MICROSTRUCTURE EVALUATION AND MECHANICAL BEHAVIOR OF HIGH-NIOBIUM CONTAINING TITANIUM ALUMINIDES

By

GLENN ESTEP BEAN JR.

A DISSERTATION PRESENTED TO THE GRADUATE SCHOOL
OF THE UNIVERSITY OF FLORIDA IN PARTIAL FULFILLMENT
OF THE REQUIREMENTS FOR THE DEGREE OF
DOCTOR OF PHILOSOPHY

UNIVERSITY OF FLORIDA

2014

To my mother, my father, Samantha, and Fereshteh

ACKNOWLEDGMENTS

To my first advisor, the late Dr. Fereshteh Ebrahimi, I owe a great deal of my success and who I am today as a researcher, as a scientist, and as a person. She always had a way of bringing out the best in a person by expecting mastery of whichever topic was at hand, and leading by example. Never before have I met someone so intelligent and persistent, while also being so caring and living life so energetically. Fereshteh pushed me to my limits and expected me to succeed, and she is the sole reason that I was able to make the quick and difficult transition into graduate school and scientific research. She made me prove to myself that if something can be achieved, I can accomplish it. For this, and for her belief in me, I cannot fully express how grateful I will always be.

To my advisor, Dr. Michele Manuel, I must express my thanks for easing my transition into her research group, and allowing me to continue to pursue my research and explore other opportunities as part of the materials design group. Because of her, I was able to not only finish my dissertation research, but also learn what it is like to create and pursue different research projects and directions. I would also like to thank my fellow researchers in the MDPL. Their advice, assistance, and distractions helped me make it through this process, and keep an even keel. Particular thanks to Dr. Michael Kesler, who I've had the pleasure of working with from the beginning, and to my advisory committee for their invaluable guidance and discussions.

To my parents, I would like to express my gratitude for all of their support, and even more so for all the decisions they made over the years, both big and small, that allowed me to make it here. They never questioned whether I would succeed; they knew I would, so they never accepted anything but my best. Whether it was helping me

understand homework in grade school, moving so we could attend better schools, or just not letting me realize how big of a nerd I really was during my childhood, I can never say thank you enough.

To Samantha, I need to offer a very special acknowledgement. She believed in me and supported me throughout the stress, the long hours, the coffee, the rewrites, and my scientific ramblings - even though she usually prefers to do science with living things. Now I can finally make up for lost time, and I am looking forward to a lifetime of doing just that.

TABLE OF CONTENTS

page

LIST OF TABLES

LIST OF FIGURES

Abstract of Dissertation Presented to the Graduate School
of the University of Florida in Partial Fulfillment of the
Requirements for the Degree of Doctor of Philosophy

MICROSTRUCTURE EVALUATION AND MECHANICAL BEHAVIOR OF HIGH-NIOBIUM CONTAINING TITANIUM ALUMINIDES

By

Glenn Estep Bean Jr

May 2014

Chair: Michele V. Myers
Major: Materials Science and Engineering

Ti-Al-Nb-based alloys with γ(TiAl)+σ(Nb_2Al) microstructure have shown promise for potential high temperature applications due to their high specific strength. Recent research has been aimed towards increasing strength and operating temperatures through microstructural refinement and control. Alloys with 10 - 30% σ-phase have been investigated, exploring relationships between chemistry, microstructure development, and flow behavior. Alloys with composition Ti-45Al-xNb-5Cr-1Mo (where x = 15, 20, 25 at%) have been produced, characterized, and tested at high temperature under compression. Processing, microstructure and mechanical property relationships are thoroughly investigated to reveal a significant connection between phase stability, morphology and their resultant effects on mechanical properties. Phase transformation temperatures and stability ranges were predicted using the ThermoCalc software program and a titanium aluminide database, investigated through thermal analysis, and alloys were heat treated to develop an ultrafine γ+σ microstructure. It has been demonstrated that microstructural development in these alloys is sensitive to composition and processing parameters, and heating and cooling rates are vital to the modification of γ+σ microstructure in these alloys. Towards the goal of designing a

high-Nb titanium aluminide with ultrafine, disconnected γ+σ morphology, it has been established that microstructural control can be accomplished in alloys containing 15-25at% Nb through targeted chemistry and processing controls. The strength and flow softening characteristics show strain rate sensitivity that is also affected by temperature. From the standpoint of microstructure development and mechanical behavior at elevated temperature, the most favorable results are obtained with the 20 at% Nb alloy, which produces a combination of high strength and fine disconnected γ+σ microstructure. Microstructural analysis reveals the γ-phase is primarily responsible for the alloy's accommodation of deformation to large strains under high temperature compression in γ+σ alloys with γ-TiAl as the primary phase, and the scale and morphology of the γ-phase correlates strongly with deformation and failure mechanisms in these alloys.

CHAPTER 1
INTRODUCTION

Advancements in the research and development of lightweight intermetallics have led to increases in the overall efficiency and performance of jet turbine and power production engines [1-5]. Improvements in γ-TiAl +α_2-Ti_3Al titanium aluminides have increased high temperature strength while demonstrating excellent properties below 750°C, owing primarily to alloying and microstructural control [2, 4, 6-9]. Alloying with elements such as Cr, Mo, Nb, and Ru have been shown to improve the mechanical properties by modifying phase transformations and their resultant microstructures [7-10]. In particular, additions of Nb in concentrations up to 10 at.% have resulted in microstructural refinement of γ+α_2 alloys, as well as improvement in strength, ductility [6] and oxidation resistance [11]. Further increasing the Nb content leads to the development of the σ-Nb_2Al phase, which can be utilized to improve high temperature properties of titanium aluminides [1, 12-14].

It has been shown that two-phase microstructures with coarse contiguous σ-phase and disconnected γ-phase exhibit high temperature strength superior to that of γ+α_2 alloys [1, 12], but have limited room temperature ductility and fracture toughness due to their high (> 0.5) volume fraction of connected σ-phase [14]. Toughness was enhanced by incorporating ductile β-phase particles into the matrix [14] or by producing a γ+σ microstructure with disconnected σ phase via heat treatment [13]. Deformation of γ+σ alloys with 60% σ-phase is dominated by interfacial sliding of the connected σ-phase [1], so it is expected that reducing the amount of Nb (and therefore σ-phase) to produce the disconnected γ+σ microstructure should change the deformation

mechanisms operant at high temperature, and deformation should be more dominated by the connected γ-phase.

Recent work has shown that by refining microstructural scale and reducing σ-phase volume fraction Ti-Al-Nb alloys with γ+σ microstructure can produce desirable properties at room temperature [10, 15, 16]. The development of an ultrafine γ+σ microstructure with γ-phase matrix and disconnected σ-phase precipitates improves strength and ductility at room temperature through grain refinement and precipitation strengthening [16]. Additionally, these precipitates may help to pin grain boundaries at elevated temperatures, reducing the extent of grain boundary sliding, which has been found to dominate high temperature mechanical behavior [12, 17, 18]. High temperature strength is typically diminished due to the increased influence of grain boundary sliding in finer microstructures [17, 19-21], however by controlling the volume fraction of σ-phase while maintaining a disconnected morphology, high temperature strength may be increased without significantly diminishing the improvements gained at room temperature. Understanding the effects of alloying on microstructure and high temperature deformation of these materials is of critical importance in order to enable the production of alloys with tunable microstructures, which can lead to desirable high temperature properties.

In order to produce an ultrafine microstructure, alloying additions of Cr and Mo are necessary to modify phase stability and transformation kinetics, which can in turn be utilized to control microstructural scale [10, 15, 22, 23]. Cr is a strong β-phase stabilizer and is therefore favorable for microstructural development [10], but the retention of β-phase in the final microstructure can be detrimental for high temperature properties [7,

11]. Mo is also a β-phase stabilizer and should partition between phases due to its large size, slowing down kinetics during microstructure development [8]. While preliminary testing of Ti-Al-Nb-Cr-Mo alloys with ultrafine γ+σ microstructure at room temperature has shown promising strength and fracture toughness [16], their high temperature properties are largely unknown.

CHAPTER 2
BACKGROUND

Currently, γ+α_2 titanium aluminides are used in the low temperature regions of jet turbines, such as the last stages of the low temperature turbine in the General Electric GeNx engine [5]. In this application, weight reduction translates directly into improved efficiency and cost savings. For these reasons, the development of titanium aluminide alloys is of interest, and the Ti-Al-Nb system shows promise for improved high temperature strength [1, 2, 6, 24].

A great amount of research has gone into the development of titanium aluminides over the past few decades, focused mainly on alloys with γ-TiAl + α_2-Ti_3Al microstructures, including research into chemistry-processing-properties relationships [25-27]. The effects of alloying additions such as Nb, V, Ta, and Cr on microstructure development and mechanical behavior of γ + α_2 alloys was investigated [28-32], as well as the introduction of Nb- or Ta-rich σ-phase and its contribution to high temperature mechanical behavior [11, 12, 33, 34]. Crystal structures of β, γ, α/α_2, and σ phases have been investigated as well as the properties of their interfaces, especially the γ/α_2 interface [25, 29, 35-37]. Throughout the development of these alloys, modification of composition, processing, and microstructure have led to improvements in alloy performance [2-4, 7, 16, 26, 27, 33].

2.1 Phases of Interest in Titanium Aluminides

Important phases in the Ti-Al-Nb system that are commonly seen in alloy development include α_2, β, γ, and σ phases [1, 2, 4, 10, 11, 38]. The β-Ti phase is a BCC solid solution that is stable in the binary TiAl system at elevated temperatures for Al content below approximately 45 at.% and is important for forming operations at

elevated temperature and machining if retained to room temperature. It is also important in the development of some two-phase microstructures in titanium aluminides [16, 23, 39], which will be discussed further in the following sections. However, it has been observed that the retention of the β-phase in the final microstructure is detrimental to toughness at ambient temperatures and elevated temperature deformation resistance [4, 7, 11]. In order to improve the high temperature performance of TiAl-based alloys, research has been done to optimize alloying chemistry and microstructure, with two-phase microstructures being commonly employed in order to improve both ductility and strength. Titanium aluminides should exhibit a balance of room temperature ductility and fracture toughness, as well as high temperature deformation resistance [4, 7], which has been the objective of recent research in this system [1, 10, 14-16, 22, 38-40].

The γ-TiAl phase is an intermetallic phase with face-centered tetragonal (FCT) $L1_0$ structure [2, 41] in which the Ti and Al atoms occupy alternating layers. Stoichiometric γ-TiAl has a c/a ratio of 1.015 (with a=4.00Å and c=4.06 Å) which varies from 1.01-1.03 with Al content from ~35-57at% [27]. Single phase γ-TiAl at room temperature has poor ductility and fracture toughness [2]. Because of its poor mechanical properties, γ-TiAl is usually present in conjunction with the α_2-Ti_3Al/$TiAl_3$ phase, an ordered intermetallic with a hexagonal $D0_{19}$ structure [2, 7, 41]. These two-phase microstructures, in which α_2 improves ductility [2] will be discussed in the following section.

The σ-Nb_2Al phase is very complex, with a unit cell containing 30 atoms [42, 43]. This phase is hard and brittle, exhibiting no ductility at temperatures up to 700°C even when toughened by a more ductile second phase [1, 12-14]. However, the effects of a

disconnected σ-phase precipitate on strength and ductility are unknown, and will be the focus of this study. In addition to in the Ti-Al-Nb system, the presence of σ-phases has been documented in Fe-Cr, -Mo; Zr-Al; Mg-Cu, -Zn, -Ni; and other transition metal alloy systems [35, 43-48], where the complex tetragonal crystal structure and its effect on microstructure have been studied. Applications of the σ-phase range from strengthening precipitates [1, 16, 36, 43] to thin films for diffusion barriers [49]. All of these phases are portrayed schematically in Figure 2-1.

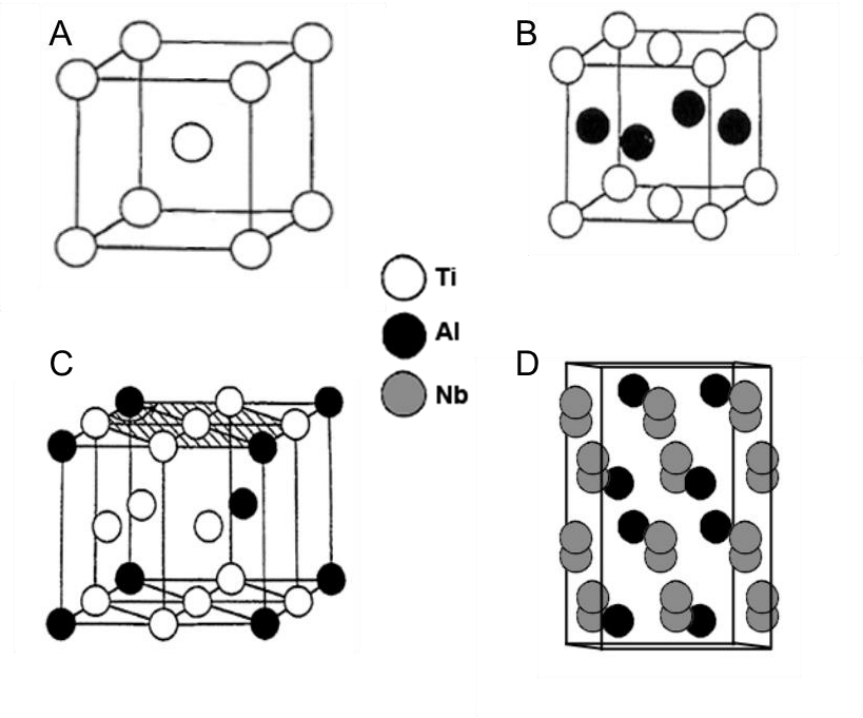

Figure 2-1: Phases of interest in the Ti-Al-Nb system. A) β-BCC, B) γ-TiAl, C) α_2-$Ti_3Al/TiAl_3$, and D) σ-Nb_2Al phases. Adapted from [2, 4, 43].

It is worth noting at this point that all compositions discussed in this document will be expressed in atomic percent (at%).

2.2 Current Microstructures of Interest

2.2.1 Gamma Plus Alpha2 (γ + α_2) Alloys

In order to improve the high temperature performance of γ + α_2 titanium aluminides, research has been done to optimize the alloying chemistry and microstructure, with two-phase microstructures being commonly employed in order to improve their ductility and strength [2-4, 6-9]. The microstructures of interest in γ+α_2 alloys include near-gamma (NG), fully lamellar (FL), nearly lamellar (NL), duplex (DP), pseudo-duplex (PS-DP), and equiaxed [2-4, 6, 8]. Examples of some of these microstructures can be seen in Figure 2-2.

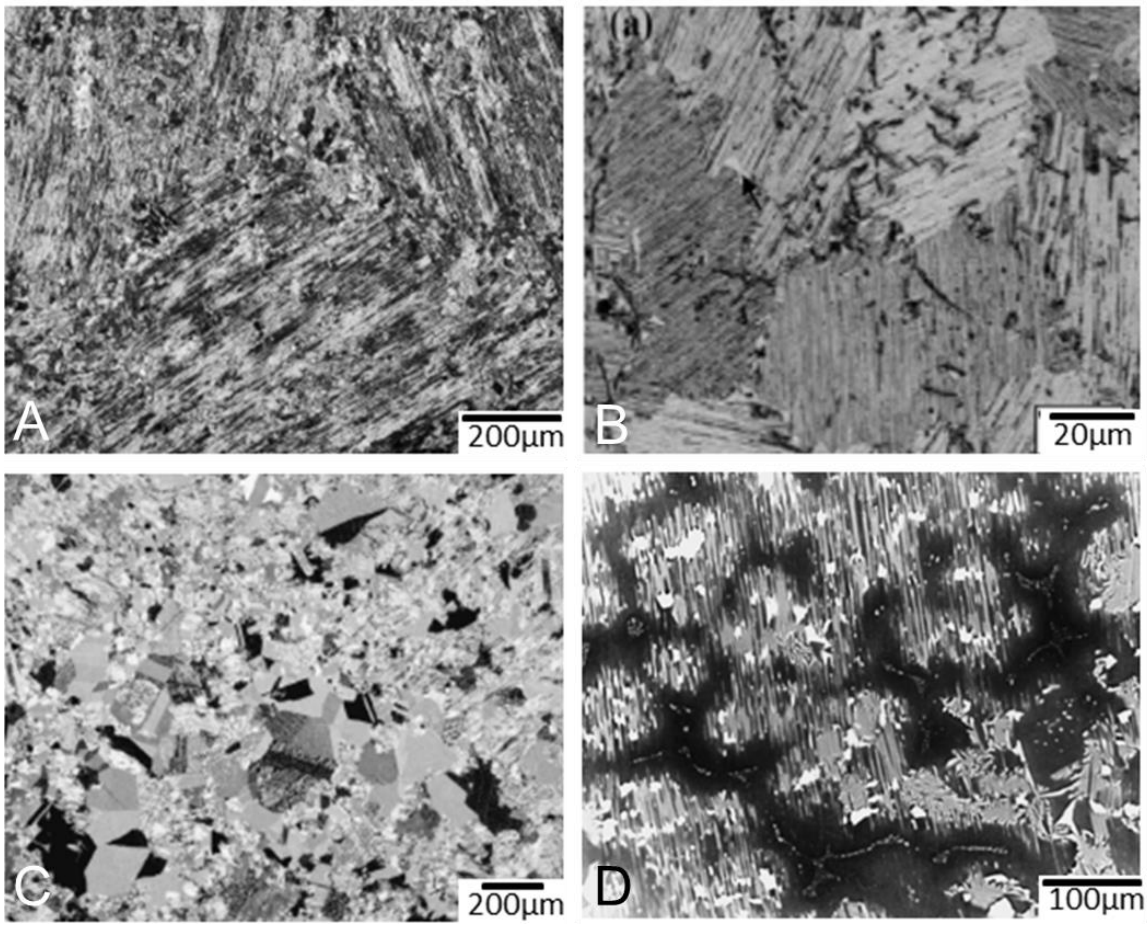

Figure 2-2: SEM micrographs illustrating γ + α_2 microstructures. A) nearly lamellar, B) fully lamellar, C) duplex, and D) pseudo-duplex. Adapted from [41, 50].

By modifying the morphology of these alloys, its mechanical properties at room temperature and elevated temperatures can be improved. The FL γ+α_2 microstructure consists of colonies of γ and α_2 platelets, and is generally characterized by high fracture toughness, and high resistance to crack propagation when compared with DP microstructures [2, 42]. The DP microstructure is a combination of single-phase γ-grains and lamellar γ+α_2 colonies, and is characterized by a higher tensile strength, higher ductility, and longer fatigue life. This microstructure is developed upon cooling from the γ+α phase field at moderate cooling rates with the transformation of prior α grains to lamellar γ+ α_2 [51]. An equiaxed microstructure can also be formed, with equiaxed γ-grains and large α_2 particles at the grain boundaries, and exhibits higher strength and ductility than DP microstructure, however the FL microstructure has been shown to significantly outperform the equiaxed microstructure [8, 11, 51].

Effect of Alloying Additions

In the development of TiAl-based alloys, there are many competing parameters must be taken into account when choosing alloying additions. Some of these issues include changes in phase stability, precipitates, microstructure morphology, transformation kinetics, and mechanical properties.

Niobium additions strengthen TiAl-based alloys, improve high temperature deformation properties, and improve oxidation resistance [1, 11, 24]. The addition of Nb increases α_2 content and refines the microstructure, increasing strength due to the Hall-Petch mechanism [11, 19]. Nb is also a slow diffuser in γ, reducing diffusion-assisted dislocation climb and reducing steady state creep rate and increasing high temperature strength [11, 52]. Alloys with additions of 4-12 at% Nb and Ta produce γ + α_2

microstructure, and show that for all amounts of Ta and Nb additions, the alloys with lower Al content (45 vs. 47 at%) exhibit higher strength, but lower plasticity, with a quaternary alloys of Ti-45Al-4Nb-4Ta showing the best combination of strength and plasticity [53].

The addition of β-stabilizing elements such as Cr, Mo, Si, Ta, and W [37, 54-57] can be essential in retaining this phase upon quenching, which is an integral part of microstructural control, as will be discussed in the following section [10, 23, 39]. In this work, Cr will be used, as it is a strong β-stabilizer, however Cr can also have a detrimental effect on high temperature properties above 700°C due to the retention of β-phase, which has a very open structure at high temperature [7, 11, 58]. Conversely, at temperatures of 700°C and below the presence of β-phase improves these properties [2, 7]. Cr is also known to increase ductility in γ-based alloys [2, 3, 7].

Molybdenum is alloyed into titanium aluminides due to its low diffusivity, which limits the kinetics of phase transformations by partitioning between phases [16]. The addition of 0.66 at.% Mo to a Ti-24Al-17Nb γ + α_2 alloy improves high temperature deformation resistance, and increasing the Mo content to 2.3 at.% results in an additional order of magnitude enhancement in steady state creep rate, but embrittles the alloy [8]. This improvement in high temperature deformation is also attributable to the reduction in α_2/α_2 interfacial sliding due to the lower volume fraction of the phase. It was found that the alloying with 1 at% Mo yields comparable improvements at elevated temperatures without the accompanying embrittlement suffered with 2.3 at% Mo [8]. For the purposes of alloy development in γ+σ alloys, the slow diffusivity and β-stabilizing

properties of Mo are of the most interest [8, 16, 39], enhancing the alloys' capability to form the targeted microstructures.

2.2.2 Gamma Plus Sigma (γ+σ) Alloys

2.2.2.1 Introduction of the σ-phase

By increasing the Nb content in Ti-Al-Nb based alloys, high temperature strength is improved through both solid solution strengthening effects of Nb as well as precipitation strengthening through the introduction of a hard σ-phase in lieu of the α_2 phase [4, 6, 24]. Due to the potential for significant improvements in high temperature performance, alloys with γ+σ microstructure are currently of interest for continued study.

In the Ti-Al-Ta system it was also found that a $(Ti,Ta)_2Al$ σ-phase can be produced in Ta-rich alloys, and research by Weaver and Kaufman shows that the formation of σ-phase in alloys with ≥ 25 at% Ta is strongly dependent on cooling rate and composition [59]. Kim et al. showed that Ti-Al-Ta alloys containing 32-40 at% Al and approximately 25 at% Ta produced a fine two-phase γ + σ microstructure when splat quenched alloys were re-annealed below 1200°C [60]. Additionally, it was found that alloys with composition Ti-50Al-25Nb solidify as β, which exists as a single phase above 1520°C, undergoes several phase transformations including the β, γ, α, and σ-phases, but consists of only γ + σ below 1300°C [61]. Investigation into the nature of phase transformations and relationships in Ti-Al based systems [15, 38, 59, 61-66] is instrumental in the design of alloy composition and microstructure.

Alloys in the Ti-Al-Nb system with 60% σ-phase prove to significantly improve high temperature strength when compared with γ+α_2 alloys, however room temperature ductility and fracture toughness are somewhat limited [12-14, 40]. When tested at

700°C the alloy (27Nb-33Ti-40Al) suffered brittle failure and at 900°C there was approximately 10% total strain before failure [1]. At 1000°C, a yield strength of approximately 450 MPa was achieved at $3.5^{x}10^{-4}$ s^{-1}, which is a large improvement over γ+α_2 alloys, which generally have yield strength of ranging from 275 - 400 MPa at similar strain rates at 700°C [1, 2, 4]. Analysis of samples strained to 55% showed significant fragmentation of the σ-phase, which was more prominent at lower strain rates [1]. Ductility and fracture toughness of the σ-based alloys is limited, due to the fact that at 60%, the σ-phase is the connected phase, acting as the load-bearing matrix phase and determining the mechanical properties of the alloy, and it has been shown that by including ductile second-phase particles of β-phase, fracture toughness can be enhanced [1, 13, 14].

It has also been proven that the scale and morphology of the microstructure has a significant effect on the strength and ductility of the alloy, and can be changed by modifying the heat treatment schedule [1, 12]. An alloy with composition Ti-40Al-27Nb was solution treated at 1450°C for 2 hours then oil quenched. If subsequent single-aging (SA) was carried out at 1200°C for 5 hours, this resulted in a fine, connected σ-morphology. However if a two-step double aging (DA) treatment was carried out, first at 1300°C for 12 hours and then 1200°C for 14 hours, the result is a much coarser disconnected DP σ-phase morphology. Comparison of these microstructures can be seen in Figure 2-3. Aging at 1300°C produces σ+γ+β microstructure, then during aging at 1200°C, the β-phase between coarse σ-particles transforms to fine γ+σ [1]. This coarse disconnected microstructure is due to the improved diffusion at a higher aging temperature and additional time allowed for the coarsening and coalescence of the σ-

phase, but despite the large difference in morphology, there is nearly equivalent V_f σ-phase in both microstructures [1, 12].

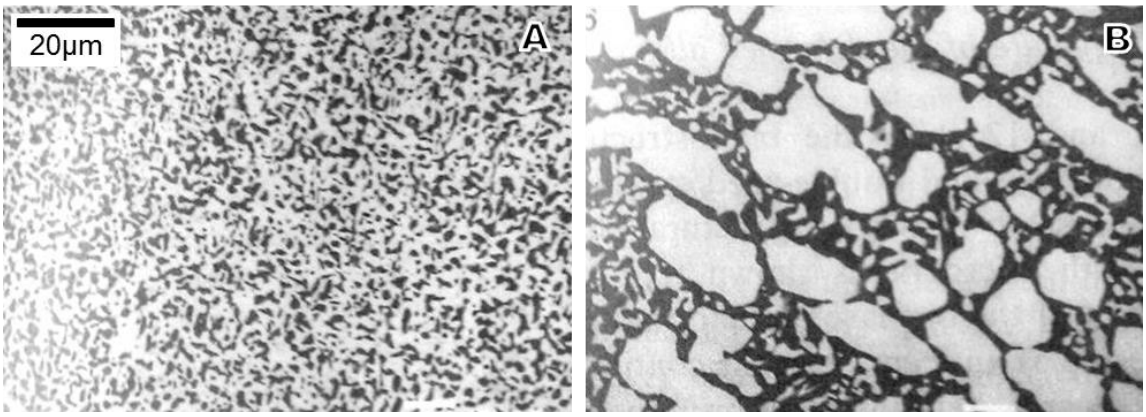

Figure 2-3: SEM micrographs illustrating difference in microstructure scale and morphology between γ+σ microstructures. A) single-aged; B) double-aged [1] (Courtesy of B.J.G. deAragao)

The single-aged alloy can be approximated as a ductile phase toughened composite, and it has been shown that the high temperature deformation behavior is insensitive to the properties of the weak, disconnected phase when there is a strong connected matrix [1]. From analysis of the microstructure and flow properties, it was found that the primary active mechanism is grain boundary sliding in the σ-phase in the single-aged microstructure [1, 12]. This grain boundary sliding was seen to a greater extent in the finer SA microstructure due to the greater amount of σ/σ interfaces. In contrast, the active mechanisms in the double-aged alloy with a disconnected DP microstructure were dislocation motion and twinning in the γ-phase, as well as grain boundary sliding [1, 12]. Additionally, from compression testing at 1000°C, it was concluded that for both microstructures of this alloy, dynamic recrystallization of the γ-phase occurred which is indicative of the characteristic serrated displayed in the flow

curves [1, 12, 67, 68]. Tensile behavior of the SA alloy is presented in Figure 2-4, which shows the transition from brittle to ductile behavior.

2.2.2.2 Past research into the Ti-Al-Nb system

In addition to the previously discussed research, there were many investigations into the thermal, microstructural, and mechanical characteristics of alloys in the Ti-Al-Nb system under the direction of Dr. Fereshteh Ebrahimi [1, 10, 12-16, 23, 33, 38-40, 52, 65, 66, 69, 70].

Early research into the development of high temperature Nb-based alloys was conducted by master's student Jesus R. Castillo-Gomez [33]. His study was into alloys with compositions of 27Nb-33Ti-40Al (alloy #2) and 42Nb-28Ti-30Al (alloy #4) (all compositions in at%), which were arc melted, solution treated in the single-phase β-region, water quenched, and aged to produce γ + σ (+ β) and σ + β (+o) microstructures in alloys #2 and #4, respectively. In compression testing, alloy #2 yielded preceding fracture at 700°C, showing higher fracture strengths of 1200 – 1900 MPa, compared with alloy #4, which fractured without plastic deformation with strengths ranging from 1100 – 1500 MPa at 900°C. Fracture strength was found to be insensitive to microstructure in both alloys, though yield strength of alloy #2 decreased with increasing γ-phase content [13, 14, 33, 40]. Research conducted by undergraduate researcher B. Thad Solomon, found that in alloys with σ + β microstructure, Vickers hardness is directly related to volume fraction of σ-phase, while fracture toughness is inversely related to σ-phase volume fraction [36].

Toughness was also evaluated through testing of 4-point bending specimen with chevron notch, and values calculated using the curve fitting model and indentation data were found to be within 20% of the measured values [14, 71]. There was increased

K1C values specimen from SA to DA samples, from 4.4 to 6.3 $MPa\sqrt{m}$ due to the discontinuous nature of the σ-phase in the DA alloys which does not continuously propagate a crack. Fractography shows that cracks propagate intergranularly at σ/γ boundaries and transgranularly when areas of high σ-phase concentration were encountered, indicating both the potential of high internal stresses at the σ/γ boundary as well as the brittle nature of the large σ-phase precipitates [1, 33].

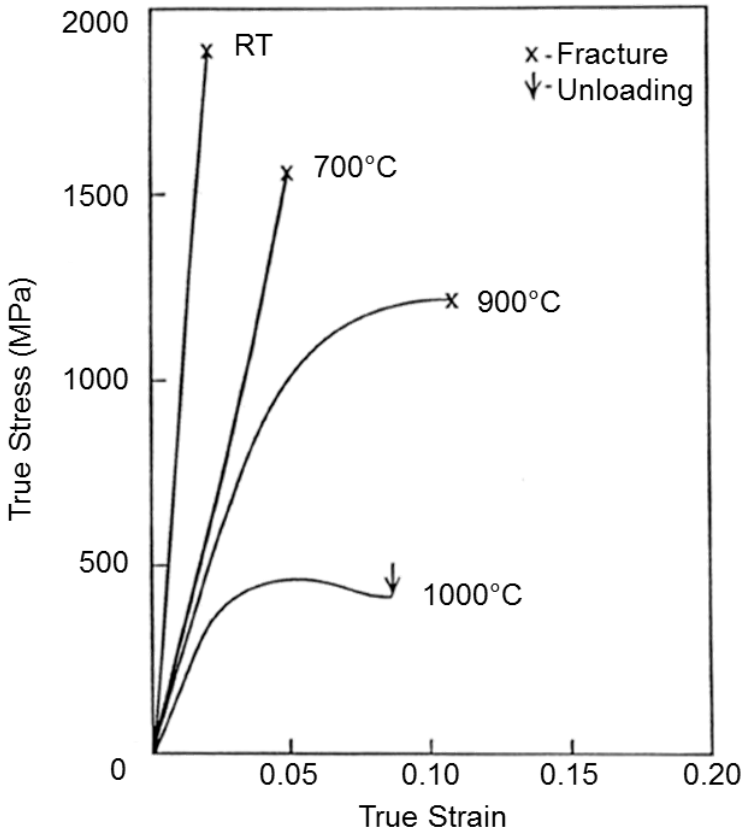

Figure 2-4: High temperature compression testing of 27Nb-33Ti-40Al (alloy #2) in the single-aged condition. Adapted from [12].

Following this, research was conducted by master's student Bernardo J. G. deAragao into the high temperature deformation of 27Nb-33Ti-40Al alloys, as detailed in section 2.2.2. The major findings of this research show that compression testing at

1000°C results in flow softening and dynamic recrystallization of the γ-phase. The σ-phase also underwent fragmentation during deformation, and the main mechanism responsible for this behavior was grain boundary sliding. Creep testing was also carried out in uniaxial compressive stress for both single-aged and double-aged microstructures, yielding very similar steady-state creep rates, as seen in Figure 2-5 [1, 12, 13].

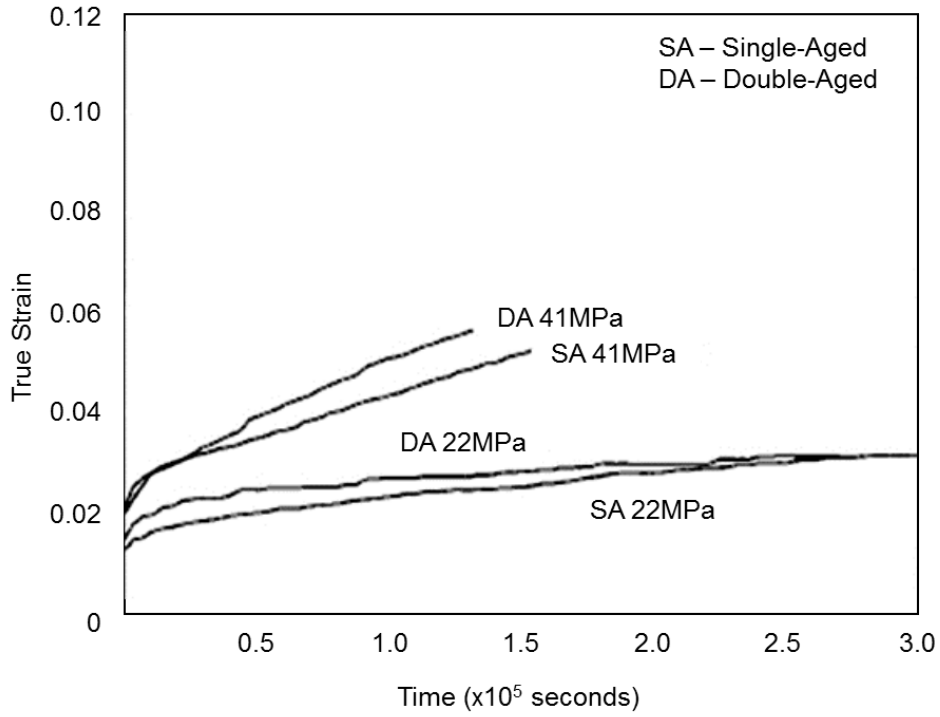

Figure 2-5: Creep testing of 27Nb-33Ti-40Al samples in SA and DA condition at 1000°C. Adapted from [1]

2.2.3 Recent γ+σ alloy development

Since the high V_f of connected, brittle σ-phase led to fragmentation and limited ductility, alloys with lower volume fractions have been explored [10, 15, 16, 23, 39, 70]. By reducing grain size, strength and ductility can both be improved [19, 72] and by maintaining a disconnected σ-phase, the brittle nature of the alloy can be mitigated.

Design of a duplex microstructure of ultrafine σ-phase precipitates as well as disconnected nanoscale σ-phase along the γ-phase grain boundaries may be effective in achieving these improvements [13, 73]. Already, several alloys have been explored with approximately 0.15 V_f σ-phase which have shown an increase in both strength and fracture toughness, and has shown that by microstructural refinement, Ti-Al-Nb alloys with γ + σ microstructure can produce desirable properties at room temperature [10, 15, 16].

The purpose of these alloys was to produce an ultrafine γ+σ microstructure through suitable composition and heat treatment control. In order to create the desired ultrafine microstructure, its evolution must be carefully controlled. For this reason, a two-step heat treatment was developed, which will be discussed in further detail in following chapters. Unlike the previously developed alloys, these alloys do not cool to room temperature as single-phase β upon casting. Therefore, the alloy is first solution treated in the single-phase β solid solution region, then quenched to room temperature to retain the β-phase. This step is to ensure homogeneity of the alloy and to enable the controlled precipitation of the γ+σ microstructure by subsequently aging in the two-phase region. Since the γ- and σ-phases are precipitated simultaneously, the σ-phase can effectively limit the growth of the γ-phase, producing an ultrafine microstructure.

Two preliminary alloys have been investigated, with compositions Ti-45Al-18Nb and Ti-45Al-27Nb. In these alloys, there has been difficulty in retaining pure β-phase upon quenching to room temperature, and a significant amount of γ-phase precipitated. In order to retain β-phase upon quenching, alloying with Cr, a known β-stabilizer was explored [4, 10]. Replacing 5 at% Nb with Cr has been shown to effectively stabilize the

β-phase in the Ti-45Al-22Nb-5Cr alloy, but was ineffective in alloy Ti-45Al-13Nb-5Cr, which still formed γ-phase laths at the β-phase grain boundaries [10, 23, 39].

In Ti-45Al-22Nb-5Cr, the β-phase is fully retained upon quenching to room temperature, but γ-phase laths still grew from the β-grain boundaries immediately upon aging. Also, there is a very small range of aluminum composition in which retaining single-phase β upon quenching is possible without γ-phase precipitation. Varying the aging temperature has been shown to change the microstructural scale as well. When Ti-45Al-22Nb-5Cr is aged at 865°C, a fine microstructure with disconnected σ-phase was produced. When aged at 1050°C, the resulting microstructure was coarser with mostly connected σ-phase, though the V_f of σ-phase was the same, approximately 30% [16].

Along with reducing the amount of Nb in the alloy when compared with past research, further alloying with Mo was conducted. The purpose of adding Mo to the alloy is to slow the kinetics of phase transformations upon quenching and at elevated temperatures, allowing for stability in the microstructure and high temperature performance. This was studied with composition Ti-45Al-14Nb-5Cr-1Mo. Although the precipitation of γ-phase upon quenching was not fully suppressed, a similar method to that used with Ti-45Al-22Nb-5Cr may be used to test the performance of the alloy without the effects of grain boundaries. That is, samples can be machined such a way as to avoid the presence of prior β-phase grain boundaries. In this way, Ti-45Al-14Nb-5Cr-1Mo produced an ultrafine microstructure, leading to compressive ductility of 15-30% and yield strength of about 1300 MPa at room temperature, and fracture toughness increased to about 15 $MPa\sqrt{m}$ [16].

While preliminary testing of alloys with ultrafine γ+σ microstructure at room temperature has shown promising strength and fracture toughness [16], their high temperature properties are unknown. As previously discussed, the deformation of γ+σ alloys with 0.6 V_f of σ-phase is dominated by interfacial sliding of the connected σ-phase [1, 12], so it is expected that reducing the amount of Nb (and therefore σ-phase) to produce the disconnected γ+σ microstructure should change the deformation mechanisms operant at high temperature. Deformation should be more heavily influenced by the connected γ-phase, but the importance of competing deformation mechanisms is unknown. It is the goal of this research to investigate the microstructure development and high temperature mechanical properties in an alloy with ultrafine γ+σ microstructure through compression testing and the evaluation of microstructural evolution occurring during heat treatment and deformation.

2.3 High Temperature Deformation Mechanisms

2.3.1 Strain Hardening

Strain hardening is the increase in dislocation density as strain is induced in a material. Strain hardening decreases with temperature, but increases with strain rate, as described by the Orowan equation,

$$\dot{\varepsilon} = \frac{1}{2}\dot{\gamma} = b\rho\bar{v} \qquad (2\text{-}1)$$

for a polycrystalline metal, where $\dot{\gamma}$ is the shear strain rate [20, 21]. As tensile strain rate ($\dot{\boldsymbol{\varepsilon}}$) increases, dislocation density (ρ) or average dislocation velocity ($\bar{v}$) must also increase in order to accommodate deformation, assuming a constant burger's vector (b). Since dislocation velocity is controlled by vacancy diffusion, at constant temperature the density of mobile dislocations must increase with increasing strain rate

[20, 74, 75]. At higher temperature, vacancy diffusion is easier so dislocation velocity can be higher resulting in a lower work hardening rate, as fewer dislocations are necessary to maintain the given strain rate [2, 11, 19, 20, 74, 75].

2.3.2 Dynamic Recovery and Recrystallization

Dynamic recovery and recrystallization are important softening mechanisms that can occur during deformation above 0.5 homologous temperature in metals. Dynamic recovery is defined by the movement of dislocations, during plastic deformation, to lower-energy arrangements, often to grain boundaries, or to form sub-grain structures [21]. Similar recovery can occur under static conditions during annealing after plastic deformation, but during deformation at high temperature the effects of dynamic recovery increase due to increased dislocation mobility, and reduces the effective strain hardening rate in the material [21]. It has been found that dynamic recovery occurs more strongly in materials with high stacking-fault energy, suggesting that thermally activated cross slip is the controlling mechanism [21].

In materials where dynamic recovery does not occur quickly, dynamic recrystallization can occur. Softening due to dynamic recrystallization results in a sharper drop in stress, and dependent on the amount of strain required to fully recrystallize the metal, the flow curve can take on one of two characteristic shapes. These characteristics include a peak stress value followed by flow softening and oscillations in the flow stress [76], or a peak stress followed by continuous flow softening to a steady-state value [21].

During dynamic recrystallization, dislocation-free grains are formed and as the material is strained further, the dislocation density increases in these grains up to a critical value, at which point recrystallization is initiated once again [76]. If one wave of

recrystallization is completed before the critical strain to nucleate recrystallization is reached again, this leads to periodic oscillations in the flow stress. If instead the critical strain to complete recrystallization is greater than that to nucleate recrystallization, then a second wave of recrystallization will begin before the first is completed, leading to a flow curve with a peak stress and softening to a steady-state value.

Another factor that can affect the dynamic recrystallization behavior of this material is alloying additions [67, 76]. If alloying additions are in solid solution the solute drag effect may hinder the growth of recrystallized grains in addition to potential for grain boundary pinning from the σ-Nb_2Al particles [1, 19, 21, 74]. Additionally, particle stimulated nucleation (PSN) of dynamic recrystallization is a phenomenon observed in precipitation- and dispersion-strengthened alloys with particles approximately 1 μm or larger [74].

2.3.3 Interfacial Sliding

Strain accommodation can also occur by interfacial, or grain boundary sliding, especially at elevated temperature, and for very fine grained metals [76, 77]. Grain boundary sliding is the shear-induced deformation between two adjacent grains, resulting in deformation that is highly local to the interface between the grains. However, it is not able to operate as a singular deformation; interfacial sliding must be accompanied by either grain boundary diffusion or volume diffusion through the grains [77]. If diffusional flow operated independently, it would lead to grain elongation and separation under applied strain, but grain boundary sliding is able to accommodate the deformation and keep the grains together [77].

2.3.4 Dislocation Climb

At room temperature, deformation is typically controlled by dislocation glide, but at elevated temperature, edge dislocations can move out of their slip planes through dislocation climb [19, 21, 78]. This thermally-activated mechanism is controlled by diffusion, and allows edge dislocations to move perpendicular to its slip plane in order to reach a parallel plane directly above or below. Positive climb occurs when a vacancy diffuses to the dislocation and an atom moving to the vacant site, where negative climb is the movement of atoms to the extra half-plane, creating vacancies that diffuse away from the dislocation [19, 21]. Positive climb is associated with a compressive stress in the slip direction, while negative climb is associated with a tensile stress [19]. Both positive and negative climb result in the formation of jogs [19, 21, 78], which act as sources and sinks for vacancies [78].

2.4 Strengthening Mechanisms

2.4.1 Solid Solution Strengthening

One method of strengthening observed in metals is solid solution strengthening, accomplished through the introduction of solute atoms into solution. These solute atoms alter the crystal structure of the material and, when compared with a pure metal, increase strength. Solute atoms can either occupy the same lattice sites as the solvent metal, known as substitutional solid solution, or occupy the space between the solvent's atoms in the lattice, known as interstitial solid solution. Interstitial solid solutions occur when the solute atom is substantially smaller than the metal it is being alloyed with, commonly occurring elements such as carbon, boron, nitrogen, or oxygen. Substitutional solid solution occurs when solute and solvent atoms are close in size, such as additions of niobium or chromium to titanium alloys.

The ability of elements to form substitutional solid solutions is governed by the Hume-Rothery rules, which state that the controlling factors are relative size, valence, electronegativity, and crystal structure of the two atoms [19]. The work of Hume-Rothery found that in solid solutions, a size difference of more than 15% will reduce solubility to less than 1%, but when valence is taken into account, it is found that metals of lower valence have less solubility in metals of higher valence when compared to the reverse situation. Elements must also have similar electronegativity, as those that do not are more likely to form intermetallics than solid solutions. Lastly, in order for there to be complete mutual solubility, the elements must have the same crystal structure.

Solute atoms can strengthen alloys by interacting with dislocations in a few ways. Substitutional solutes cause local changes in lattice parameter, and the resulting misfit stress causes an elastic interaction with the dislocation line. This local change in crystal structure can also affect the local modulus of the material. Solute can also impede dislocation motion by their attraction to the strain fields surrounding the dislocations. Since there is a localized compression on the matrix above a dislocation line, and a tensile state below it, solute atoms are attracted to this site. Smaller atoms can reside above the dislocation line in order to reduce the amount of compressive strain experienced in the matrix. Likewise, larger solutes are attracted to the area below dislocation lines. This attraction between solutes and dislocations causes the motion of dislocations through the metal to be slowed. One typical case of such attraction is with Cottrell atmospheres, where carbon interstitial solutes are attracted to the dislocation lines, forming an ‘atmosphere’ around the dislocation. In order for dislocations to move, it must overcome this energetically favorable condition, or move slowly enough to allow

for the diffusion of the Cottrell atmosphere along with the dislocation. Solutes can similarly interact with other dislocation line phenomena such as stacking faults and anti-phase boundaries, impeding their motion through the alloy during deformation.

2.3.2 Grain Boundary Strengthening

Another method of strengthening commonly employed in alloy development is grain boundary strengthening. Grain boundaries act as obstacles to the movement of dislocations, so by decreasing grain size strength increases due to the increase in the number of these obstacles. The amount of strengthening can be predicted using the Hall-Petch relationship which describes that yield strength is inversely proportional to grain size. In this equation, $\boldsymbol{\sigma_y}$ is the yield strength of the material, $\boldsymbol{\sigma_0}$ is the "friction stress" representing the overall resistance of the crystal lattice to dislocation movement, $\boldsymbol{k}$ is a material constant, and $\boldsymbol{d}$ is the average diameter of the grains [19].

$$\boldsymbol{\sigma_y = \sigma_0 + k d^{-\frac{1}{2}}} \tag{2-2}$$

This relationship is based on the dislocation pile-up theory, whereby dislocations pile up and must induce a critical stress in the neighboring grain in order to produce additional dislocations in that neighboring grain that will then propagate.

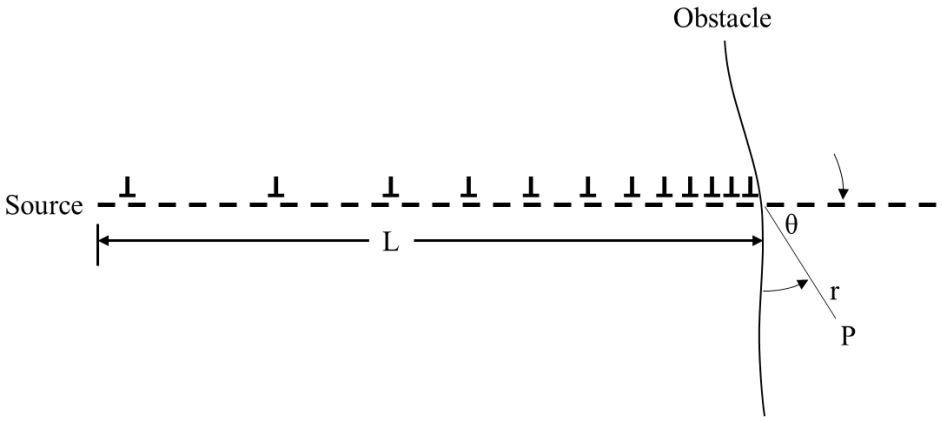

Figure 2-6: Dislocation pile-up at a grain boundary. Adapted from [19].

As the size decreases, the pile-up stress induced by the dislocations decreases, so an increased amount applied stress is required to cause slip in the neighboring grain. Dislocation pileup is illustrated schematically in Figure 2-6 below, where ***L*** is the dislocation pile-up length, and the location in the neighboring grain (point ***P***) is described by ***r***, ***θ***.

2.3.3 Precipitation Strengthening

To increase the strength of metal alloys, it is common to introduce second phase precipitates into the microstructure. These particles increase the strength of the material by impeding the motion of dislocations through the matrix. When a dislocation encounters a precipitate, it must either cut or bypass the particle.

For the dislocation line to shear a precipitate, the precipitate must be deformable and have a coherent or semi-coherent interface with the matrix. Important factors that determine the ability of precipitates to be cut are its Peirls stress, elastic modulus, and stacking fault energy. These factors affect the dislocation line energy as it passes through the precipitate and determine if it is energetically feasible to cut the particle rather than bypass it. For a dislocation line to bypass a precipitate it must bow around it and form a loop, and each loop make it more difficult for the next dislocation line to bypass the particle by effectively increasing the precipitate size, and is known as the Orowan strengthening mechanism for dislocation movement through a precipitate-containing matrix, illustrated in Figure 2-7.

Other precipitate strengthening mechanisms include misfit strain, chemical hardening, and strengthening due to ordered structures. Misfit strains, due to the mismatch in size of the particle and matrix, can either attract or repel dislocations, increasing the force required for them to approach or escape the precipitate as it bows.

Strengthening due to ordered particles is also important in high temperature metals. As the dislocation line passes through an ordered precipitate, anti-phase boundaries (APBs) will be formed as it is sheared, which can increase the energy of the dislocation line and make shearing more difficult [19]. Also, by shearing a particle, a step is created, which increases the surface energy of the particle. This may lead to shear localization, since the cross sectional area of the particle along that plane is smaller, so it is requires less force to propagate subsequent dislocation lines.

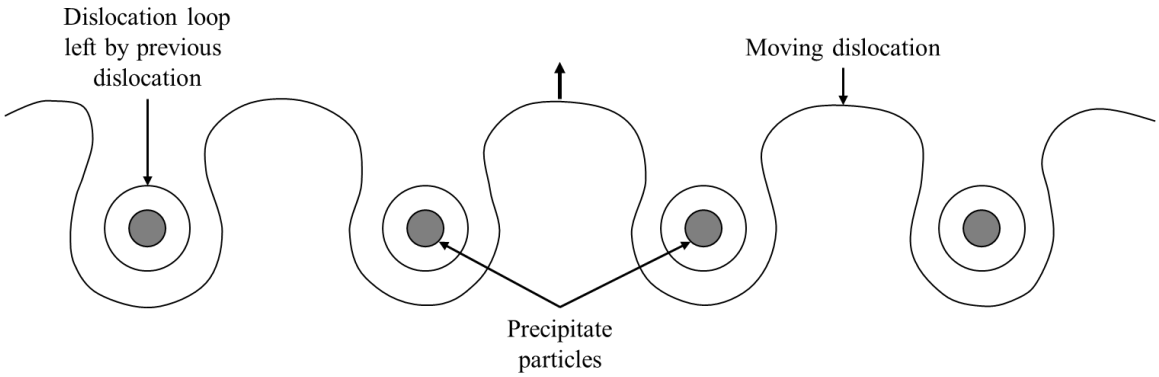

Figure 2-7: Orowan Looping. Adapted from [21]

Small particles are more effective at strengthening by dislocations cutting them, but as they become larger and more difficult to cut, dislocations must bypass them, and larger particles are effective for Orowan strengthening. This tradeoff is illustrated in Figure 2-8. While cutting of precipitates depends highly on precipitate properties, bowing of dislocations requires a non-deformable particles and is dependent on precipitate spacing, as described in Equation 1-2, where $\boldsymbol{\tau_0}$ is the amount of stress required to bow the dislocation line between the precipitates, ***G*** is the shear modulus, ***b*** the burgers vector of the dislocation, and $\boldsymbol{\lambda}$ the inter-particle spacing.

$$\boldsymbol{\tau_0} = \frac{\boldsymbol{Gb}}{\boldsymbol{\lambda}} \tag{1-2}$$

Controlling the size of precipitates through heat treatment, therefore, allows for maximization in the effectiveness of precipitation strengthening. This becomes an issue with over-aging of precipitates, especially for high temperature materials that may experience operating temperatures near those used in heat treatment. Therefore, it important to ensure stable precipitates in order to retain the desired strengthening effects throughout the material's lifetime.

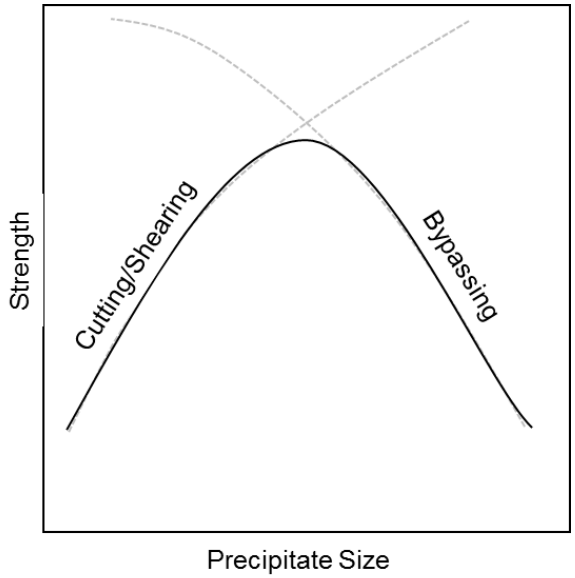

Figure 2-8: Schematic representation of precipitate strengthening mechanism vs precipitate size

One very important aspect of precipitation strengthening to note that the dislocation mechanisms discussed in this section are relevant for deformation at lower temperature. During high temperature deformation, dislocation climb is active, which changes the dislocation-particle interactions, may limit the amount of dislocation cutting and bowing that occurs, dependent on particle size and spacing, and particles may act as a source and sink of dislocations [19, 21, 76]. Larger particles are more difficult to overcome via climb, and have a greater effect on deformation and recrystallization behavior in high temperature alloys [21, 76].

CHAPTER 3
EXPERIMENTAL METHODS

3.1 Raw Materials and Alloy Fabrication

Metals for materials for alloy fabrication were obtained from a combination of sources. Elemental forms of Ti, Al, Nb, Cr, and Mo were purchased through Alfa Aesar in the following forms. Ti granules, 99.99% purity (metals basis excluding Na and K). Al wire, 2.0mm (0.08in) diameter, annealed, Puratronic® 99.999% purity. Nb wire, 1.0mm (0.04in) diameter, 99.8% purity (metals basis). Chromium lumps, 99% purity. Molybdenum wire, 1.0mm (0.04in) diameter, 99.95% purity. Raw material preparation and cleaning will be detailed in the following section.

3.1.1 Arc Melting

Raw materials were arc melted to fabricate 5-25g buttons and bars using a MRF ABJ 900 large bell jar arc melter with water-cooled copper hearth and Miller GoldStar 652 power supply with 800 ampere capacity. Non-consumable tungsten electrode arc melting was conducted under approximately 5 psi positive pressure argon (Ar) environment in order to minimize the potential for oxidation. Pressure was set via pressure relief valve, with flow rate of Ar between 5-30 mL/min, as regulated by secondary operator of arc melter. In order to ensure sufficient gas flow, pressure was set to 25-30 psi at the argon tank regulator.

Arc melting was selected as the alloy fabrication method of choice primarily due to the very high melting points of the metals being alloyed, as well as their susceptibility to oxidation. Melting points of pure Ti, Nb, Cr, and Mo are all well in excess of 1200°C, which is the limit of the available box furnaces. Additionally, these elements have a

high reactivity with oxygen at elevated temperature, and the formation of oxides during the alloy fabrication process would severely alter its material properties.

Raw materials were prepared by first washing in a soap-water solution and rinsing, then washing an ultrasonic bath in 3% Nital, and rinsed with 2-Propanol. This was done to remove any dirt, oils, or oxide that the materials may have encountered or developed during handling. The exception to this is Mo, for which the Nital wash is omitted since it would cause a surface oxide to evolve. Metals were then dried completely before being placed into the arc melter. Nb, which was in either shaving or powder form, was placed at the bottom of the hearth with pure Ti layered above so the arc would not blow them out of the way upon initial melting. Due to the complete mutual solubility of these two elements [79], they will combine readily upon melting. Al was placed on the side so that the arc would not directly strike it, but would be indirectly heated when the Nb and Ti are melted and then be drawn into the solution. Cr and Mo were scattered on top, as there were relatively small amounts of each of these alloying elements and there is not a risk of these heavy metals being perturbed by the arc upon melting.

Melting of the alloys was conducted at 450 amperes current and pure Ti samples were used for oxygen gettering. After starting the arc, the getter was first melted, and then each sample was melted for 15-20 seconds, with the getter being melted again between each one in order to reduce the risk of oxidation. Samples were checked after each melting to ensure complete melting, no oxidation, and they were flipped over to prepare for subsequent melting. Each sample was melted a total of six times in order to

ensure homogeneity. After melting was completed, composition was confirmed by electron probe microanalysis (EPMA).

3.1.2 Externally prepared alloys

Once alloy compositions were selected from evaluation of the small-scale samples prepared via arc melting, larger 250g buttons were fabricated externally. Alloys of composition Ti-45Al-xNb-5Cr-1Mo (where x = 15, 20, 25 at%) were fabricated by Sophisticated Alloys Incorporated with alloy composition verified independently via inductively coupled plasma (ICP) mass spectroscopy. Each alloy composition was within 0.4 at% of the nominal composition. A summary of ICP results can be found in Appendix A. These large buttons were used for thermal and mechanical analysis.

3.2 Alloy Characterization

3.2.1 Electron Probe Microanalysis (EPMA)

EPMA of the experimental alloys was conducted on a JEOL Superprobe 733 at the Major Analytical Instrumentation Center (MAIC) at the University of Florida. The system was calibrated with Ti, Al, Nb, Cr, and Mo standards, and was operated by Wayne Acree of the MAIC staff. Readings were taken using 1µm spot size at sets of ten randomly chosen spots on each alloy to obtain an average bulk reading. Since microstructure scale is sufficiently smaller than spot size, an average of these readings results in reasonable bulk composition quantities.

3.2.2 Differential Scanning Calorimetry (DSC)

Samples of arc melted buttons were sectioned, heat treated, and tested using a Setaram Setsys EVO 1750 Differential Thermal Analysis (DTA)/Differential Scanning Calorimetry (DSC)/Thermal Gravimetric Analysis (TGA) system with DSC 1600 rod. Testing was conducted under flowing helium (He) environment with temperature

ramped at 10 °C/min between 600-1550°C. Calibration of the DSC system was completed through the Setsoft2000 software for varying temperature ranges using indium (In), Al, copper (Cu), and nickel (Ni) standards.

Samples ranging from 100-200mg were prepared with a very flat bottom face in order to ensure good thermal contact with the alumina 100μL crucibles. Before each run, an empty crucible is cycled through the program and this output is used as a baseline subtraction for the data collected in the subsequent run using the same crucible loaded with a sample. Prior to heating the sample chamber, it is pumped and purged with He gas four times to clear any atmosphere or contaminants that may have entered the system upon sample loading. DSC was conducted on 15, 20, and 25 at% Nb samples in the as-cast and solution treated conditions.

Samples for DSC analysis were cut from the solution treated alloy using a low-speed diamond saw, and DSC of these alloys was conducted under the same conditions as described above, but the first heating cycle, which shows the phase transformations from the metastable quenched-in phase, was used to determine metastable phase transformation temperatures. Analysis of DSC results paired with XRD was used for determination of phase transformation temperatures and stability regions of these alloys in order to design heat treatments.

3.2.3 X-Ray Diffraction (XRD)

Phase identification was conducted on alloy samples before and after heat treatment using an XPert Powder X-Ray diffractometer. Samples were powdered in preparation for XRD analysis using a mortar and pestle, and double-sided tape was used to affix the resultant powder to a glass slide for mounting in the diffractometer. Scans were carried out at a speed of 0.08 deg/sec within a range of 2θ = 20-120°.

3.2.4 Optical Microscopy

Alloys were sectioned using an Allied High Tech low speed saw with low-concentration diamond metal-bonded wafering blades, mounted in Bakelite resin, and polished to a 0.03 micron finish with alumina polishing media. Optical microscopy was conducted on solution treated and quenched samples using a Leica DM2500. These samples were etched using a modified Kroll's reagent (10% HNO_3, 8% HF, 82% H_20) to reveal the grain boundaries and precipitates. ImageJ analysis was conducted on optical and SEM images to characterize phase fractions.

3.2.5 Scanning Electron Microscopy (SEM)

Alloy samples in the solution treated state as well as the aged state were sectioned, mounting in Buehler KonductoMet, and polished to a 0.03µm finish for microstructure analysis. For SEM and EPMA, a silica finishing polish was used in order to avoid any surface contamination by alumina slurry that may interfere with composition readings. Scanning electron microscopy (SEM) was conducted using a FEI XL-40 FEG-SEM, using 15 kV accelerating voltage, spot size of 4.0 and working distance of 10mm. Energy dispersive spectroscopy (EDS) was also conducted on this system in spot, line, and mapping modes in order to visualize the distribution of alloying elements throughout the microstructure.

3.3 Alloy Processing

3.3.1 Thermal Processing

Solution treatment of alloy samples was carried out using a custom built vertical tube furnace with drop-quenching capability. The system was built around a Centorr CM 1700 Split VTF with an alumina tube, vacuum, and gas system for heat treatment of samples in an oxygen gettered flowing Ar environment. Samples were heated at a rate

of 9°C/min and quenched into agitated water directly from the hot zone of the furnace to retain the solution treated microstructure to room temperature. Aging of samples was accomplished through hydrogen torch encapsulation in quartz tubes under Ar environment, heating in an ATS 3150 box furnace, and furnace cooling. Samples were solution treated and aged for two hours, at temperatures detailed in the following chapters.

3.13.1 Sample Machining

The 250g buttons were first sectioned into large pieces using a Leco MSX205M cutoff saw, then sectioned into thin (2-4mm) plates using an Allied low-speed saw using low-concentration diamond metal bonded wafering blades (60-20095). The low-speed saw enabled very precise cuts to be made, which is essential in the fabrication of small compression samples. Grinding and polishing of samples was carried out using a Leco Varipol VP-50 grinding wheel, grit papers from 60-1200 grit, and polishing cloths with alumina and silica polishing to achieve a 0.03μm finish for microstructure analysis samples. Mechanical testing samples were polished to a 5μm finish to minimize friction between the sample faces and the platens used in compression testing.

Initial experimental compression samples were fabricated using these tools in addition to a planer to produce 2x2x3mm rectangular samples with parallel faces. Samples from the 250g buttons were machined using electric discharge machining (EDM) wire cutting by Triad EDM in Dunnellon, FL. For compression samples, cylinders with a diameter of 2.5mm were cut from the as-cast alloys, heat treated, then cut, ground, and polished into the appropriate geometry, as depicted in Figure 3-1. EDM was conducted by Joseph Hy Hyatovik from specifications programmed via AutoCAD drawings. A schematic of the dogbone dimensions is illustrated in Figure 3-2, with final

sub-size specimen pictured in Figure 3-3. In this way, reproducibility was maximized between different alloys and machining operations.

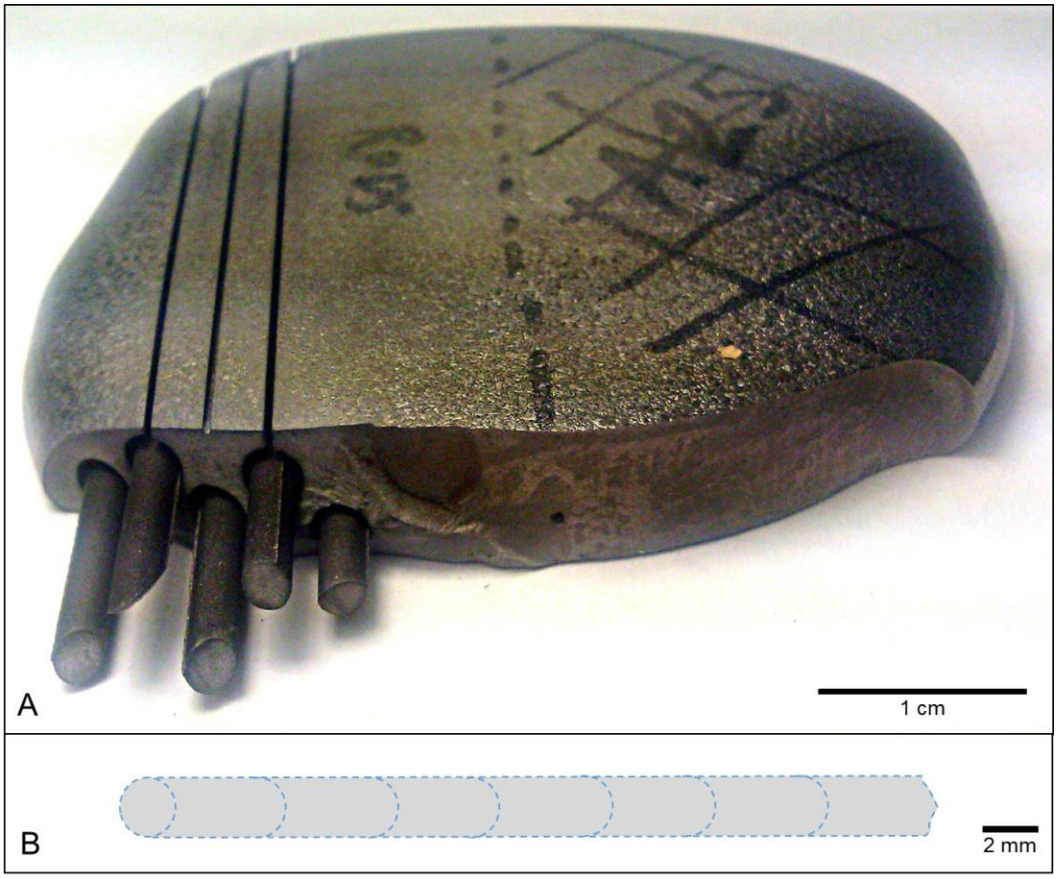

Figure 3-1: Images illustrating fabrication of compression samples. A) Cylinders cut from 250g button via EDM, B) schematic of compression samples sectioned from these cylinders after heat treatment. (Courtesy of author).

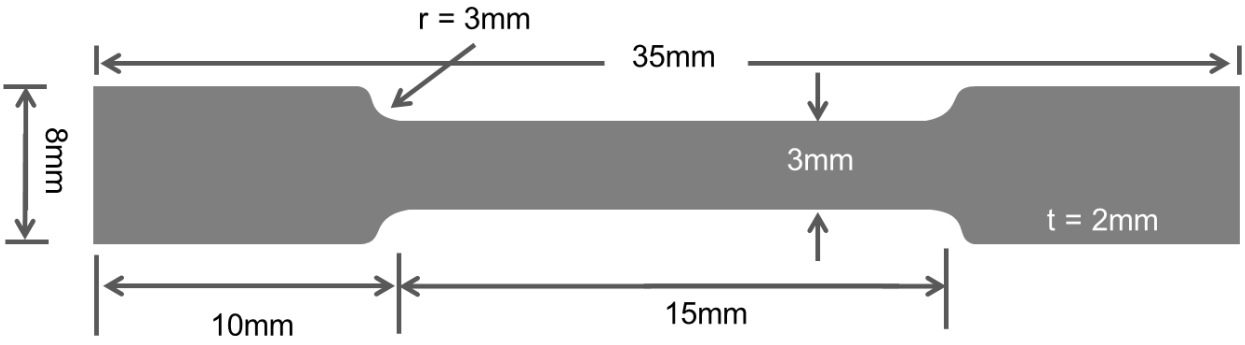

Figure 3-2: Schematic illustrating sample dimensions for sub-size tensile specimen, based on ASTM E8 standard [80]

Figure 3-3: Sub-size tensile sample, prepared for mechanical testing with 0.3μm polish. (Courtesy of author)

Tensile samples were also machined via EDM from the 250g buttons by Triad EDM. Plates as well as dogbones were cut at varying stages during the thermal treatment of these alloys, as further discussed in the tensile testing section (6.4) of this document.

3.4 Mechanical Testing

3.4.1 Compression and Tension Testing

Compression testing was conducted using an MTS 810 servo-hydraulic testing system with 2kip and 20kip load cells and attached Oxy-Gon FR200 universal materials testing furnace system. This system also has a Pfeiffer TCP300 turbo pump and Centorr Model 2A inert gas purifier. This system is capable of reaching 1600°C and being run under variable pressure inert oxygen-gettered argon environment. Graphite and silicon carbide compression fixtures were used for elevated temperature testing.

Compression samples were tested in two geometries – rectangular samples of size 2x2x3mm and cylindrical samples with 2.5mm diameter and a height of 3mm. Care was taken to ensure that these sub-size specimens had parallel faces, to minimize testing error. This was accomplished using a combination of planers and levelers during the grinding and polishing of the samples' faces, to a 0.03 micron finish with

same alumina polishing media used for metallographic preparation. Boron nitride spray was used on the silicon carbide platens as high-temperature lubricant.

Testing was run in displacement-controlled mode at a set strain rate, calculated from individual sample geometry. The controller for the MTS 810 system uses ramp rates programmed in terms of percent full-scale range (%FSR) per second, as well as a set stopping displacement, or 'Level' expressed in %FSR. This is because the system has interchangeable range and load cartridges that define the scaling of the standard +/-10 Volt readings from the load and stress transducers. For testing of compression samples, the +/- 0.5" Full-Scale displacement cartridge was used, with a 2kip (2,000 lb.) cartridge and load cell. In order to program the appropriate ramp for compression testing, the sample height (h_{sample}), desired final strain (ε_{final}), and desired strain rate ($\dot{\varepsilon}$) must be known in addition to the FSR of the current displacement cartridge in use. From this, a strain rate can be translated into %FSR/second, and final strain into %FSR. This is done using a form of the following equations [3-1 and 3-2], where care must be taken to maintain consistent units, and the forced negative value for level indicates compression. Displacement was measured via the system's built-in displacement transducer as well as an external single-arm extensometer, and data was compliance corrected using data fitted to the system's compliance at the temperatures and strain rates of interest for the high temperature compression testing.

$$Rate = \frac{(\dot{\varepsilon}/h_{sample})}{FSR} x100 \tag{3-1}$$

$$Level = -\left|\frac{(\varepsilon_{final} * h_{sample})}{FSR} x100\right| \tag{3-2}$$

Data acquisition was handled using a National Instruments (NI) analog-to-digital (A2D) converter and data acquisition (DAQ) card installed in a Windows system running

NI LabView software. The LabView virtual instrument was constructed to save the load, displacement, and strain readouts from the MTS 810 system to a text file, after converting displacement to metric units to allow for more precise measurement (there is a limitation on the number of significant digits saved to the right of the decimal place). Post-test data analysis and interpretation was conducted using a combination Microsoft Excel and WaveMetrics Igor Pro software packages, with custom macros for baseline subtraction and compliance correction of data when necessary.

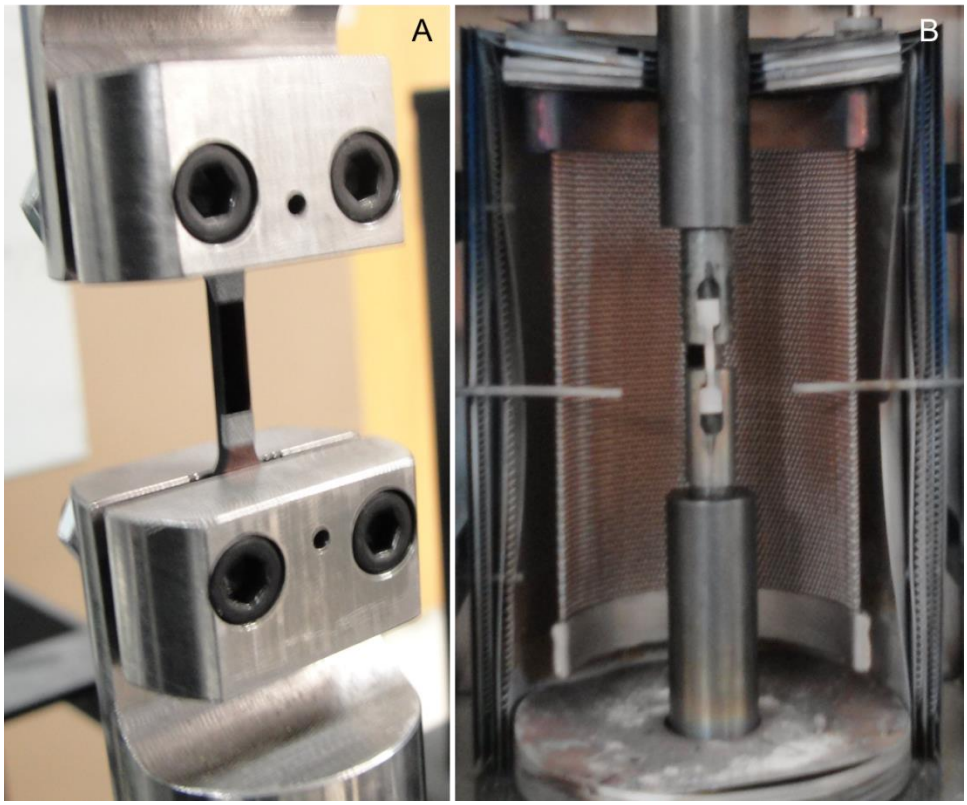

Figure 3-4: Photographs of tensile specimen loaded in grips. A) Tensile specimen loaded in vice-style grips for room temperature testing; B) Specimen loaded in collar-style grips for elevated temperature testing. (Courtesy of author).

Tensile testing at high temperature was conducted on the aforementioned MTS system, with collar-style grips, and room temperature testing was conducted on an Instron electro-mechanical load frame, using custom-machined vice-style grips, pictured

in Figure 3-4. Displacement was measured using a laser extensometer, calibrated before every set of testing, and measurements of samples were taken before and after testing to verify machine readout.

3.4.2 Loading and Operation for High Temperature Testing

High temperature compression testing under inert environment requires a few addition considerations when compared with room temperature testing. In addition to high temperature fixtures and lubricants, the samples required specific preparation and loading. After cleaning samples, they were loaded between the platens with the MTS controller in displacement control. This allows for precise loading and alignment of the small samples and the load on the samples can be monitored as the sample is put under a small amount of compression (5-10 MPa). The furnace O-ring is cleaned, greased, and the furnace is closed and sealed. The furnace chamber is then evacuated using the turbo pump then filled with the inert gettered argon gas to about 10 psi below ambient pressure. This procedure is repeated four times to clear the furnace chamber's environment, then the furnace is pressurized to positive 2psi, regulated by relief valve. At this point, the error on the load control module is zeroed and the system can be switched to load control while still under hydraulic power. The furnace is then heated to the desired temperature at a rate of 20-30 °C/min. Holding the sample in compression under load control during heating allow for the hydraulic actuators to compensate for thermal expansion of the sample and fixtures without applying additional pressure on the sample. Once the furnace has reached the desired temperature, it is allowed 20 minutes to equilibrate before switching back to the displacement controller and running the desired testing program.

Tests were run at 700 and 800°C at nominal strain rates of 10^{-3}, 10^{-4}, and $10^{-5}s^{-1}$, under displacement control. Testing profiles were programmed as ramp functions with displacement rate and final displacement level expressed in terms of percent full scale range (FSR). Compression testing was conducted using the +/- 0.5 inch FSR module, with strain rate calculations carried out using a combination of MathCAD and MS Excel. Furnace temperature is measured and regulated by two independent thermocouples which keep the testing chamber within 1°C of the set point. System compliance was determined at these temperatures and strain rates and used to correct the measured displacement results of all compression testing. An external extensometer with +/-0.016 inch FSR was used for finer strain measurement.

After testing is completed, samples were unloaded to approximately 100MPa and the system was returned to load control before the furnace is cooled. In this way, neither the sample nor platens will fall into the furnace heating elements upon cooling and contraction of the fixtures and sample. Once the furnace has cooled to room temperature, gas flow is stopped, the system is returned to displacement mode, and the furnace is opened. At this point, the sample can be removed and sectioned for microstructure analysis.

CHAPTER 4
ALLOY SELECTION AND HEAT TREATMENT DESIGN IN TI-AL-NB-(CR-MO) ALLOYS

Traditional alloy development cycles last approximately 20-30 years from initial investigation to implementation in industrial settings. One way to reduce the amount of time needed to develop, evaluate, and implement a new alloy system is through the use of computational tools for use in alloy design and selection. In this method of alloy development, specific compositions and microstructures can be targeted in order to produce the desired properties, and the number of experiments can be greatly reduced by first predicting microstructure development and alloy performance through the use of thermodynamic and science-based modeling. In this work, thermodynamic prediction capabilities are leveraged in order to select specific alloying ranges and inform thermal treatments required to produce the targeted microstructures.

4.1 Computational Analysis on the Effect of Nb on Phase Transformation Behavior

The ThermoCalc software platform [81] provides a powerful tool for thermodynamic calculation for the understanding of material properties and processes, allowing the user to simultaneously explore process variables such as alloy chemistry and temperature. In collaboration with Professor Hans Seifert's research group, an optimized Ti-Al-Nb ThermoCalc database, developed by Cupid et al [38] was used to calculate alloy phase equilibrium and relevant processing characteristics such as the relative contributions of Ti and Nb to phase transformation temperatures as well as to help select heat treatment temperatures necessary to produce the desired microstructural morphology.

In order to meet the objective of producing a very fine, disconnected γ + σ microstructure through thermal processing, a high temperature single phase β-phase region is required, as well as a lower-temperature γ + σ phase region that could be produced upon quenching and aging [10, 15]. The initial retention of β-phase upon quenching is important in preventing any phase transformations upon cooling, the scale and morphology of the final microstructure can be controlled via the subsequent aging step, allowing for production of finer microstructure scale than possible through equilibrium phase transformations [1, 10, 82]. The aging treatment temperatures and times can also be selected in order to modify the microstructural scale, with increased nucleation and slower growth kinetics at lower temperatures being favorable to the production of fine γ + σ morphology. In this way, strength should be increased by the Hall-Petch mechanism [19, 21], as well as the ductility by the microstructure refinement and separation of σ-phase regions [14, 16, 19, 40, 73].

It should be noted that all calculations in this chapter are performed in the absence of Cr and Mo. Ternary Ti-Al-Cr and Ti-Al-Mo databases are in the process of being assessed by Professor Hans Seifert's group and combined with the Ti-Al-Nb database to produce quaternary and quinary databases [38, 65, 66]. These alloying additions will affect the thermodynamics and kinetics of the reactions taking place in this system, thus it is possible that actual transformation temperatures in these alloys will be offset from those calculated in this section. However, since optimized databases of this higher-order system are not currently available, these predictions based upon the optimized ternary database calculations are the most appropriate way to model potential alloy behavior.

Initial selection of 45 at% Al was fixed in order to enable a wide range of compositions and phase fraction flexibility. Previous work has shown that alloys in this range have the ability to retain β upon quenching [10, 15] and the potential for improvement of environmental protection with increased Al content [83]. By leveraging the optimized Ti-Al-Nb database for ThermoCalc [38], compositional ranges of interest within the Ti-Al-Nb system were identified. A calculated isotherm at 1000°C, Figure 4-1, shows there is an elevated temperature γ + σ phase field. Furthermore, there exists a range of compositions where it is possible to keep σ-phase content below approximately 30%, which should aid in retaining disconnected σ-phase morphology [1, 14, 40].

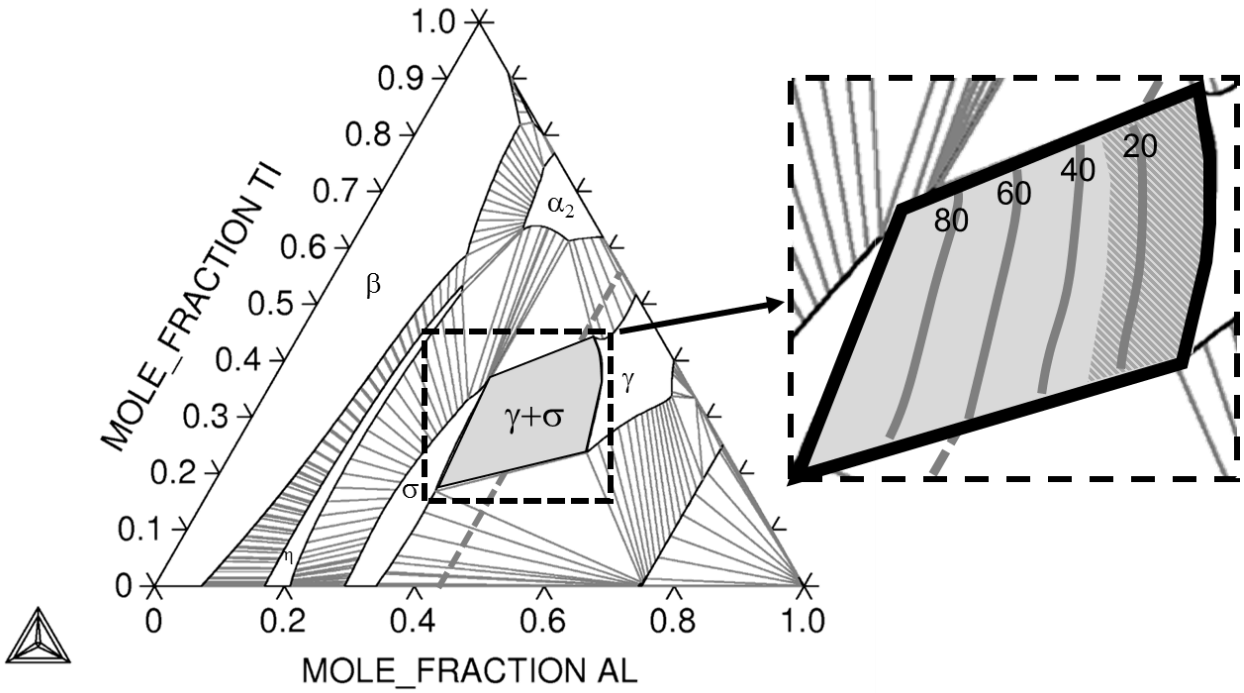

Figure 4-1: Calculated Ti-Al-Nb Isotherm at 1000°C with γ + σ phase field and 45at% Al line highlighted [38]. Insert indicates γ + σ phase region overlaid with calculated lines of equal phase percent σ-phase; targeted region of <30% indicated as shaded region.

Taking these constraints into account, an isopleth at 45 at% Al was calculated to determine temperature regimes for each of the phases of interest for microstructure development in this alloy system. Plotting this isopleth yields a section of the ternary, illustrated in Figure 4-2, which shows a region from approximately 15-25 at% Nb in which both of these alloy requirements are met, and transformation temperatures were calculated for alloys with 15, 20, and 25 at% Nb, as summarized in Table 4-1.

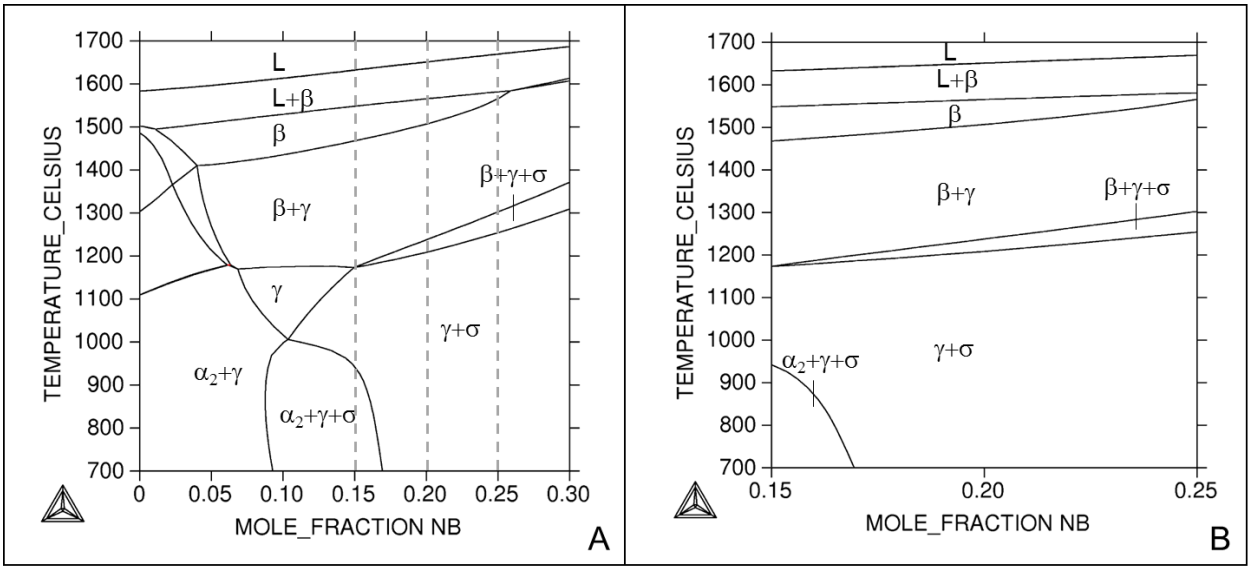

Figure 4-2: Isopleth sections of Ti-Al-Nb ternary along 45 at% Al indicating compositions which meet microstructure development requirements. A) 0-30 at% Nb; B) Targeted 15-25 at% Nb range showing high-temperature β-phase with lower temperature γ + σ phase field. Calculated using ThermoCalc [38].

Table 4-1: Phase transformation temperatures upon heating (°C), calculated from ThermoCalc Ti-Al-Nb database [38]

at% Nb:	15	20	25
β → β+L	1540	1560	1580
β+γ → β	1460	1505	1560
β+γ+σ → β+γ	1175	1230	1300
γ+σ → β+γ+σ	1175	1205	1250

In order to solution treat the alloys they should be heated to a temperature above the final solid state transformation temperature (β + γ → β), and below melting. These solution treatment temperatures are calculated to be in the range of 1460-1540°C, 1505-1560°C, and 1560-1580°C for alloys with 15, 20, and 25 at% Nb, respectively. Aging temperatures for these alloys should be below the lowest temperature solid state transformation reported in Table 4-1 (γ+σ → β+γ+σ), but the phase transformation of interest is the metastable transformation from β → γ+σ, so further work must be done to determine the lower limit for the aging temperature in these alloys.

4.2 Phase Fraction and Driving Force Predictions for Aging Treatments

Using the ThermoCalc software platform, the equilibrium phase fractions of γ, σ, and β phases can be calculated upon cooling for each of the specific ternary compositions. Looking at the phase fraction analysis for the alloys at either end of the range, with compositions of 40Ti-45Al-15Nb and 25Ti-45Al-25Nb (at%), it can be seen that these alloys have equilibrium γ and σ phase fractions that do not change dramatically in the range of 900-1000°C and 700-1100°C, respectively (Figures 4-3 and 4-4). More importantly there is a temperature regime in which these phases are mutually stable. One key difference in the phase fraction analyses is that for the 15 at% Nb alloy there is nucleation of the α_2 phase at temperatures below about 950°C, where this phase is not present in the 25 at% Nb alloy. This is consistent with the calculated isopleth section at 45Al, and by referencing that calculation, it is seen that the nucleation of the α_2 phase is only potentially relevant in the development of the 15 at% Nb alloy. Due to this factor, if a sample is to be aged into a two-phase γ + σ microstructure, it should be at temperatures above 950°C.

Another key difference between the 15 and 25 at% Nb alloys is the phase fraction of γ and σ in the potential aging temperature regimes. The 15 at% Nb alloy has a calculated σ-phase fraction range of 0.22-0.23 at 900-1000°C, while the 25 at% Nb alloy has a higher σ-phase fraction range of 0.37-0.4 at 700-1100°C. The higher calculated content of σ-phase is consistent with expectations based on the relative locations of these compositions in the γ + σ phase field on the calculated isopleth (Figure 4-2). Increased stability of σ-phase fraction with respect to temperature paired with the absence of α_2-phase nucleation at lower temperature may make increased Nb concentration more favorable for aging treatment and production of the two-phase γ + σ microstructure in this ternary system. Both of these alloys also have a high temperature single-phase β region, with a decrease in the single-phase temperature stability regime with increase in Nb content. Now that the presence of all required phases has been calculated, predictions regarding aging behavior can be made.

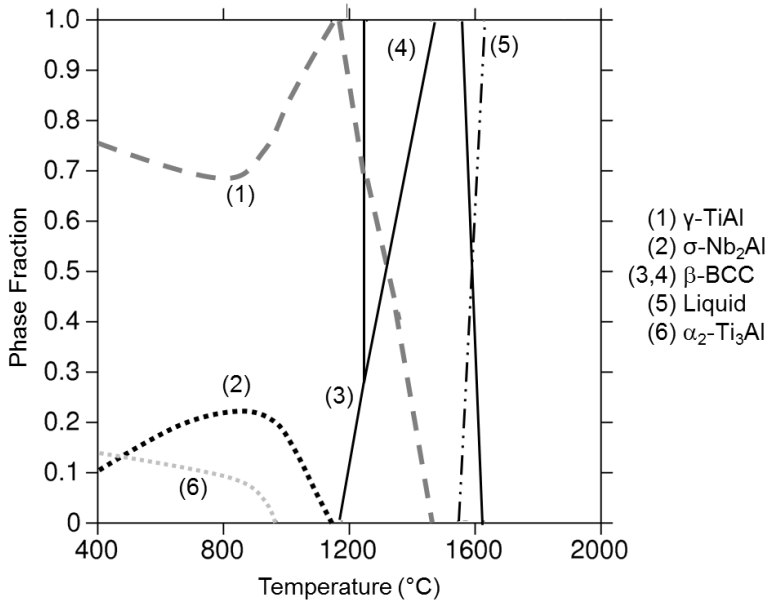

Figure 4-3: Phase fraction of stable phases with respect to temperature in Ti-45Al-15Nb alloy, calculated by ThermoCalc [38].

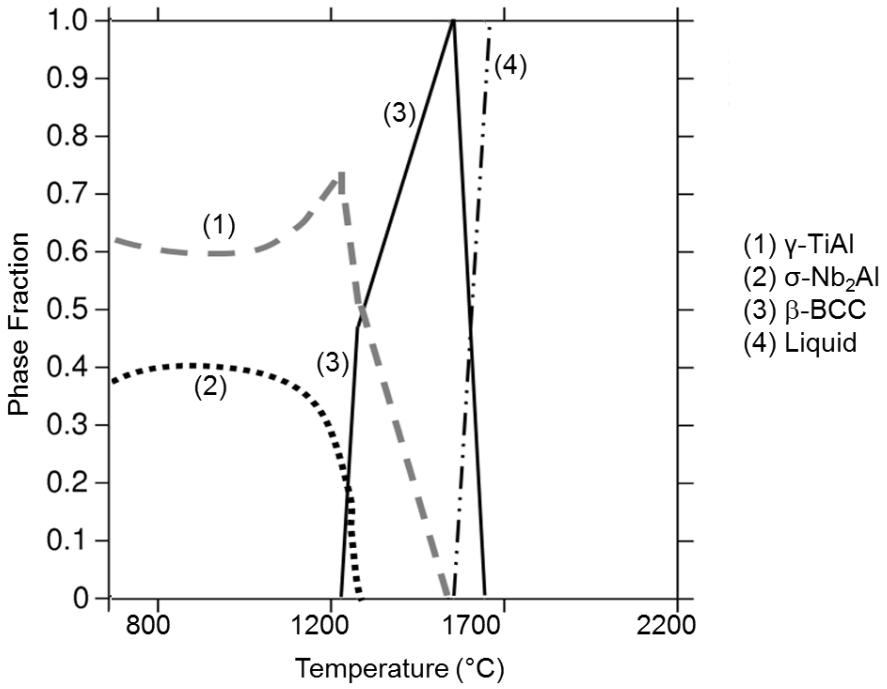

Figure 4-4: Phase fraction of stable phases with respect to temperature in Ti-45Al-25Nb alloy, calculated by ThermoCalc [38].

As previously discussed, the aging of these alloys will occur from a solution treated and quenched in metastable solid solution β-phase. In order to predict how nucleation and growth may occur during the aging of these alloys, the change in driving force for nucleation of γ- and σ- phases from a metastable β-phase was calculated. This information can be used to indicate what type of microstructure can be achieved, since high driving force for nucleation results in a denser, more uniform distribution of precipitates in the microstructure, while lower driving force for nucleation results in a less precipitate-dense microstructure due to fewer nucleation sites [21]. It was seen that there is very similar driving force for nucleation of both γ- and σ- phases throughout the entire temperature range over which the calculation was conducted, as presented in Figure 4-5.

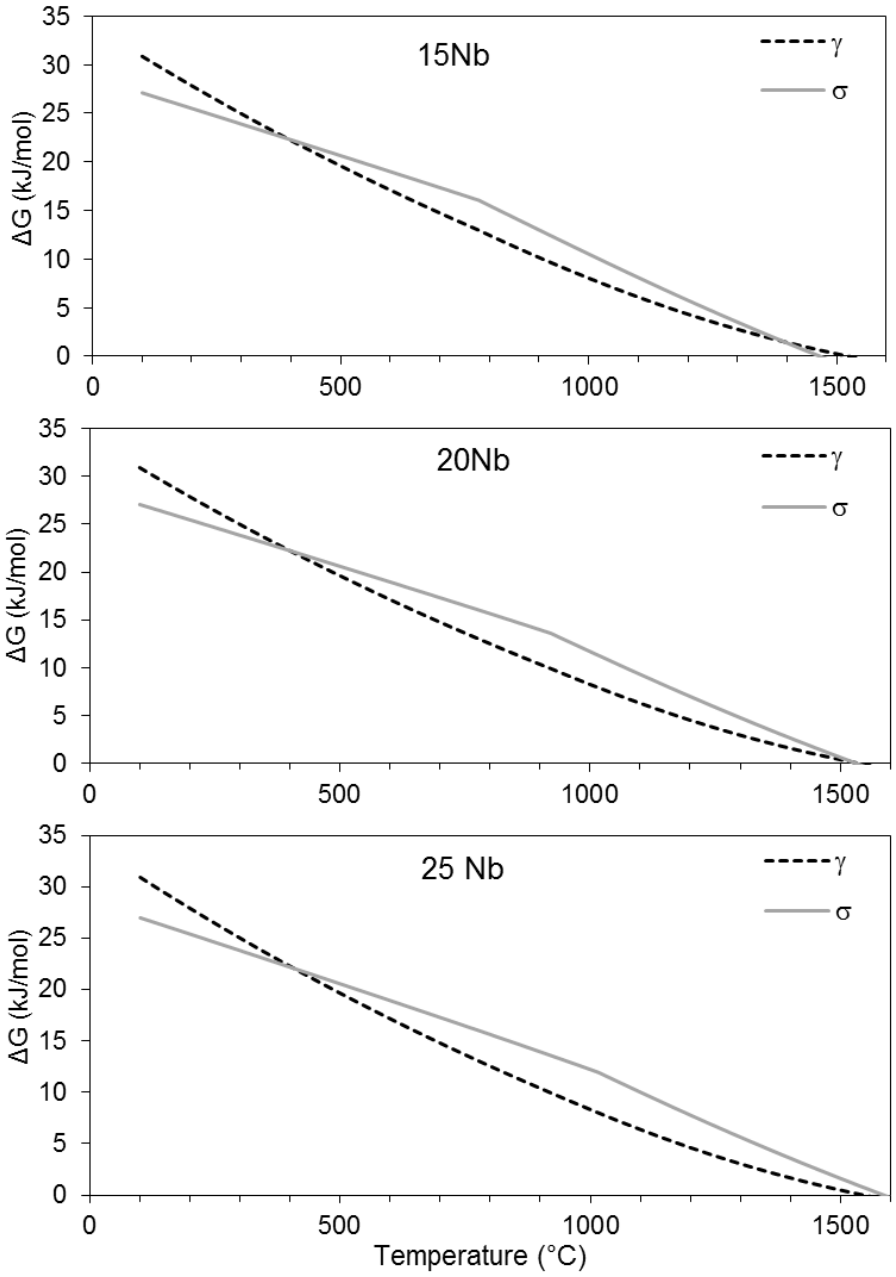

Figure 4-5: Driving force for nucleation of γ- and σ-phases from metastable β with respect to temperature for 15, 20 and 25 at% Nb alloys, calculated by ThermoCalc [38].

There is slightly higher driving force for nucleation of σ-phase for the majority of the temperature regime above 400°C, and with increasing Nb, this driving force increases slightly. These calculations assume an artificially stabilized β-phase, so it

predicts driving forces for nucleation at temperature above both γ- and σ-phase stability regions. In an experimental setting, the β-phase is more stable at these temperatures, so these nucleation events will not actually occur, but the relative driving forces can be used to give insight into nucleation behavior. Using this information to compare driving forces at various temperatures shows that at lower temperatures there is a higher driving force for nucleation, which would result in finer microstructural scale.

Also important is the fact that at all temperatures below about 400°C, there is a higher driving force for nucleation of the γ-phase. This could indicate that even with very fast cooling rates, the driving force for γ-phase nucleation would be significantly higher than at elevated temperatures, and could lead to its nucleation. The differences in driving forces can be used to understand what would happen without the effects of kinetics or crystal defects as a first step in understanding what may occur in the alloys experimentally.

As previously mentioned, in order to accomplish microstructure control in this alloy system, it is important to have control of the precipitation behavior of γ- and σ-phases. From these ternary phase diagrams, and isopleth sections (Figures 4-1, 4-2), we are able to predict that in order to meet all of the required alloy characteristics (β at high temperature, γ + σ at lower temperature) the Nb content must be kept within approximately 15 - 25 at.%. In order to develop a fine two-phase microstructure, it is integral to quench the single phase β to room temperature to increase the driving force for nucleation, which results in a finer, more uniform microstructure after aging in the γ + σ region, resulting in enhanced alloy performance [10, 16]. While these predictions allow for a satisfactory understanding of ternary alloy behavior, it has been

experimentally determined that the addition of β-stabilizing elements such as Cr can be essential in the retention of β-phase. It has been demonstrated that additions of about 5at% Cr to a high-Nb Ti-Al-Nb alloys stabilizes the β-phase and enable it to be retained upon quenching after solution treatment [10], and that up to 1 at.% Mo may improve high temperature microstructural stability due to its slow diffusion rate in this system, which limits the kinetics of phase transformations, while Mo also acts as a β-stabilizer [8, 65, 84].

The effects of variations in Ti, Al, or Nb can be calculated using ThermoCalc [38], and though the addition of quaternary and quinary alloying elements cannot be predicted using the same database, the calculations can be used as a guide for alloy design. These additions, along with variation in Nb content, necessarily affect the driving force for phase transformations and requiring the measurement of transformation temperatures in the quinary alloys currently under study. As it is not the focus of this work to undertake the optimization of quaternary and quinary ThermoCalc databases, the ternary calculations prove a sufficient first approximation of alloy behavior for initial selection and design work. More information about the quinary alloys of interest can be obtained experimentally and compared with the ternary calculations in order to determine the effect of alloying additions of Cr and Mo on phase transformation temperatures, and whether they have any effect on the trends predicted with respect to varying Nb concentration.

4.3 Experimental Analysis on the Effect of Nb on Phase Transformation Behavior

In the previous section, phase transformation temperatures were established for the Ti-Al-Nb ternary alloy system. These calculations will be verified experimentally

using DSC. Due to the low amount of Mo and Cr additions, it is anticipated that they will minimally affect and alter the phase transformation sequence from that predicted using computational thermodynamics.

Previous work has shown that the addition of Cr to a ternary Ti-Al-Nb alloy causes the suppression of the γ + σ → β phase transformation upon heating, as well as the temperature of the reverse reactions upon cooling [10]. The addition of 5 at.% Cr did not affect the β→γ transformation temperature upon equilibrium cooling of the alloy; however the temperature at which σ-phase nucleated was reduced by approximately 100°C. In this work, it has been seen that the addition of Cr and Mo suppress the transformation temperatures by an average of 50 - 100°C upon heating. Of particular interest for microstructure development is the temperature range in which γ + σ will co-precipitate from the metastable β phase, which is necessary to select an appropriate aging temperature.

Table 4-2: Transformation temperatures (°C) measured via DSC for quinary alloys (addition of 5 at% Cr, 1 at% Mo), compared with transformation temperatures for ternary alloys calculated via ThermoCalc Ti-Al-Nb database (in parenthesis)

at% Nb:	15	20	25
β → β+L	1475 (1540)	1475 (1560)	1550 (1580)
β+γ→ β	1310 (1460)	1330 (1505)	1475 (1560)
β+γ+σ → β+γ	1075 (1175)	1175 (1230)	1250 (1300)
γ+σ → β+γ+σ	1075 (1175)	1130 (1205)	1195 (1250)

The initial heating cycle from the DSC data (Figure 4-6) was used to determine the temperatures at which the as-cast microstructures, which solidify as a mixture of non-equilibrium phases due to the fast cooling rates, transform into the high temperature β phase and its subsequent melting temperature. These samples were cycled several times to determine the equilibrium phase transformations. Cycled curves

can be found in Appendix B, and it was observed that transformation temperatures for equilibrium transformations remain stable, while the initial exothermic peaks are diminished or do not appear for the subsequent cycles. This indicates that they are metastable phase transformations. Of primary interest is the final transformation before melting occurs, which is the transformation to single-phase β. After determination of this temperature range for all alloys, each alloy was solution treated at their respective β-phase temperatures and water quenched to retain this phase to room temperature.

Similarly, the first DSC heating cycle of the quenched alloy was used to study the ($\beta \rightarrow \gamma + \sigma$) phase transformation from the metastable β-phase, so that aging treatments may be designed. From this heating curve it is seen that the first exothermic peak upon heating corresponds to the γ-phase nucleation while the second is the σ-phase. The multiple endothermic peaks at higher temperatures correspond to the dissolution of these two phases and the re-introduction of β-phase upon heating, and the final plateau is the single-phase β region. The identity of these peaks has been confirmed in previous research [10, 23, 39] and phase identification was conducted in the regions of interest using XRD analysis, presented in Chapter 5. These transformation points are illustrated in Figure 4-7 and the results of thermal analysis are summarized in Table 4-2, and compared with transformation temperatures calculated using the ternary ThermoCalc database.

From the DSC results it can be seen that all transformation temperatures in the transformation sequence upon heating ($\sigma + \gamma \rightarrow \beta + \sigma + \gamma \rightarrow \beta + \gamma \rightarrow \beta$) increase with increasing Nb content, with the most significant increase in the range of 20-25 at.% Nb. That is, the temperature of all equilibrium phase transformations increase with Nb

content. Additionally, it is observed that the temperature range over which γ + σ phases are stable increases, while that for β-phase decreases with increasing Nb content.

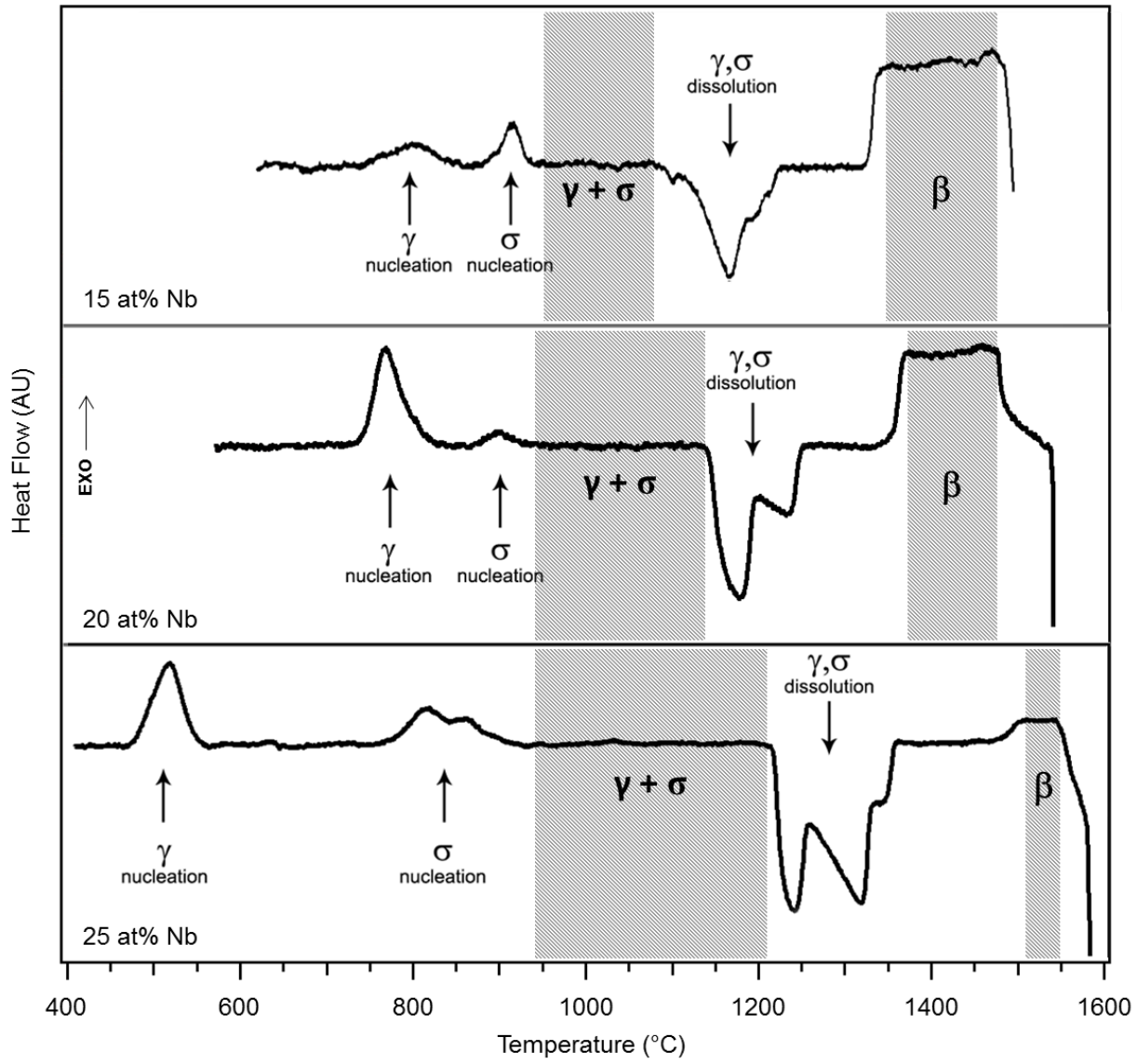

Figure 4-6: DSC data upon initial heating of alloys with 15, 20, and 25 at% Nb from metastable β-phase, indicating γ- and σ-phase nucleation and dissolution peaks, as well as γ + σ and β-phase stability temperature regimes

These trends are consistent when comparing quinary Ti-Al-(Nb,Cr,Mo) alloys with the calculated ternary Ti-Al-Nb isopleth section, which show upward sloping phase boundaries with increasing Nb content for all phases in the ($\sigma + \gamma \rightarrow \beta + \sigma + \gamma \rightarrow \beta + \gamma$

$\rightarrow \beta$) transformation path in this Nb-content range. The sole exception is a larger increase between the higher Nb content alloys than in the ternary system. This can be explained by the β-stabilization effects of Cr and Mo additions as, it has been seen that by adding 5 at% Cr to ternary Ti-Al-Nb alloys, transformation temperatures are depressed by 10-100°C [10]. By comparing the transformation temperatures measured in the DSC cycling of the quinary alloy with those predicted by the ternary calculations, as illustrated in Table 4-2, a similar depression in transformation temperatures is seen. Also evident is the decrease in the γ- and σ-phase nucleation temperatures with increase in Nb, with more pronounced decrease occurring in the γ-phase. While this large change in alloy behavior was not predicted based upon ternary calculations it could result in increased γ-phase formation upon quenching or aging treatments, especially in the case of the 25 at% Nb alloy.

Notable features of the DSC curves produced through heating of the metastable β phase (Figure 4-6) include the two exothermic peaks at temperatures below 1000°C in all three alloys tested, as well as multiple endothermic peaks which indicate solid state transformations occurring before melting. The irregular shape of the endothermic γ, σ dissolution peak upon heating of the 15 at% Nb alloy indicates a double peak, seen in Figure 4-6. As Nb content increases the γ + σ microstructure becomes more stable to higher temperatures and these peaks separate as σ-phase dissolves at higher temperature. Also as Nb content increases, the temperature at which each of the exothermic transformations occur decrease, with a larger decrease in the first reaction. The temperatures at which the endothermic dissolution reactions begin to take place increase with increasing Nb. The increase in dissolution temperature with Nb is

expected as the γ + σ phase region extends to higher temperature, so the β phase is not stable until higher temperature.

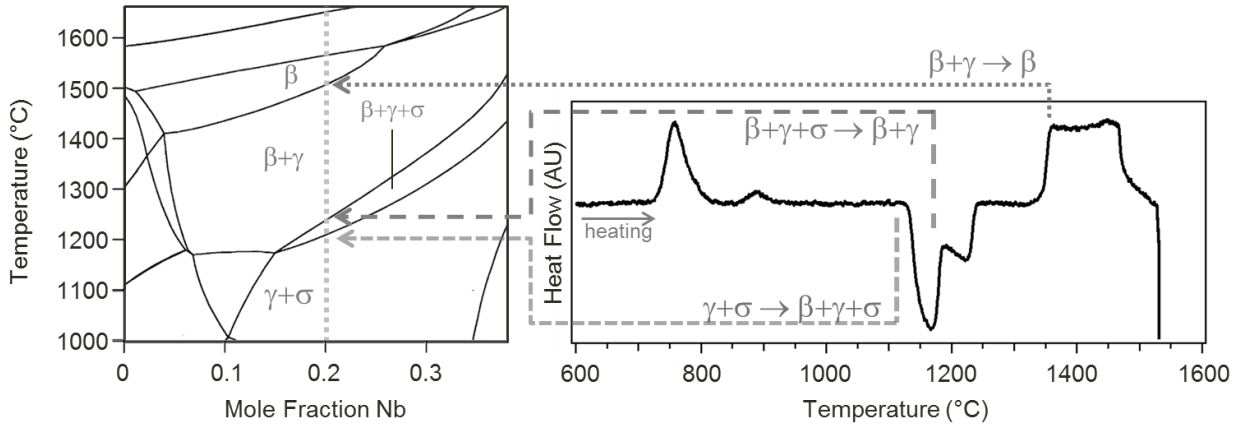

Figure 4-7: Comparison of DSC curves of Ti-45Al-20Nb-5Cr-1Mo alloy to calculated isopleth section for Ti-45Al-20Nb alloy, illustrating how calculated transformation temperatures were correlated with experimental results.

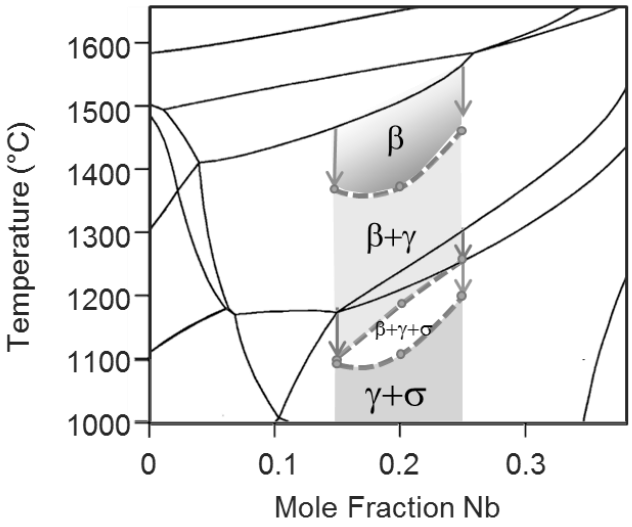

Figure 4-8: Phase transformation temperature measured in DSC upon heating overlaid on Ti-Al-Nb isopleth section at 0.45 Al (calculated via ThermoCalc [38]) illustration suppression of transformation temperatures with substitution of 5 at% Cr and 1 at% Mo for Nb

In the 25at% Nb alloy, evidence of a third peak is seen, manifesting as double exothermic peaks near 800 and 850°C, as well as an additional shoulder within the

dissolution peaks near 1350°C. One explanation for this additional peak is the non-equilibrium nature of these initial precipitation reactions. Since the β-phase is not stable to room temperature, the β → γ + σ reaction sequence is highly dependent on factors such as quenching rate, local alloy composition, and local precipitation sequence. It is thought that the additional peaks are due to the nucleation of the σ-phase directly from the β-phase, as well as at the β/γ interfaces.

The increased temperature is consistent with the additional energy requirement for homogenous nucleation of σ-phase from the remaining β-phase, and the higher dissolution temperature may be due to slight composition variation between σ-phase produced through homogenous versus heterogeneous nucleation. Upon further thermal cycling of the alloy (Appendix B) these additional peaks disappear since the β → γ + σ transformation occurs under equilibrium conditions and all of the σ-phase is of equilibrium composition. Thus, not only is there a lack of exothermic precipitation peaks, there is only a double peak in the temperature range of γ- and σ-phase dissolution. The effect of alloying additions on phase transformation temperature depression is summarized schematically in Figure 4-8, in which the shifted phase field boundaries are overlaid on the ternary isopleth calculated via the ThermoCalc Ti-Al-Nb database.

CHAPTER 5
MICROSTRUCTURE DEVELOPMENT AND STABILITY IN Ti – 45Al – xNb – 5Cr – 1Mo ALLOYS

In order to improve the high temperature performance of TiAl-based alloys, research has been performed to optimize alloy chemistry and microstructure, with two-phase microstructures being commonly employed in order to concurrently improve ductility and strength [1-4, 6-10, 58, 82]. In the previous chapter, alloy selection and heat treatment design was detailed in order to produce a method by which the microstructure can be controlled and tailored. It has been seen experimentally that slow-cooling of alloys in the Ti-Al-Nb system with Nb in the range of 10-15 at% will result in a coarse, γ-TiAl microstructure. Once these alloys have transformed fully to γ-phase it is not feasible to produce the σ-phase precipitate without heat treating for prohibitively long times. Even if heat treated for sufficiently long periods of time, the resultant microstructure would be coarse, yielding unfavorable mechanical properties, and not fully benefiting from increased strength and ductility that would be seen if precipitation strengthening with a fine dispersion of Nb-rich phase [1, 12-14, 40].

This has been attributed to the σ-phase which is known to be brittle and when it is the connected phase, acts to control the mechanical properties [1, 12, 14, 40, 43]. Therefore, it is the current goal to develop microstructures with a fine, disconnected σ-phase morphology, so that alloys may retain the benefits of precipitation strengthening without the detriment of low ductility experienced by high volume fraction σ-phase alloys.

5.1 Thermal Processing

In order to overcome the challenges in producing a fine, disconnected σ-phase morphology, two-stage heat treatments were designed such that alloys are solution

treated in the single-phase β solid solution region, water quenched to retain this metastable β-phase to room temperature, and subsequently aged in the γ + σ phase field regime, as illustrated schematically in Figure 5-1. Analysis of DSC data led to the determination of 1400, 1450, and 1500°C as solution treatment temperatures for alloys with 15, 20 and 25 at% Nb, respectively, as these temperatures lie fully within the single-phase β region. Likewise, aging temperatures of 1000, 950, and 1125°C were chosen for these alloys as these temperatures lie fully within the two-phase γ + σ regime. Solution treatment temperatures were selected to be at least 25°C above the β + γ → β transformation temperature, and 50°C below melting. In this way, it is ensured that the alloy will be within the single-phase β-region and will have adequate thermal energy available to fully solution treat. Aging temperatures were chosen to be fully within the γ + σ phase stability regimes of the respective alloys, as illustrated in Figure 4-6 in the preceding chapter.

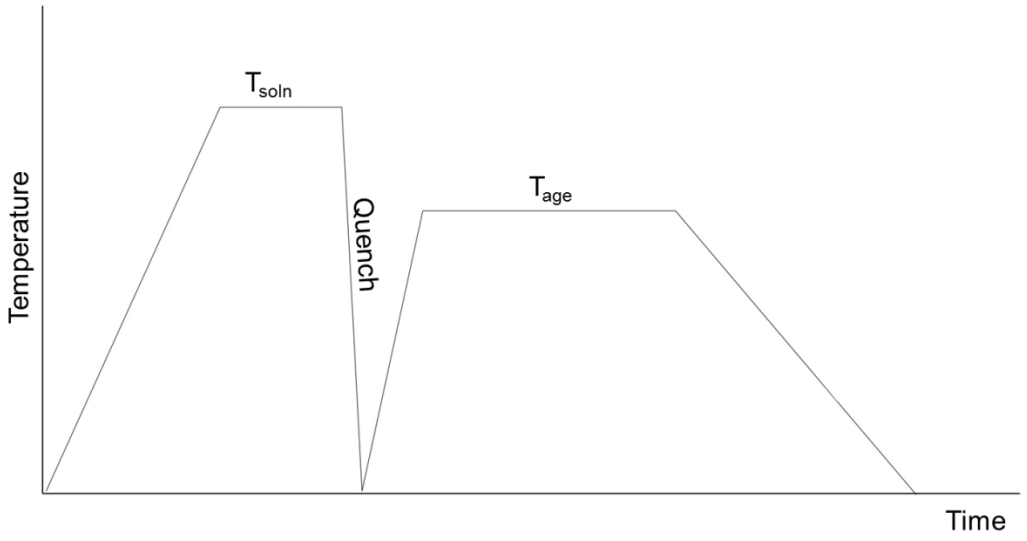

Figure 5-1: Heat treatment profile for experimental alloys. Temperatures for solution treatment (T_{soln}) and aging (T_{age}) determined by DSC analysis

5.2 Microstructure Development

5.2.1 Solution Treating and Quenching of Single-Phase β

For microstructure modification in this alloy system, it is essential to have control of the precipitation behavior of γ- and σ-phases. In order to accomplish this, it is important to quench the single phase β to room temperature, which is achieved though sufficiently severe quench as well as alloying additions [10, 39, 82]. In these ways, the thermodynamics and kinetics of the reaction are altered. The β-stabilizing elements, Cr and Mo, were added and have been proven effective in stabilizing this phase upon quenching [10, 82]. In previous research, solution treatment and quenching of ternary Ti – 44.5Al – 26.5Nb alloy produced a β+γ microstructure since the formation of γ-phase could not be suppressed upon quenching, but with the substitution of Cr for Nb, a Ti – 43.5Al – 22.5Nb – 5Cr alloy was able to retain solely β-phase to room temperature upon quenching [10].

While reduction in Nb content when compared with alloys in this system that have been studied in the past [1, 14, 40], lowers the amount of β-stabilizing elements present in the alloy, it also moves the composition towards a larger, lower-temperature area of the single-phase β-region, which improves the ability to solution treat. Solution treatment of alloys in the range currently under study produces a very large β-phase scale, with grain size on the order of millimeters. Etching of the quenched microstructures with a modified Kroll's reagent (10% HNO_3, 8%HF) reveals the location of the β-grain boundaries as well as the γ-phase, which resides mostly along β grain boundaries in the case of lower-Nb content alloys, as illustrated in Figure 5-2. This

relatively large microstructure scale is always seen after successful solution treatment of alloys in this system in the single-phase region and quenching.

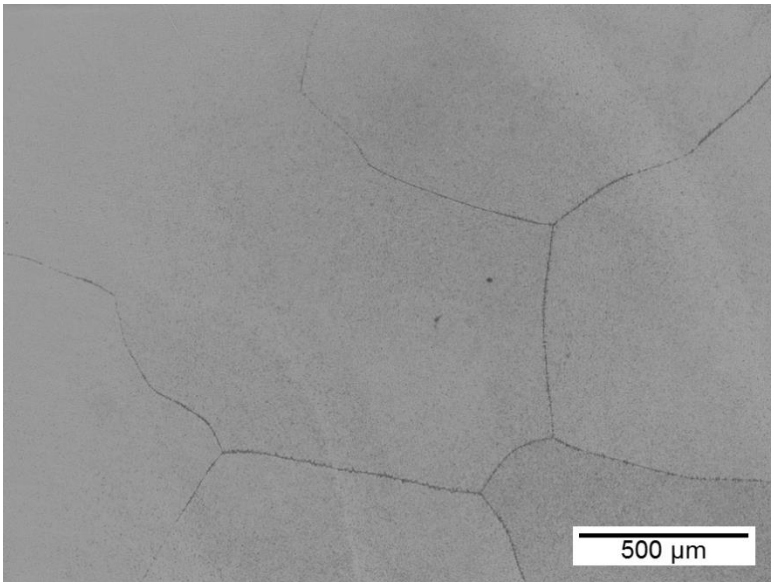

Figure 5-2: Etching reveals solution treated and quenched microstructure of alloy with 15 at% Nb, showing β-phase grain size and boundaries. (Courtesy of author)

In the alloys currently being studied, it was found that with increasing Nb content there is increased γ-phase formation at the β-grain boundaries. This is illustrated in Figure 5-4, with XRD analysis in Figure 5-3, and can be attributed to the fact that all phase transformation are shifted to higher temperatures, as summarized by the DSC results in Figure 4-6. Due to the higher temperature at which the γ-phase is stable relative to the β-phase, the alloy is in a temperature range favorable for the nucleation of γ-phase during the quenching process. Additionally, only the quenching media's starting temperature is controlled, so the quenching of 25 at% Nb samples from higher temperature compared to lower-Nb alloys (1500°C rather than 1400 or 1450°C) causes the quenching media to become warmer during the process. Even though the initial ΔT is higher for the 25 at% Nb alloy, this reduces the thermal gradient and cooling rate at

lower temperature when compared with quenching from lower solution treatment temperature. The less severe quench, paired with the high driving force for γ-phase nucleation leads to the formation of this phase throughout the microstructure.

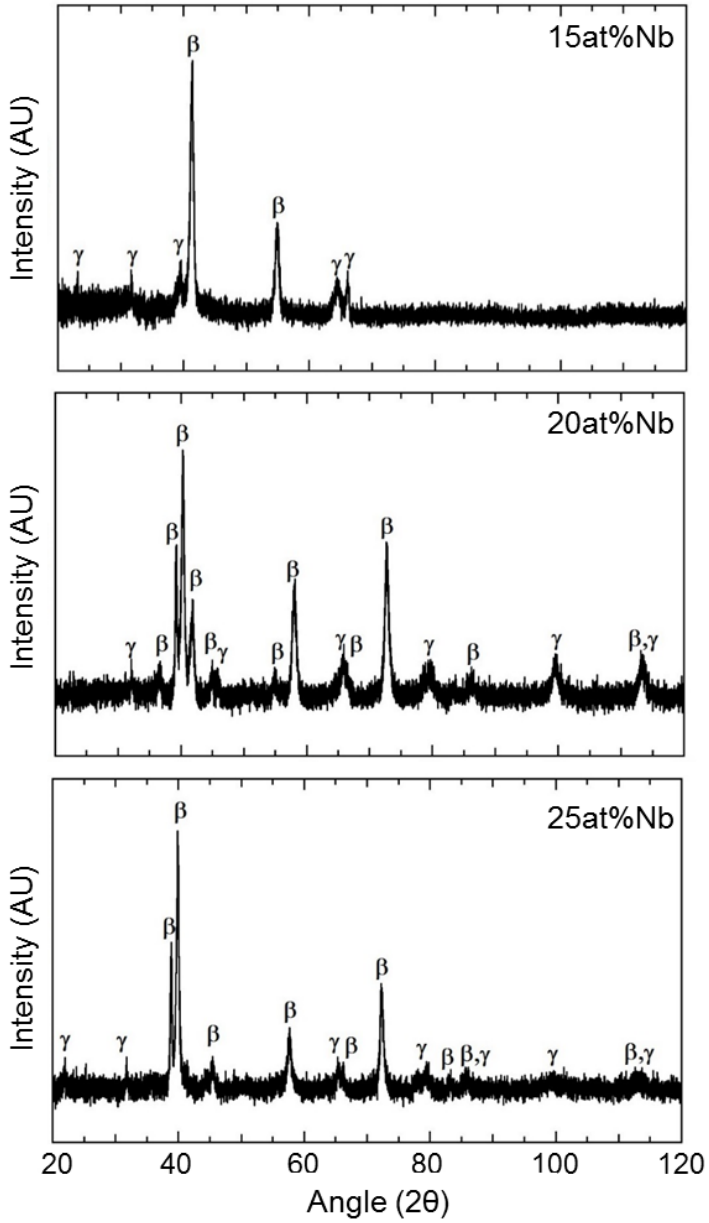

Figure 5-3: XRD of alloys with 15, 20, and 25% Nb in solution treated and quenched (S&Q) state, showing β+γ microstructure

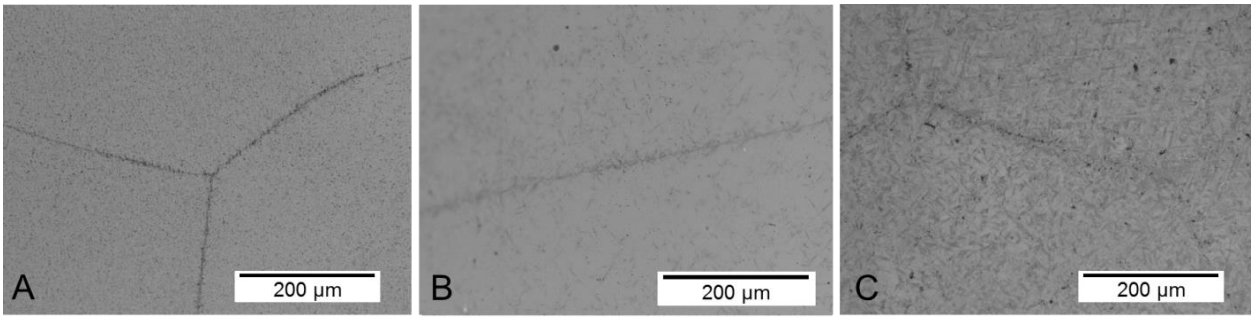

Figure 5-4: As-quenched microstructures of Ti-Al-Nb-Cr-Mo alloys showing increase in γ-phase scale and amount at prior β-grain boundaries with increasing Nb. A) 15 at% Nb, B) 20 at% Nb, and C) 25 at% Nb (Courtesy of author)

Successful retention of the β-phase to room temperature is dependent on several factors. First is the ability to rapidly cool the alloy samples to room temperature from the solution treatment temperature. The vertical tube furnace setup employed in solution treatment allows for quenching directly from the hot zone, minimizing the amount of cooling that can occur before the samples come into contact with the quenching media. Initial quenching was done into a bucket with room temperature water, which proved to be a sufficiently severe quench for the 15 at% Nb alloy, retaining β-phase to room temperature for samples below 3mm in thickness. Another factor affecting cooling rate is the sample's size. Samples that are very small, such as the 3 mm thick samples that were used in the initial rounds of heat treatment are suitably thin for quick conduction and removal of heat due to their large surface to volume ratio. Not only can heat be removed quickly from the larger faces, but thinner samples have lower amount of heat stored within the sample before it comes in contact with the quenching media, enabling the water to remain closer to its initial temperature throughout heat removal from the sample. Thicker samples (~5mm) were solution treated, and proved too thick for quick removal of heat by water quench, and more extensive transformation to γ-phase was observed. Similar results occurred when several thin samples were

solution treated and quenched at the same time, and this behavior holds for higher Nb concentration alloys, as illustrated in Figure 5-5.

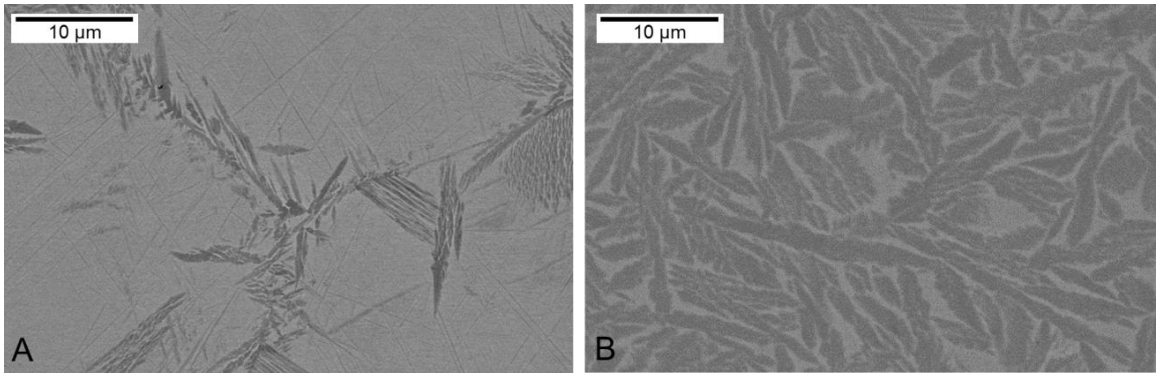

Figure 5-5: SEM images of solution treated and quenched 25% Nb alloy. A) Partial suppression of γ-phase transformation in thin (2 mm) sample, B) Growth of γ-phase in thick (6 mm) sample. (Courtesy of author).

Later solution treatments employed an agitated water quenching media, in which a water pump was used to force additional water into the quench bucket from a secondary reservoir and provide some amount of stirring to the quench media. This improved heat removal from thin samples, aiding the retention of β-phase to room temperature in 15 and 20 at.% Nb alloys. In these alloys, γ-phase is observed only where it heterogeneously nucleates on the β-grain boundaries, however in the 25 at.% Nb alloy, there is a much more even dispersion of γ-phase throughout the microstructure. This indicates homogeneous nucleation of γ-phase in addition to heterogeneous nucleation at the β-grain boundaries. The increased amount of γ-phase could be a result of either not fully solution treating the alloy, or of cooling somewhat before quenching. Observation of the β-phase grain structure of the 25 at% Nb alloy reveals that it is equiaxed and in the 1-2 mm range, similar to alloys with lower Nb

content. A microscopic view of this equiaxed structure can be seen in Figure 5-4, and a macroscopic image of the 25 at% Nb samples can be seen in Figure 5-6.

Figure 5-6: Solution treated and quenched 25 at% Nb alloy showing large equiaxed β-grains indicative of solution treatment in the single-phase region. (Courtesy of author)

If the heat treatment had occurred in the two-phase β+γ region rather than the single-phase β-region, then growth of β-phase into large equiaxed grains would not have occurred. Therefore it is probable that there was some cooling of the sample before quenching, or that cooling rate upon quenching was slow enough to allow for transformation to γ-phase before reaching room temperature. As discussed previously, due to the lower temperature at which the γ-phase nucleates upon cooling from the β-phase in the 25 at% Nb alloy, there is less undercooling upon quench in samples with higher Nb, leading to more favorable conditions for γ-phase nucleation and growth during quenching.

5.2.2 Aging to Produce γ + σ Microstructure

Of particular interest is the precipitation of the γ + σ microstructure from the metastable β-phase upon aging. This transformation is not well studied, but it is known that the γ-phase precipitates quickly from the prior β-phase grain boundaries, growing in

widmanstatten morphology, often upon quenching [23], as shown in Figure 5-5. The temperature regime in which γ + σ co-nucleation occurs has been determined through DSC, and is seen as the region between the two nucleation events and the first dissolution event upon heating of the metastable β, as summarized in Figure 4-6 in the previous chapter. Aging at a lower temperature within the γ + σ phase regime will result in finer microstructure due to the increased nucleation rate and slower grain growth, while higher temperature will result in decreased nucleation and faster growth, a trend that has been found to hold in similar alloy systems with 22.6 at% Nb [16].

5.2.2.1 Aged Microstructures

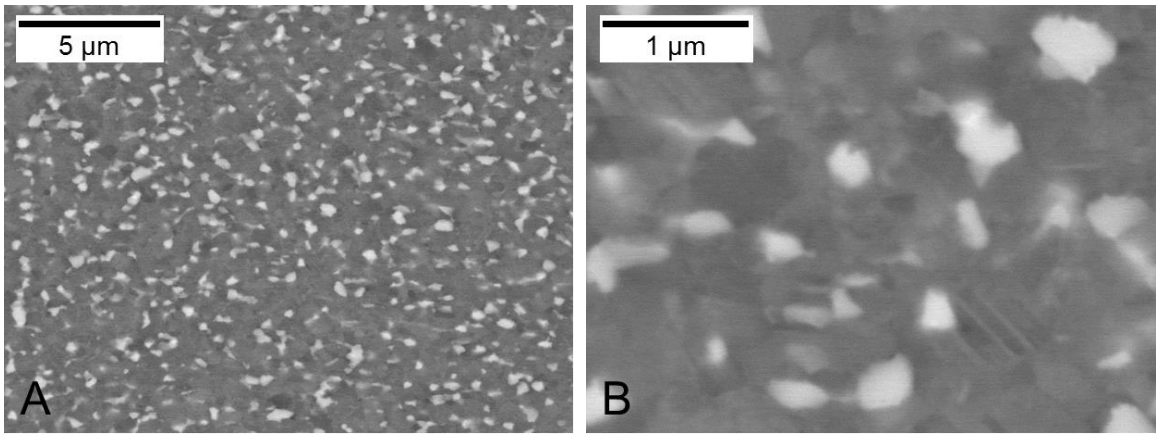

Figure 5-7: SEM micrographs of 15 at% Nb alloy aged at 1000°C for 1 hour. A) Ultrafine γ + σ microstructure produced via simultaneous nucleation of γ+σ from metastable β-phase; B) detail of σ-phase size and morphology. (Courtesy of author).

Initial aging treatments of the 15 at% Nb alloy at 1000°C showed successful development of the ultrafine microstructure, as illustrated in Figure 5-7. The morphology is greatly refined when compared with alloys where the β → β + γ transformation was allowed to occur first, such as it would with less β stabilization or upon slow heating to the aging temperature. The modification of microstructure through precipitation sequence will be discussed in further depth in the following sections.

Analogous heat treatments conducted on alloys with 20 and 25 at.% Nb showed increasing σ-phase content, as well as increased microstructure scale, as illustrated in Figure 5-9. With more availability of Nb, increased amount and growth of σ-phase is seen, and the microstructure transitions to one with a more connected σ-phase.

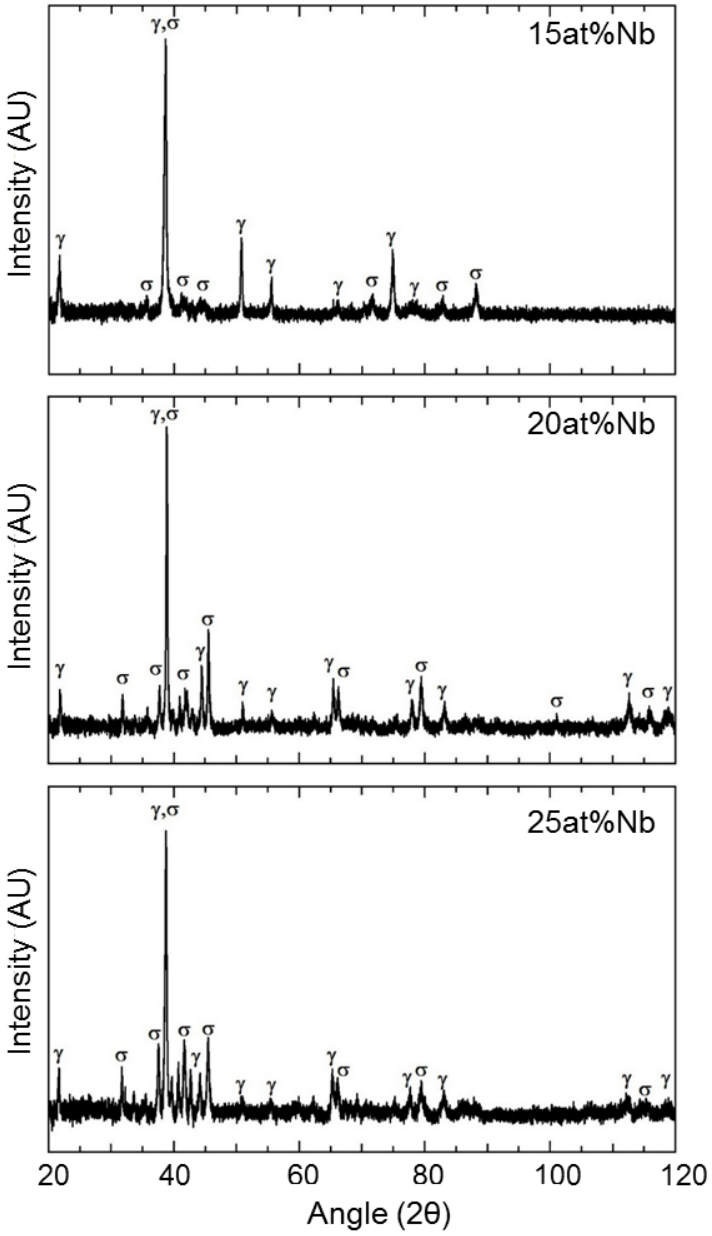

Figure 5-8: XRD of alloys with 15, 20, and 25% Nb in aged state, showing γ+σ microstructure

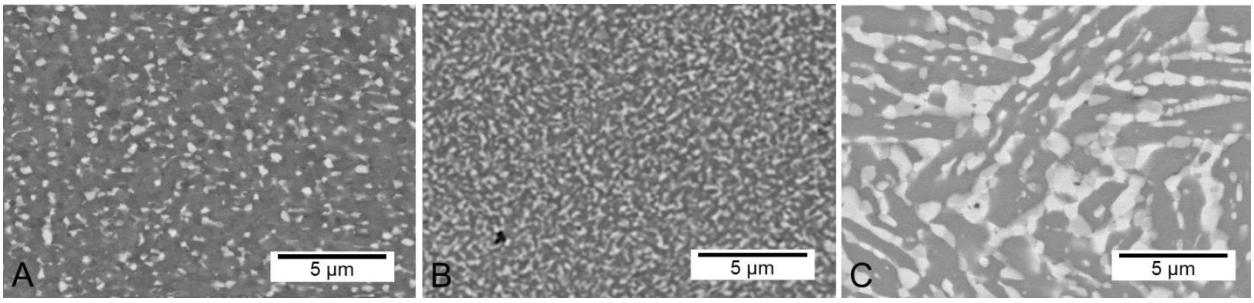

Figure 5-9: Change in scale and percent σ-phase of aged γ + σ microstructures with respect to Nb content. A) 15 at% Nb with12% σ, B) 20 at% Nb with 25% σ , and C) 25 at% Nb with 33% σ (Courtesy of author)

In order to verify the phases present in the aged state, XRD was conducted in the aged state, and peak identification revealed only γ- and σ-phases present in the microstructure, as seen in Figure 5-8. It was previously believed that there may be some residual β-phase in the aged microstructure or development of some α_2-phase as thermodynamic calculations show should occur in the 15 at% Nb alloy upon cooling. The lack of α_2-phase in the 15 at% Nb alloy indicates that the additions of Cr and Mo may stabilize the γ- and σ-phases such that further transformation will not occur upon near-equilibrium cooling. Alternatively, it could indicate that the alloying additions modify the thermodynamics of the system enough that the $\gamma + \sigma \rightarrow \gamma + \sigma + \alpha_2$ phase boundary line is shifted to lower Nb concentration or lower temperature. The information gained from XRD and DSC data suggest that the latter outcome is more probable. The $\gamma + \sigma \rightarrow \alpha_2 + \gamma + \sigma$ phase transformation is not observed in thermal cycling of the 15 at% Nb alloy, where this transformation would occur upon near-equilibrium heating and cooling, and all other phase transformation temperatures are depressed by 50 - 100°C.

5.2.2.2 Effect of Precipitation Sequence

If the microstructure is allowed time to transform fully to γ-phase by holding at lower temperature (400-500°C), σ-phase formation will be suppressed as σ-phase formation will be suppressed as σ-phase nucleation only occurs from metastable β despite the phase's stability in that temperature range [23, 39]. However, if aging is instead conducted in a higher temperature within the γ + σ region, precipitation of σ-phase is found to occur from the β-phase as well as from the γ/β interfaces after γ-phase formation. During this simultaneous γ + σ precipitation, presence of the σ-phase inhibits the coarsening of the γ-phase and provides additional nucleation sites for γ-phase during the aging of these microstructures.

The effect of precipitation sequence is evident from the microstructures produced in 15 and 20 at% Nb alloys, as seen in Figure 5-9. In these alloys, the formation of γ-phase was suppressed upon quenching, resulting in a very fine, equiaxed microstructure. It has been experimentally observed that upon quenching there can be formation of primary γ-phase laths at β grain boundaries, as seen in Figure 5-4. Upon aging of these alloys, the resultant microstructure reflects smaller, equiaxed γ-grains away from the prior β grain boundaries, while primary γ-phase that forming upon quenching e would coarsen [10, 23, 39].

Thermodynamic calculations conducted using an optimized ternary Ti-Al-Nb database [38] confirm there is higher driving force for nucleation of σ-phase from β-phase when increasing Nb content from 15 to 25 at%, as illustrated in Figure 4-4. For all compositions, the driving force for nucleation of σ-phase is higher than of γ-phase for most temperatures above about 400°C. In ternary alloys with 15 at% Nb content, it is

calculated that γ-phase will have higher driving force within the highest temperatures, indicating that the β → γ transformation should be seen first upon cooling. However, with 25 at% Nb it is calculated that the σ-phase should nucleate directly from the β-phase first upon cooling.

While driving force for σ-phase is higher than that of γ-phase for most of their stability regime, including the aging temperature range, these calculations only reflect the homogeneous nucleation of γ + σ from metastable β-phase, and does not take into account heterogeneous nucleation. It has been observed that upon quenching there is formation of primary γ-phase laths at β-phase grain boundaries. When quickly heated to the aging temperature, the primary γ-phase has enough energy to begin growth, while additional γ-TiAl will nucleate and σ-phase begins to precipitate from the β-phase as well as at the γ/β boundaries. However, evidence of this transformation behavior can be seen in the aged microstructure of 15 and 20 at% Nb alloys by observing differences between γ-phase morphology near and away from the prior β-phase grain boundaries. Near these boundaries, a coarser acicular morphology is seen, while away from them a very fine equiaxed structure is observed, consistent with growth of primary γ-phase at the grain boundaries as well as nucleation of γ-phase within the grains. This variation in microstructure scale and morphology with respect to location relative to prior β-phase grain boundaries is illustrated in Figure 5-10.

The scale and distribution of the σ-phase in the 15 at.% alloy are indicative of a combination of homogenous and heterogeneous nucleation. The fine, evenly distributed, disconnected σ-phase, seen especially in the 15 at% Nb alloy, indicates nucleation of σ from β-phase, and limits the γ-phase to a very fine scale. Additionally,

regions of elongated σ-phase precipitates can be seen, which indicate the formation of σ-phase at the γ/β interfaces after formation of γ-phase laths. This is illustrated in Figure 5-11, in which contrast within the γ-phase grains is due to electron channeling contrast, and some sub-surface σ-phase is visible. Additionally, the presence of annealing twins has been documented in γ + σ microstructures [12, 33], such as those potentially represented in Figures 5-19, 5-11, and 6-6 in the following chapter, which alter the contrast of the γ-phase grains in these micrographs.

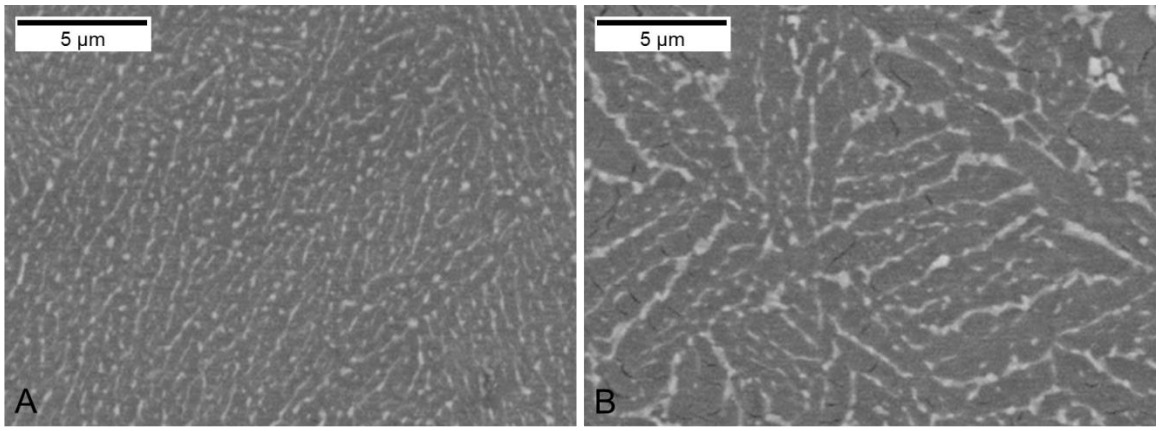

Figure 5-10: SEM micrographs of 15 at% Nb alloy. A) Fine microstructure away from boundary produced by simultaneous γ + σ nucleation, B) Coarse microstructure near prior β-grain boundary indicative of primary γ formation during quenching. (Courtesy of author).

It has been observed that γ-phase will continue to grow into large laths if unhindered, so it is thought that the nucleation of the σ-phase is responsible for retarding the growth of these laths, and providing additional locations for nucleation of γ-phase. Since σ-phase nucleates first, only the remaining β between σ-phase can transform to γ-phase. If instead γ-phase is nucleated first, as it is with slower cooling rate upon quenching, then σ-phase can only nucleate from the remaining β phase, leading to a coarser lath-shaped γ + σ microstructure. This morphological modification

is illustrated in Figure 5-12, which compares the aged microstructures of a sample of 15 at% Nb alloy that has been quenched into β-phase (Figure 5-12 A) to that of one allowed to partially transform to γ-phase upon quenching (Figure 5-12 B). During aging, competing nucleation and growth of both phases is occurring, so the order in which these reactions are allowed to occur plays a very strong role in the development of the alloy microstructure.

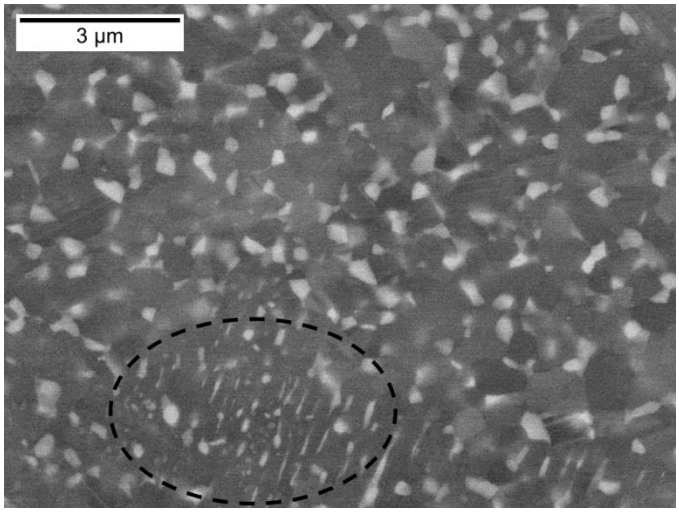

Figure 5-11: Microstructure of aged 15 at% Nb alloy showing variation in scale of σ-phase, indicating homogeneous nucleation in the majority of the alloy with some heterogeneous nucleation between γ-phase laths (highlighted). (Courtesy of author)

Enhanced β-phase retention results in finer, more uniform microstructure after aging in the γ + σ region, resulting in enhanced alloy performance [10, 16]. This fine microstructure is expected to result in higher strength alloys due to reduction in strain localization which would otherwise occur in regions of coarse γ-phase near prior β-phase grain boundaries [16]. Further discussion of the effects of microstructure morphology on mechanical properties will be presented in Chapter 6. In order to produce the ultrafine γ + σ microstructures seen in these alloys, the simultaneous

nucleation from the metastable β phase necessary, as can be clearly seen through observation of microstructure development, presented in Figures 5-4 and 5-9, where alloys with 15 and 20 at% Nb do not nucleate γ-phase upon quenching and produce an ultrafine microstructure, while the 25 at% Nb alloy nucleates γ-phase upon quenching and results in a much coarser microstructure, and a modified morphology.

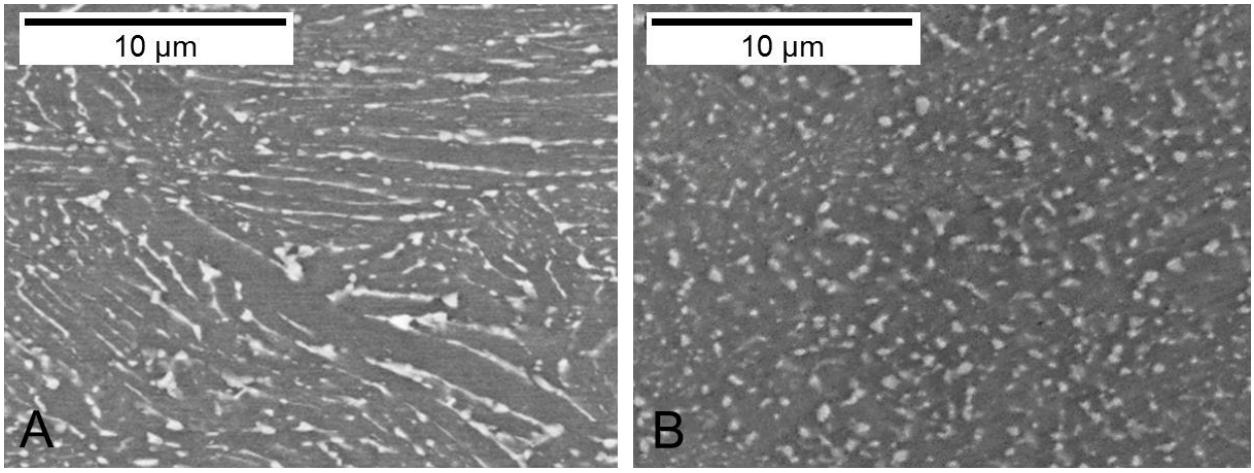

Figure 5-12: Effect of severity of quench on γ + σ microstructure development in 15 at% Nb alloy; A) γ-phase formed upon quenching coarsens into lath-shaped morphology, B) γ-phase nucleation suppressed upon quenching results in fine, equiaxed morphology. (Courtesy of author).

5.2.3 Long-term aging and microstructural stability

Aging treatment study was carried out by undergraduate University Scholar student Cameron Palmer on alloys with 20 and 25 at% Nb in order to determine the evolution of microstructure scale with aging time. Additionally, microhardness testing was conducted to correlate with effects on alloy strength and to determine peak aging times. Samples with 20% at Nb were aged at 950°C, and samples of 25% Nb alloy were aged at 1125°C, as they were for previous microstructure development, for times ranging from 10 to 10,000 minutes. Aged samples were air-cooled and polished to a

0.3 μm finish, and then Vickers microhardness was used to correlate the hardness of the sample to changes in alloy strength with aging.

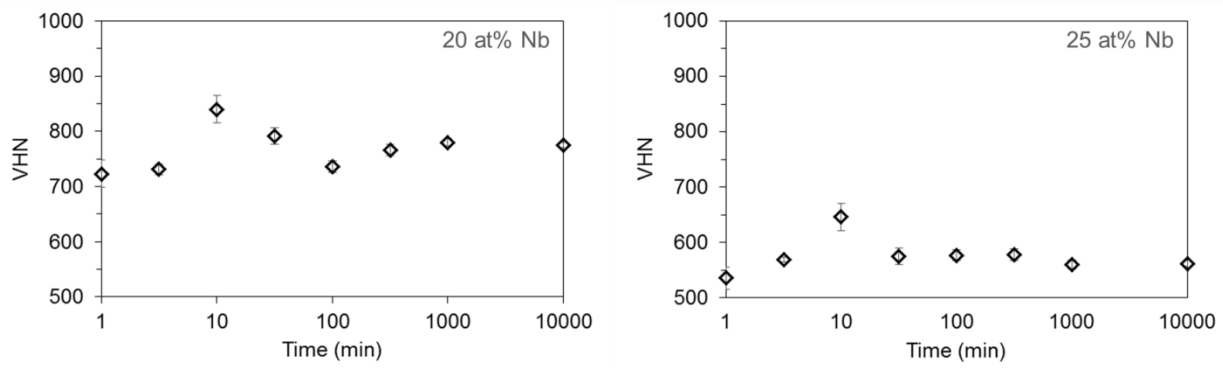

Figure 5-13: Effect of aging on microhardness in 20 and 25 at% Nb alloys. 20 at% Nb alloy aged at 950°C, 25 at% Nb alloy aged at 1125°C

It is important to note here that the grain size of the 20 at% Nb alloy are much smaller than that of the 25 at% Nb alloy, which may correlate to higher hardness values. In each alloy, there is a relatively short peak aging time, around 10 minutes of aging, which indicates a very short incubation time before nucleation begins. This is followed with a decrease in hardness values, indicating over-aging and then a leveling off of after this time, as summarized in Figure 5-13. A comparison of each of the alloys after 10 minutes and 1000 minutes of aging in illustrated in Figure 5-14. The short peak aging time can be attributed to a high driving force for nucleation of the γ + σ microstructure from the metastable β-phase and fast kinetics of this transformation. Since the β-phase is stable only at temperatures above 1330 and 1475°C for alloys with 20 and 25 at% Nb, respectively, there is a large driving force when these alloys are heat treated approximately 350°C below these temperatures, coupled with a large amount of energy available at these high temperatures. The decrease in hardness after 10 minutes is indicative of over-aging, which can be due to the increase in precipitate size and change

in interfacial coherency with the matrix [19, 21]. Additionally, the decrease in hardness of the 20 at% Nb alloy followed by an increase could be attributed to the dissolution of some metastable σ-phase precipitates, similar to a reversion process seen in some aluminum alloys [21], followed by the growth of stable σ-phase precipitates which strengthen the alloy.

Determination of peak aging time is important for microstructure development of an alloy, and can be used to produce the highest room temperature strength possible. However, for elevated temperature applications, the stability of the microstructure is of greater interest. It was observed that alloys were over-aged after the one-hour heat treatment that has been employed for microstructure development in these alloys, but more importantly the hardness values were relatively stable as aging time progresses. In the case of the 25 at% Nb alloy, this stability in hardness would not be expected due to the large change in microstructure scale, but could be attributed to the strengthening from the σ-phase and its size relative to the microhardness indenter. For the 20 at% Nb alloy, the stability in hardness is understandable due to the fact that microstructure scale remains relatively small. In order to determine longer-term microstructure stability, 20 at% Nb samples were aged for 10,000 minutes and it was observed that while there was some coarsening of the microstructure, it is not to the extent that would be expected for continuous growth of microstructure scale over an additional order of magnitude of aging time. Figure 5-15 shows SEM micrographs of the 20 at% Nb alloy after aging for 10,000 minutes which support that the material maintained relative stability in the microstructure as well as hardness.

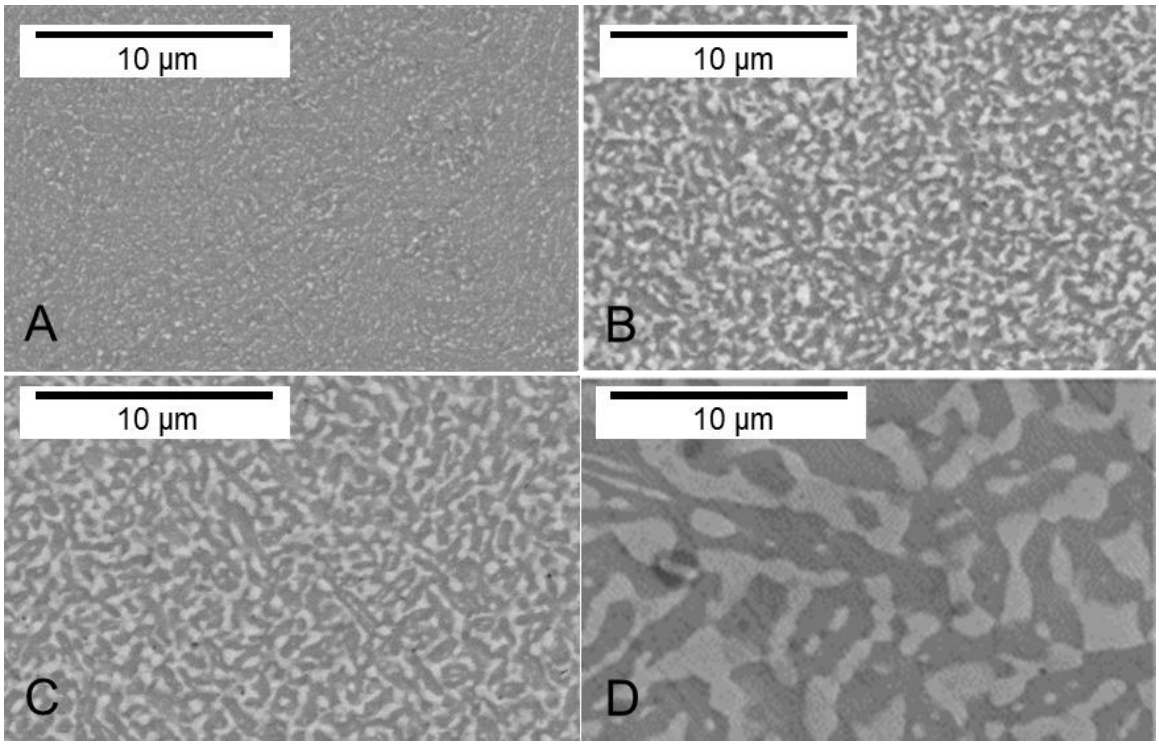

Figure 5-14: Effect of aging on microstructure scale for 20 and 25 at% Nb alloys. A) 20 at% Nb alloy aged at 950°C for 10 minutes, (B) 20 at% Nb alloy aged at 950°C for 1000 minutes, C) 25 at% Nb alloy aged at 1125°C for 10 minutes and (D) 25 at% Nb alloy aged at 1125°C for 1000 minutes. (Courtesy of author)

For both of these alloys, the γ + σ microstructure underwent coarsening between 10 and 1000 minutes, correlating with decreased hardness levels. However, even after 10,000 minutes of aging, grain size is limited to 1-2 µm for the 20 at% Nb alloy, and approximately 5 µm after aging the 25 at% Nb alloy for 1000 minutes. The goal of generating a relatively fine microstructure through solution treatment and aging was accomplished, and the aging study helped characterize that the strength may be retained at extended aging times, even well past peak aging time. Other mechanical properties would be altered by changes in microstructural morphology and scale over time, such as toughness and ductility, and this would be an appropriate focus for future work in this alloy system.

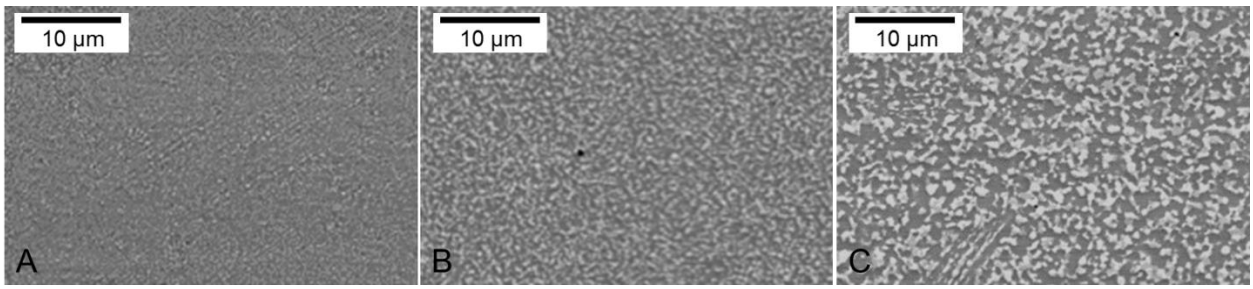

Figure 5-15: Effect of aging on microstructure scale for 20 at% Nb alloy aged at 950°C. Aging times of A) 10 minutes B) 1000 minutes, and C) 10,000 minutes. (Courtesy of author)

CHAPTER 6
MECHANICAL PROPERTIES OF TI-AL-NB BASED ALLOYS

6.1 Microstructure and Mechanical Properties

As discussed in the previous chapter, solution treatment in the single-phase βsolid solution region [15, 16, 23, 38] and subsequent quenching retains the β-phase, limiting the formation of γ-TiAl and allowing for better control over microstructural scale [10, 15, 23]. Aging in the two-phase γ-TiAl +σ-Nb_2Al region, can produce a homogenous, ultrafine microstructure made up of continuous γ-phase with disconnected σ-phase [10, 16, 23, 38], with a representative microstructure and XRD evaluation of the 15 at% Nb alloy illustrated in Figure 6-1.

In the Ti-Al-Nb system, it is known that Ti and Al form several intermetallic phases, as do Nb and Al [2, 4, 38, 79, 85]. It is also known that Ti and Nb have complete mutual solubility [79]. Additions of Cr and Mo are expected to have solubility with both Ti and Nb as well, due to their similar electronegativity and size [19, 21, 38, 65, 66]. The small additions of these alloying elements should offer some solid solution strengthening, but it is not expected to be as significant as the increase due to strengthening from precipitation of the Nb-rich σ-phase.

Microstructure morphology and scale are expected to have a significant effect on strength, as well as deformation and failure mechanisms in this alloy system, due to Hall-Petch, solid solution, and precipitation strengthening effects in addition to the known brittleness of the σ-phase [12, 14, 40] during low temperature deformation. Quantitative microscopy was performed using the ImageJ software to characterize σ-phase volume fraction and micrographs were analyzed to determine relative morphology of σ- and γ-phases. The 15 at% Nb alloy has γ-phase grains ranging from

0.1 – 1 μm in diameter and approximately 0.12 area fraction (A_f) of σ-phase particles ranging in size from approximately 50-500 nm, while increasing the Nb content to 25 at% increases the A_f σ-phase to approximately 0.33, with much larger, contiguous σ-phase ranging in size from 500 nm - 5μm.

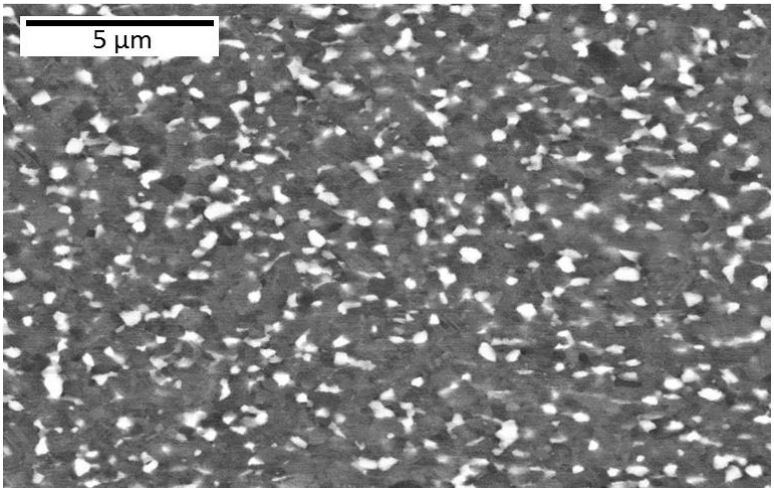

Figure 6-1: Representative γ + σ microstructure showing γ-TiAl matrix (darker gray) with disconnected σ-Nb_2Al particles (white). (Courtesy of author)

6.1.1 Flow Behavior

Initial compression testing was conducted on the 15 at% Nb alloy, and as shown in Figure 6-2, all flow curves show a linear elastic region followed by a transition to plastic deformation with no sharp yield point. All samples were tested to approximately 40% engineering strain, where tests were interrupted with no macroscopic failure of the alloy. At testing temperature of 800°C, changes in flow behavior as a function of strain rate are most discernible. At lower strain rates, a peak stress followed by flow softening is observed, as well as oscillations in the curve that increase in period as the strain rate decreases. However, at faster strain rates this oscillatory behavior is diminished. At 700°C there is a moderate increase in yield stress and a change from flow softening to work hardening behavior for compression at the highest strain rate. At both

temperatures, as the strain rate increases, the flow stress and work hardening rate increase. Compression of samples at 700 and 800°C yields stress exponents of 13.1 and 7.7 respectively, as illustrated in Figure 6-3 where they are compared with strain rate dependent strength of high σ-phase content alloys [1]. The 0.2% offset yield stress and maximum flow stresses of all tests can be found in Table 6-1.

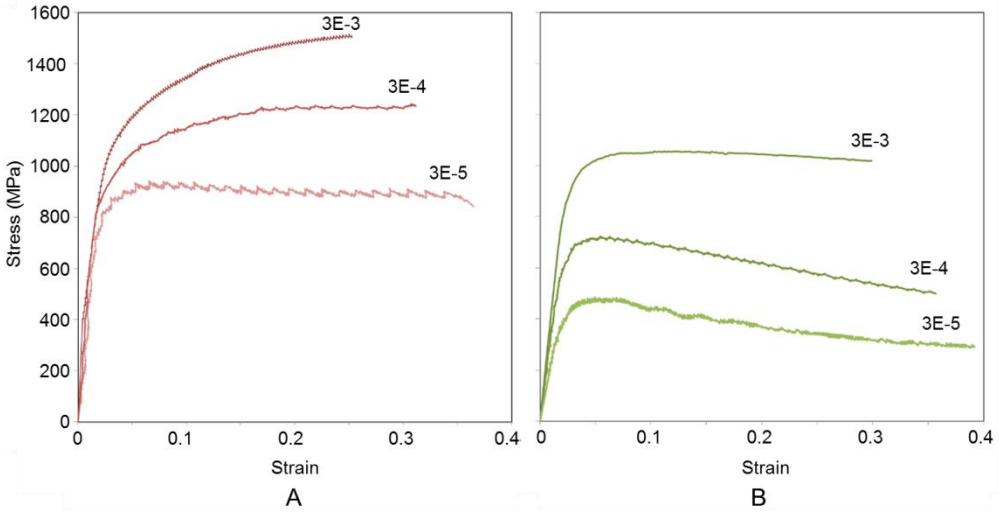

Figure 6-2: Compression testing results of 15 at% Nb alloy at strain rates of $3x10^{-3}$ to $3x10^{-5}$ s^{-1}. A) 700°C, B) 800°C

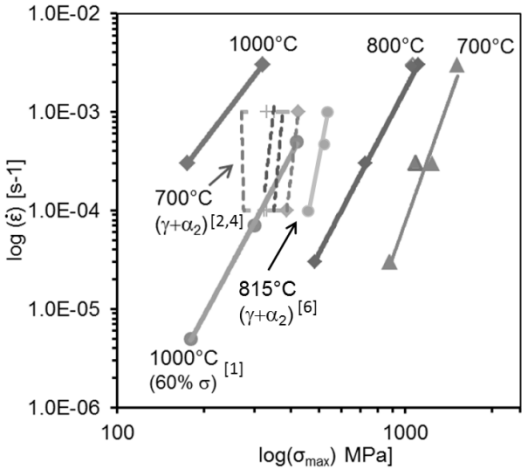

Figure 6-3: Strain rate dependence of strength, comparing results of current testing of 15Nb alloy at 700 and 800°C to TiAlNb alloy with $0.6V_f$ σ-phase [1] and typical values for alloys with γ+$α_2$ microstructure at 700°C [2, 4] as well as a high-Nb γ+$α_2$ alloy with improved high temperature strength at 815°C [6]

Table 6-1: Test temperature and strain rate along with the corresponding 0.2% offset yield stress and maximum stress (MPa) for 15 at% Nb samples tested in compression at 700 and 800°C

Temperature (°C)	Strain Rate (s^{-1})	0.2% Offset σ_y	σ_{max}
700	$3x10^{-3}$	1010	1510
	$3x10^{-4}$	840	1240
	$3x10^{-5}$	690	880
800	$3x10^{-3}$	780	1010
	$3x10^{-4}$	680	725
	$3x10^{-5}$	415	485

Compression testing of 20 and 25 at% Nb alloys at temperatures of 700, 800, and 900°C show similar trends with respect to strain rate, temperature, and flow softening. With increased Nb content, strength increases at all strain rates and temperatures tested. This can be explained by the higher amount of precipitation strengthening due to increased σ-phase concentration. However, at the highest strain rate and lowest temperature (700°C, 10^{-2} s^{-1}) the 20 at% Nb alloy shows limited compressive strain to failure when compared with other testing conditions, failing after only 5% true compressive strain. At the same strain rate at 800°C, the alloy accommodated over 50% compressive strain before failure. Under all other temperatures and strain rates tested, the tests were interrupted at approximately 50% engineering strain, at which point the flow behavior of the alloy was determined.

At testing temperatures of 700 and 800°C, the 25 at% Nb alloy fractured before 50% engineering strain. At 700°C, failure occurred in a nearly brittle manner at 10^{-2} s^{-1} strain rate, and total compressive strain at failure was between15 and 20% true strain at the slower strain rates. Increasing the testing temperature to 800°C increases failure strain to 15% at 10^{-2} s^{-1}, and to approximately 30% and 55% for strain rates of 10^{-3} and 10^{-4} s^{-1}, respectively. At this temperature, a peak stress followed by flow softening is seen, similar to lower-Nb content alloys at this temperature.

Table 6-2: Test temperature and strain rate dependence of 0.2% offset yield stress, maximum stress (MPa), and true compressive strain to failure (ε_f) for 20 at% Nb samples tested in compression at 700, 800, and 900°C

Temperature (°C)	Strain Rate (s^{-1})	0.2% Offset σ_y	σ_{max}	ε_f
700	10^{-2}	1300	1630	0.05
	10^{-3}	1220	1485	-
	10^{-4}	1080	1275	-
800	10^{-2}	1010	1210	0.4
	10^{-3}	820	900	-
	10^{-4}	590	635	-
900	10^{-2}	560	655	-
	10^{-3}	420	490	-
	10^{-4}	285	310	-

Table 6-3: Test temperature and strain rate dependence of 0.2% offset yield stress, maximum stress (MPa), and true compressive strain to failure (ε_f) for 25 at% Nb samples tested in compression at 700, 800, and 900°C

Temperature (°C)	Strain Rate (s^{-1})	0.2% Offset σ_y	σ_{max}	$\varepsilon_{failure}$
700	10^{-2}	1800	1960	0.01
	10^{-3}	1350	1770	0.13
	10^{-4}	1380	1780	0.17
800	10^{-2}	1280	1775	0.19
	10^{-3}	1060	1400	0.3
	10^{-4}	750	980	0.55
900	10^{-3}	625	750	-
	10^{-4}	265	280	-

At 900°C, there is a significant decrease in strength in both the 20- and 25 at% Nb alloys. This is evident in the drop in yield strength by nearly half between 800 and 900°C at all strain rates. The drop is even more exaggerated at the slowest strain rate in the 25 at% Nb alloy, in which the yield strength drops by approximately 65%. This drop can be attributed partially to the increased Nb concentration in this alloy, but the most important factor affecting the decrease in strength is the connected nature of the σ-phase. The microstructure of the 25 at% Nb alloy has increased σ-phase concentration, size, and contiguity when compared with lower-Nb alloys, as illustrated in Figure 5-7 in the previous chapter. Due to its more connected nature, the alloy behavior

is more controlled by the σ-phase as seen in previous research in high σ-phase alloys, where σ-phase is found to undergo a softening transition near 900°C [1, 12, 14].

6.1.2 Deformed Microstructure

SEM observation of the deformed microstructure of the 15 at% Nb alloy shows that it does not undergo significant coarsening during compression at 700 or 800°C when compared to the non-deformed microstructure as displayed in Figure 6-4. There was no fragmentation, pancaking, or flattening of particles normal to the loading direction, which were both observed in previous study of microstructures with 0.6 V_f σ-phase [1]. With the exception of microcracking, the deformed microstructure appears identical to the non-deformed microstructure. Microcracking was seen throughout the γ-phase and some cracking at the γ/σ interface in all samples, with microcracks opening at various angles with respect to the loading direction due to local re-orientation of strain due to the hard second-phase particles [86].

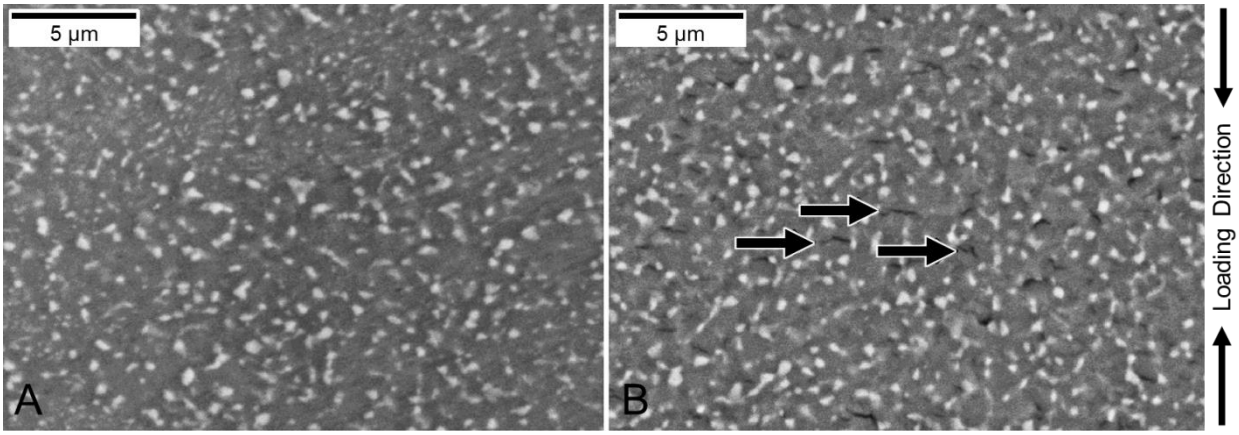

Figure 6-4: SEM micrographs of 15 at% Nb alloy before and after compression testing. A) Non-deformed sample; B) Sample deformed at 800°C, $3x10^{-4}$ s^{-1} to approximately 40% engineering strain. Arrows indicate microcracking in the γ-phase, which appears as the darker phase in these micrographs [82] (Courtesy of author)

6.2 Deformation mechanisms

Analysis of flow curves obtained at varying strain rates and temperatures can lead to insight into the deformation mechanisms that may be active in these alloys. The effect of strain rate on work hardening is evident in these alloys, especially in testing of the 15 at% Nb alloy at 700 and 800°C. Calculated stress exponents (reported in Appendix C) fall into the range of dislocation recovery mechanisms, which include dynamic recovery, dynamic recrystallization, interfacial sliding, and diffusion assisted dislocation motion [6]. This is supported by the flow curves, which indicate that dynamic recovery and recrystallization play important roles in deformation. These deformation mechanisms could be confirmed through targeted transmission electron microscopy (TEM) work, but the current testing setup does not allow for quenching of samples directly from the testing stage for analysis of interrupted tests. Since quenching is not possible, some of the dislocations that are present in a deformed sample will be annealed out upon furnace cooling to room temperature which would change the dislocation substructures.

Evidence of dynamic recrystallization can be seen most prominently in the flow curves of this alloy tested at 800°C and lower strain rates. At $3x10^{-5}$ s^{-1}, multiple oscillations in the flow stress can be seen as a function of increasing strain due to the nucleation and propagation of dynamic recrystallization waves through the material. Since at this strain rate one wave of dynamic recrystallization can be fully completed before next wave begins, oscillations in the flow stress are evident. At higher strain rates, the critical dislocation density required to nucleate dynamic recrystallization is reached before the material can completely recrystallize, so oscillations are not visible in the flow curves as the material is continuously being recrystallized.

Previous work with alloys containing 0.6 V_f σ-phase has shown that dynamic recrystallization occurs in both fine and duplex γ+σ microstructures, with TEM analysis showing γ-phase deformation by dislocation glide and twinning [1]. Due to the connected nature of the σ-phase in the 0.6 V_f alloy, high temperature deformation was controlled by σ/σ grain boundary sliding [1, 14], but by reducing the phase fraction and forming a discontinuous σ-phase, deformation is instead controlled by the γ-phase in the alloys currently under study, as evidenced by analysis of the deformed microstructure, which will be discussed in further detail in the following section. At 800°C the σ-phase acts as a hard phase, as it has been found in literature [1, 40] that it undergoes a transition to a deformable phase at temperatures above 900°C, as previously mentioned.

While deformation of this alloy is controlled by the properties of the continuous γ-phase, the disconnected σ-phase particles contribute to strengthening and limit the size of recrystallized grains. Similar to microstructure development upon aging of the alloy, the dispersion of ultrafine σ-phase particles will pin the γ-phase grain boundaries and limit coarsening [76]. Another benefit of σ-phase pinning is that the particles at the γ grain boundaries may reduce the amount of γ/γ interfacial sliding at elevated temperature. Since the γ/σ interface is not likely to be fully coherent, as dislocations attempt to slide along the γ/γ interface or propagate through the γ-phase they may be impeded by σ-particles that they can overcome through dislocation climb or Orowan looping. These processes are more difficult in this temperature regime when compared to γ/γ interfacial sliding, resulting in increased work hardening and retention of strength [2, 11, 19-21, 72].

The alloying additions Cr and Mo in solid solution may slow the growth of recrystallized grains and σ-Nb_2Al particles may exert grain boundary pinning [74]. As discussed in Chapter 2, particle stimulated nucleation (PSN) of dynamic recrystallization is observed in two-phase and dispersion-strengthened alloys, though it is unlikely to contribute significantly to nucleation of recrystallization in these alloys. Since second phase particles must be approximately 1 μm or larger to initiate recrystallization [76], and the largest σ-phase particles in the 15 at% Nb alloy microstructures are approximately 500 nm, with many smaller particles in the regime of 10-50 nm. However, the presence of the ultrafine σ-phase particles may have the effect of reducing the amount of strain required to initiate recrystallization by increasing strain in the matrix even though local dislocation densities are not large enough at the precipitate-matrix interface for nucleation at the particles. Since particles smaller than 1 μm have been found to retard recrystallization under certain conditions, systematic study would be required to determine the regimes of particle size and spacing in which recrystallization would be retarded or accelerated. At this point the effect of the σ-phase particles upon recrystallization is unclear, but it has been seen that they have a strong influence in the recrystallized γ-phase grain size through their pinning effect.

In higher Nb concentration alloys similar flow behavior is observed, with a peak stress at low strain followed by significant flow softening. The exceptions to this are samples tested at the fastest strain rate (10^{-2} s^{-1}) at 700°C. At this temperature, there is not sufficient time for the accommodation of deformation. That is, at this temperature and strain rate, dislocation generation and mobility is not sufficient for dislocation-

recovery mechanisms to be active, so the induced strain results in the opening of microcracks, and complete fracture of the samples.

6.3 Failure Mechanisms

The morphology of γ-phase in relationship to the reinforcing σ-phase is vital to understanding the deformation and failure behavior in these two-phase alloys, and analysis of deformed samples shows that microcracking occurs throughout the deformed microstructures. Cracking can be used as an indication of what types of deformation and failure mechanisms occur in this alloy, such as γ/γ or γ/σ interfacial sliding. Additionally, grain boundary incompatibility and internal stress could cause cracking within the γ or σ grain itself. In Figures 6-4 and 6-5, the cracks appear to be solely in the γ-phase, indicating that it is the strain-accommodating phase.

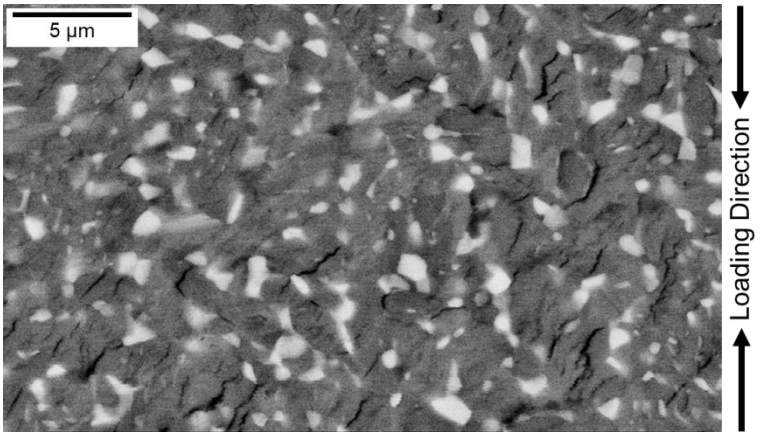

Figure 6-5: Detail of sample deformed at 800°C, $3x10^{-3}$ s^{-1} showing γ/γ and γ/σ interfacial microcracking. (Courtesy of author)

Dislocation formation during plastic deformation can be attributed the anisotropic nature of the γ-phase leading to the production of geometrically necessary dislocations at grain boundaries, in addition to dislocation pileup. Since compression testing is being carried out at elevated temperatures, competing recovery mechanisms would also be

active. Recovery mechanisms reduce the number of dislocations and amount of residual stresses [19, 74, 76], but when compressed to 50% engineering strain, there are still large enough stresses at the γ/γ interfaces to open microcracks.

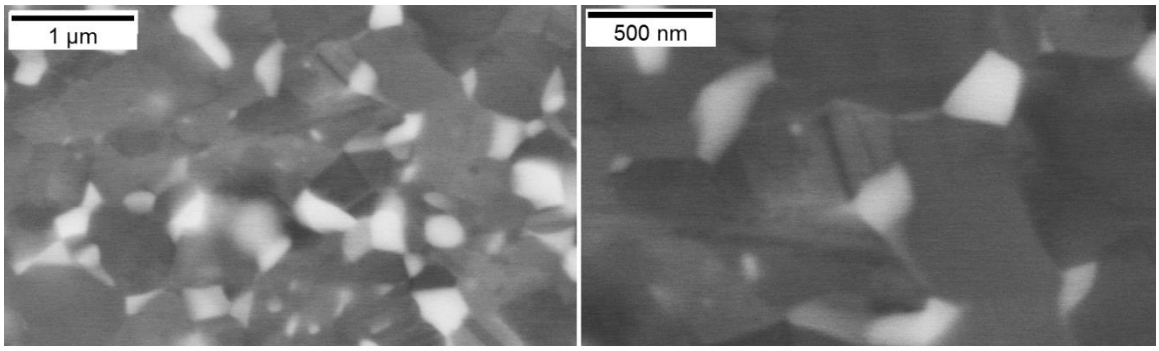

Figure 6-6: Electron channeling contrast revealing ultrafine γ + σ microstructure with equiaxed γ-phase morphology. (Courtesy of author)

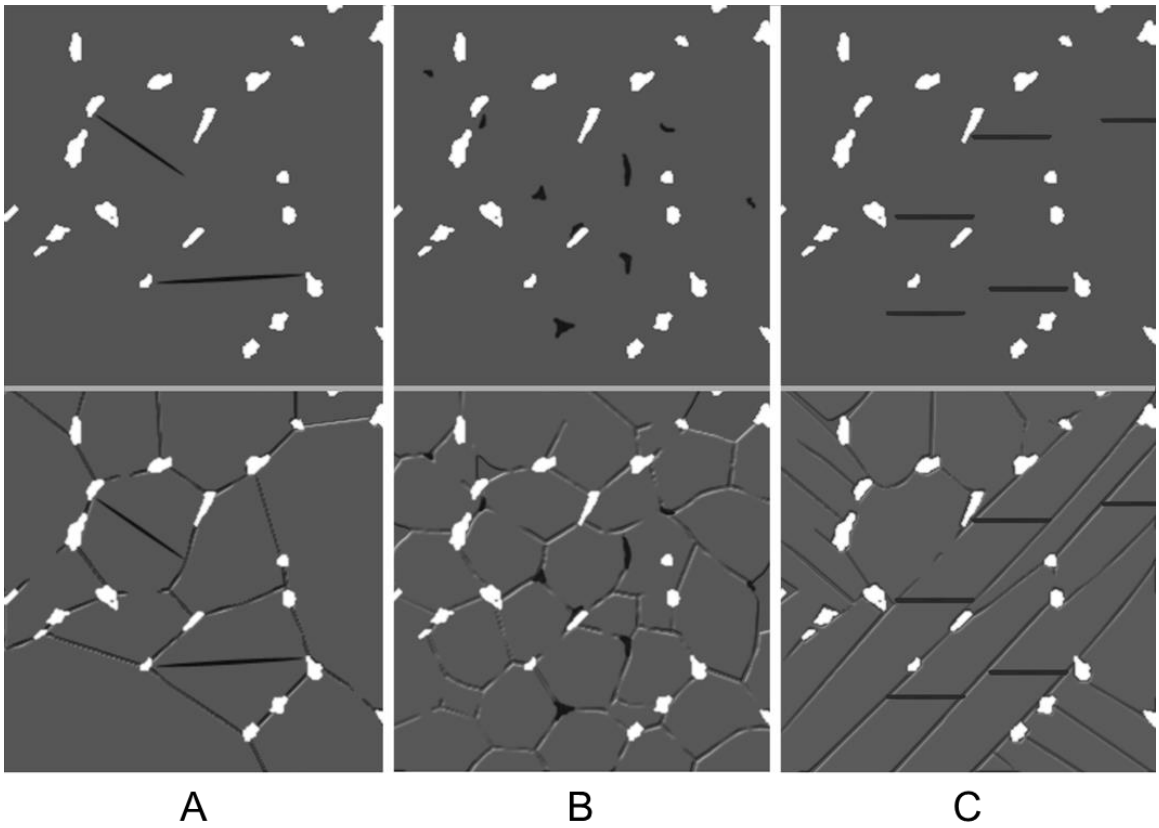

Figure 6-7: Schematic relationship between observed microcracking with respect to γ-grain morphology. A) equiaxed, B) ultrafine equiaxed, C) lath γ-grain morphology [82]. (Courtesy of author)

Under specific beam conditions, the γ-phase morphology is visible through electron channeling contrast, as seen in Figure 6-6, and when imaged in SE or BSE modes. However, the γ-phase morphology is not readily apparent in all micrographs of these alloys, so the particular cracking behavior in the microstructure can be used as evidence to discern the relationship of γ-phase morphology to deformation and failure mechanisms. Figure 6-7 schematically details the types of microcracking that may be observed and how they correlate with γ-phase morphology and damage. If the majority of cracks are large and span the length between σ-phase particles, it could indicate that there is a larger, equiaxed γ-phase (a). If there are short, randomly oriented cracks as well as cracks that form an angle or triple point, this could indicate finer equiaxed γ-phase grains (b). If there are a series of parallel cracks, then this could indicate acicular γ-phase morphology (c) which could locally share a common orientation relationship, due to the nature of their growth from the metastable β-phase [10, 23].

In samples of 15 at% Nb tested at 800°C, SEM evaluation shows microcracking solely in the γ-phase comprised mostly of short cracks that do not span the entire distance between σ-phase particles, as well as cracks opening up at characteristic triple points, which suggests a fine equiaxed morphology of γ-grains pinned by σ-particles as presented schematically in Figure 6-7(b). This microcracking pattern also indicates strain localization in the γ-phase and that γ/γ interfacial sliding may be the main deformation mechanism active at 800°C. This is consistent with the γ-grain morphology visible in SEM via channeling contrast.

In compressive fracture of a brittle material, microcracks will align with the direction of maximum compressive load, which for single-phase samples is the loading

axis [87]. It can be seen in Figures 6-4 and 6-5 (in which the loading direction is vertical with respect to the micrographs) that this is not the case for deformation of this two-phase material, but instead there is uniform microcracking throughout the microstructure. Additionally, flow curves indicate pseudo-plastic behavior. In ceramics or intermetallics, such uniform cracking is usually only seen when there is sufficient confining stress to prevent axial splitting or shear failure [87-89].

Since this alloy was tested only in uniaxial compression with no external confining stress, this behavior may be attributed to the re-distribution of stresses due to the reinforcement phase, as well as the small grain size [19, 86]. In this two-phase microstructure, confinement stress is provided locally by the hard reinforcement phase, which imposes a triaxial stress state due to strain compatibility constraint of the γ/σ interface [16, 86]. This also changes the stress state such that the loading direction is not necessarily that of maximum compressive stress, therefore modifying the orientation of microcracks relative to the sample geometry and loading.

No fragmentation or cracking through the σ-phase was present in this alloy, in contrast with the damage observed in studies of γ + σ microstructure with higher V_f σ-phase [1]. As expected, a continuous ultrafine γ-TiAl matrix with disconnected σ-Nb_2Al results in increased ductility [16]. This is evidenced by the high amount of compressive strain, more than 40% strain at 800°C, accommodated by the material with no evidence of large-scale cracking.

In samples of 15 at% Nb alloy tested at 700°C, there is not a clear indication of the γ-phase morphology based solely on microcracking, as they do not appear to predominantly open up at γ/γ or γ/σ interfaces. The majority of cracking is branching

within the γ-phase and is more severe in coarser regions of the microstructure, consistent with localization of strain in the γ-phase also seen at 800°C, as illustrated in Figure 6-8. However, there is still significant strain accommodation in these alloys at 700°C, as these compression tests were also interrupted at approximately 40% engineering strain. By contrast, alloys with a connected σ-phase matrix show very poor ductility, even at elevated temperatures, suffering brittle failure in compression testing at 700°C [1].

6.3.1 Effect of Microstructure Scale

Since the refinement of microstructure scale is expected to affect mechanical behavior in these alloys, the effect of modifying microstructure scale on deformation and failure behavior was studied. In order to determine the effect of microstructure scale, samples were heat treated to produce a coarser γ + σ microstructure, as detailed in the section 5.2.2. Alloy samples were also cut from solution treated and aged slices of the alloy such that prior β-phase grain boundaries were not included in the samples. In this way, samples were produced that have uniform microstructure throughout. These samples will be considered “single crystal” in that they originate from a single β-phase crystal, removing any effects the prior grain boundaries have on microstructure scale and strain localization. Compression testing of single crystal samples of fine and coarse microstructures were tested and compared with the flow behavior of “polycrystalline” samples reported in Section 6.1.

As illustrated in Figure 6-8, both fine microstructures have similar scale and morphology, while the coarse microstructure contains lath-shaped γ-phase morphology and less dispersed σ-phase. It can also be seen that the coarseness of the

microstructure or presence of prior β-grain boundaries does not have a strong effect on yield strength, but does affect flow softening behavior. Single crystal samples have less flow softening than the polycrystalline sample, which can be attributed to their lack of heavy localized deformation near prior β-grain boundaries. In polycrystalline samples, there is localization of strain near these boundaries due to inhomogeneous microstructure scale, which facilitates the nucleation of recovery and recrystallization.

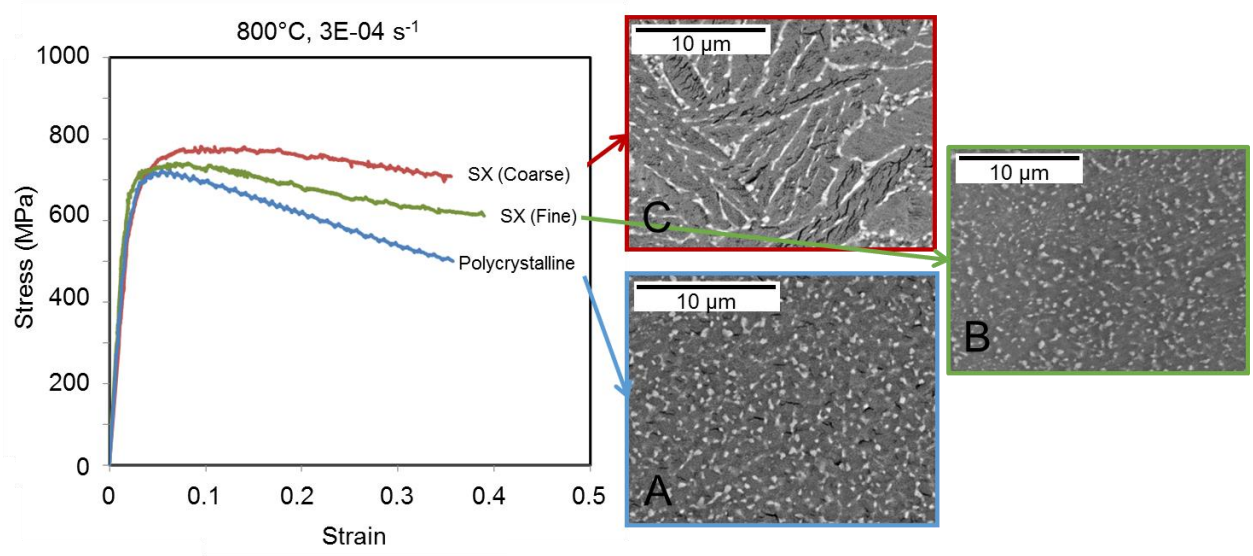

Figure 6-8: Comparison of flow curves of 15 at% Nb alloy with varying microstructure. Samples prepared to produce A) ultrafine equiaxed polycrystalline microstructure, B) ultrafine equiaxed single crystal microstructure, or C) coarse single crystal microstructure with enlarged lath-shaped γ-grain morphology. (Courtesy of author)

Since deformation is more homogeneously distributed in the single crystal samples, higher levels of strain are required to initiate recovery mechanisms. It is also seen that the coarse microstructure has less flow softening than the fine single crystal sample, which can be attributed to the relative increase in γ-phase size. Larger γ-phase increases the distance that dislocations must travel before annihilating at a grain boundary, and increases difficulty of γ/γ grain boundary sliding when compared with

finer γ-phase. With comparable strength and reduction in flow softening, a coarser microstructure may make it a better candidate for high temperature deformation resistance.

6.4 Tensile Testing

Compression testing indicates that an ultrafine microstructure with disconnected σ-phase yields a balance of strength and strain accommodation at high temperature. However, the tensile behavior of these alloys has not been previously studied. One reason that tensile testing has been a challenge is alloy fabrication and heat treatment. Due to the severe nature of the thermal treatment these alloys must undergo in order to produce a γ + σ microstructure with controllable scale, the samples cannot be machined into final geometry until heat treatment is completed. Initial attempts at tensile sample fabrication proved that heat treatment of dogbone specimen causes high thermal stresses during quenching, and high residual stresses afterwards. Due to this, if cracking does not occur upon quenching, the dogbone is highly susceptible to cracking upon further handling, usually initiating at the fillet. Similarly, heat treatment of large plates is difficult due to the large thermal gradients experienced during quenching. Under both of these conditions, significant sample cracking occurred during quench, making them unsuitable for further processing. It was found that the most reliable method for sample heat treatment and machining is to section the alloy to rectangular samples near the final dimensions of the dogbone, solution treat, age, and then machine the final geometry. In this way, the alloy samples are sufficiently small so that even heat removal can occur during quenching, and the simple geometry removes any stress concentration that would otherwise occur at the fillet.

Initial tensile testing of these samples at elevated temperature resulted in premature cracking and failure in the fillet region of the dogbone. In a sample of 15 at% Nb alloy tested at 800°C, 10^{-4} s^{-1}, it was found that this failure was the result of highly localized strain due to the collar-style grips used. This stress concentrator induced a high amount of deformation, initiating cracking through the sample as illustrated in Figure 6-9. The majority of deformation occurred within the grip region, plastically deforming the sample to the inner contour of the collar grips. Since deformation occurred outside of the gage section, meaningful flow data was not able to be obtained. Analysis of a second tensile test under the same conditions resulted in failure near the fillet region as well. SEM analysis of this sample, presented in Figure 6-10, found this failure to be due to a Nb-rich inclusion near the fillet region. Due to the high amount of local stress placed on the dogbone sample by collar-style grips, it was determined that additional testing should be conducted using more traditional grips that would distribute the load more evenly on the grip section of the samples.

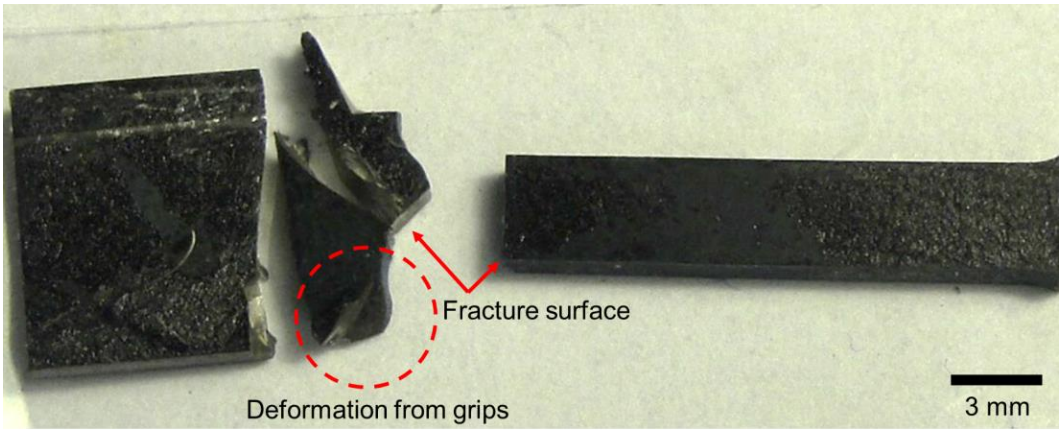

Figure 6-9: Tensile sample of 15 at% Nb alloy tested at 800°C, 10^{-4} s^{-1} showing high amount of local plastic deformation; brittle tensile fracture. Note: additional cracking within grip region occurred during sample removal from grips. (Courtesy of author)

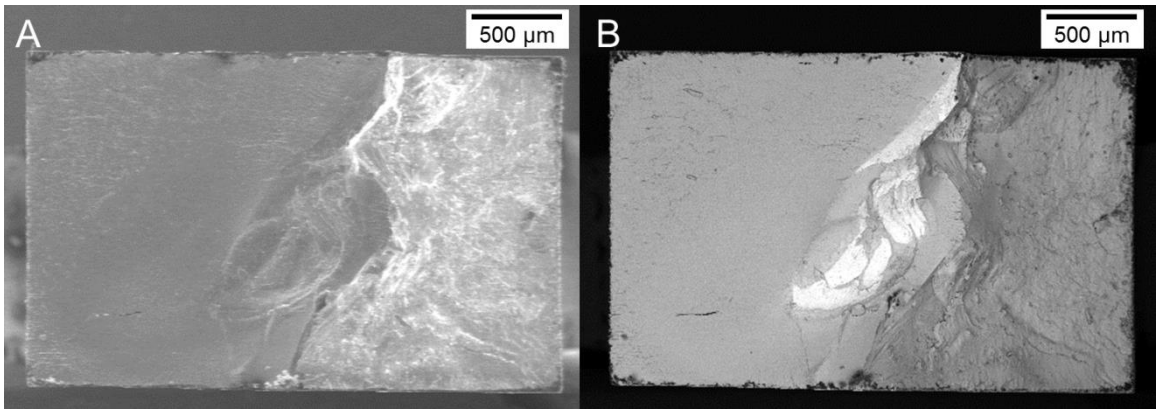

Figure 6-10: SEM of fracture surface of tensile dogbone tested at 800°C, 10^{-4} s^{-1} showing fracture initiation in high-atomic weight inclusion. A) Secondary electron mode; B) backscatter mode. (Courtesy of author)

Further tensile testing was conducted on dogbone samples at room temperature, and these samples also fractured near the fillet region before any plastic deformation occurred. Observation of the fracture surface using optical and electron microscopy (Figure 6-11) indicate a mixed-mode fracture that appears macroscopically brittle and microscopically ductile. Crack initiation begins on the sample face and appears to follow a few cracking paths, giving the fracture surface a faceted appearance. This could be explained by fracture along previous β-phase grain boundaries that would provide an easy cracking path. However, since the microstructure is fully transformed to very fine γ + σ, there is no immediately distinct pattern of the fracture surface on a macroscopic scale.

Closer examination of the fracture surface (Figure 6-12) does not reflect classical intergranular fracture, microvoid coalescence, or cleavage failure modes. Instead, it has characteristics of a combination of a tearing topography surface fracture and quasi-cleavage fracture [19, 21, 90] which is indicative of some plasticity in the γ-phase during fracture despite the apparent brittle fracture

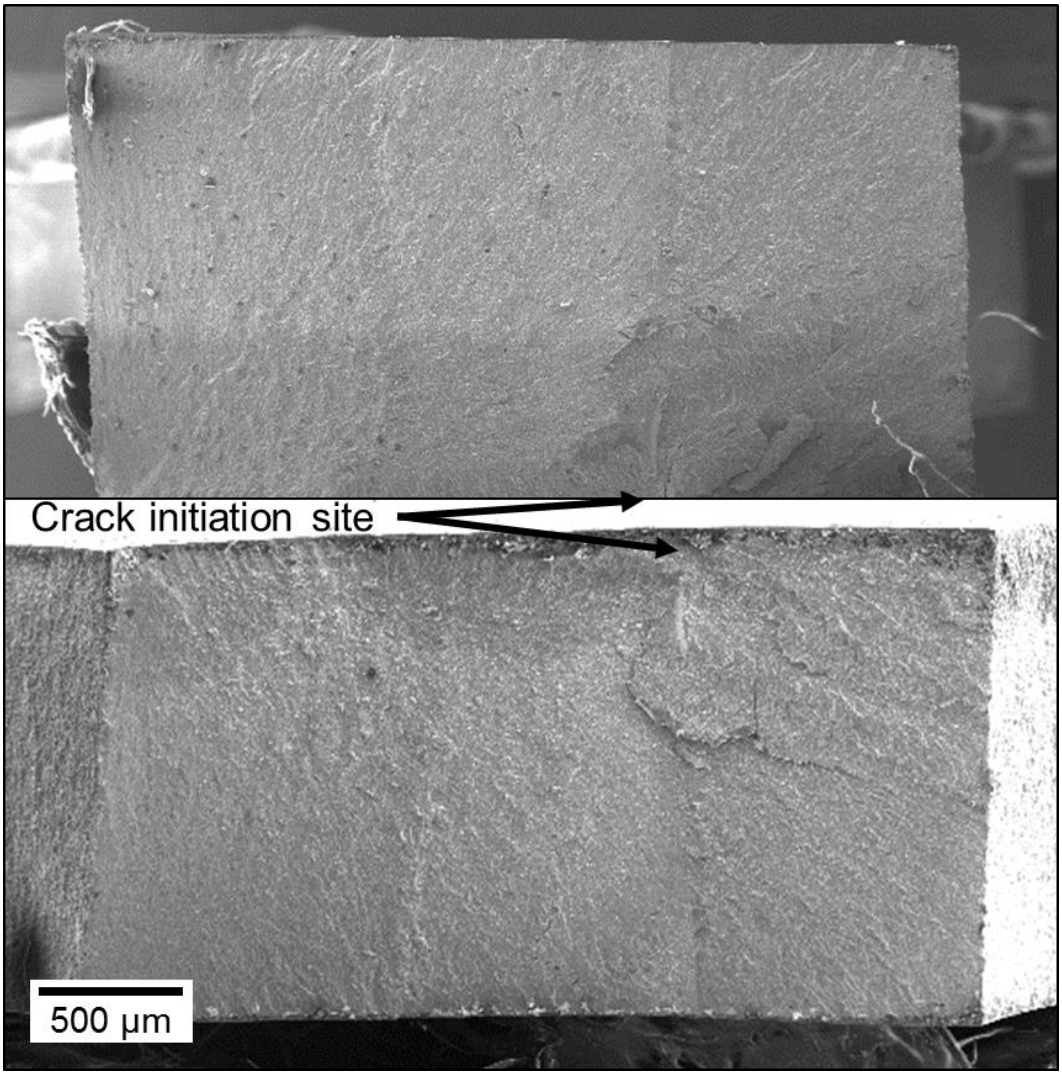

Figure 6-11: SEM of fracture surface of tensile dogbone tested at room temperature and 10^{-4} s^{-1} showing facing sides of fracture surface. Fracture initiates on sample face, and follows faceted path. (Courtesy of author)

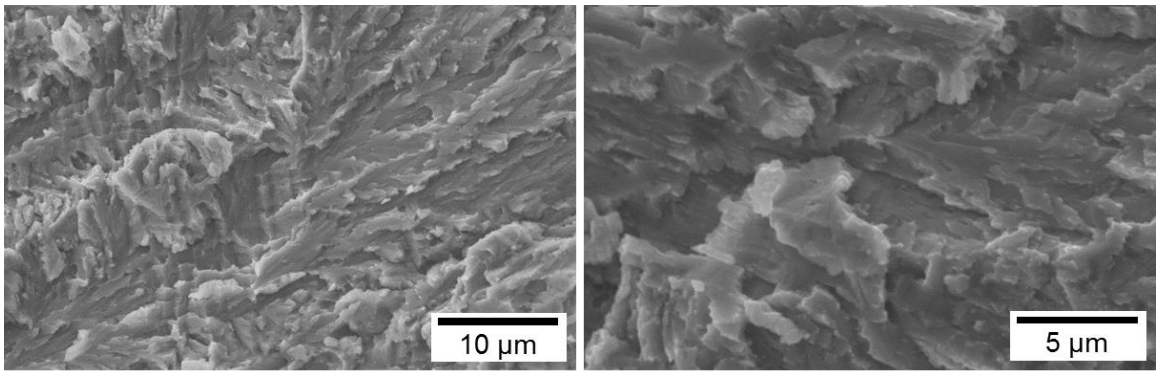

Figure 6-12: SEM micrograph illustrating topography of γ-phase fracture, indicative of mixed transgranular and intergranular modes. (Courtesy of author).

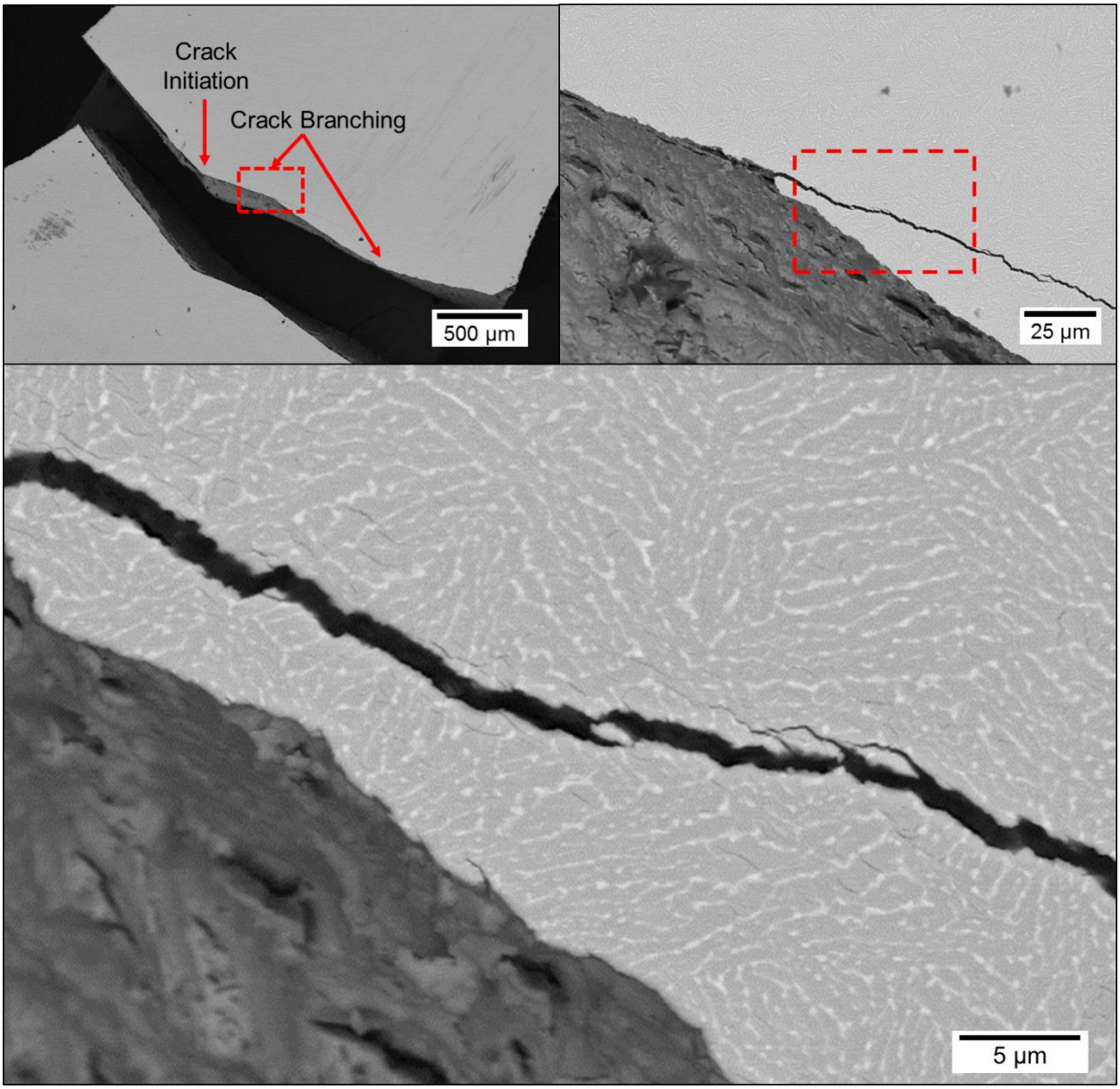

Figure 6-13: SEM micrograph of tensile sample face, showing crack branching near fracture surface, following path through coarse γ-phase. (Courtesy of author).

Figure 6-13 shows the macroscopic crack path through the tensile sample, as well as some crack branching that occurred during deformation. The crack appears to follow a preferred plane, which is a probable prior β-phase grain boundary, and continues to follow this path while the fracture surface deviates. This major crack branching appears independent of local γ-phase orientation and morphology, as does

microcracking near the fracture surface. Further analysis of cracking near the fracture surface and approximately 100 μm away from the fracture shows that cracking occurs similarly, and only in the γ-phase.

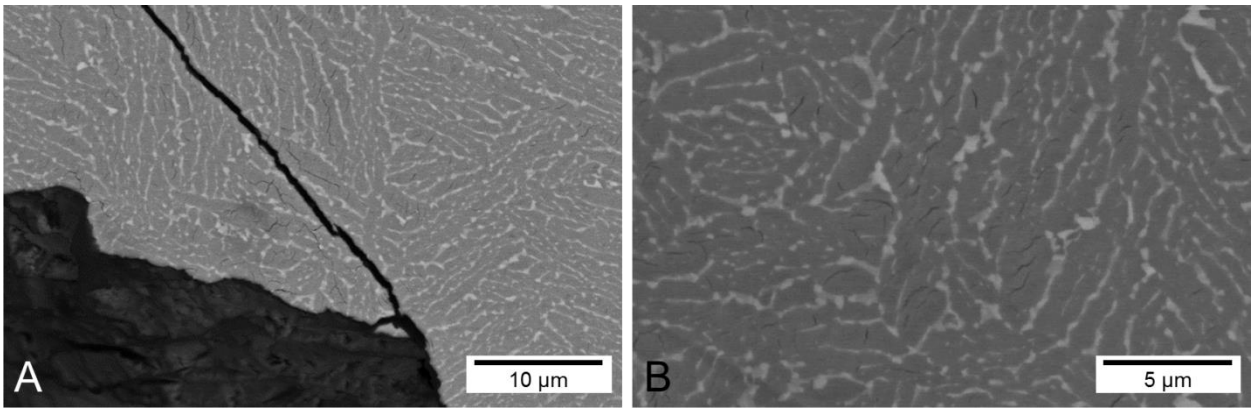

Figure 6-14: Detail of tensile sample face, illustrating microcracking solely through coarse γ-phase as well as lack of γ/σ interfacial or σ-phase fracture. A) Near fracture surface; B) away from fracture surface, (Courtesy of author)

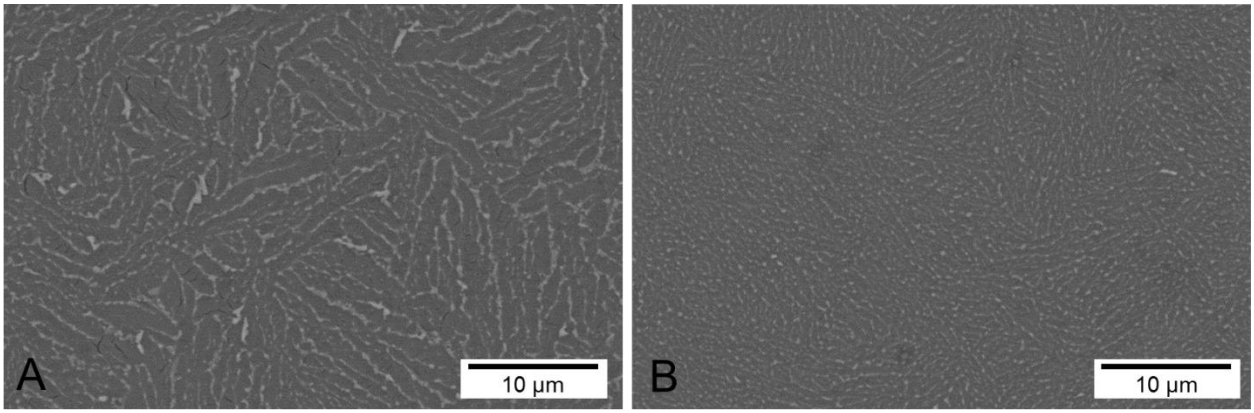

Figure 6-15: Comparison of γ + σ microstructure scale and morphology A) near failure site (100-200μm) and B) far from failure site (1-2 mm). (Courtesy of author)

Additionally, increased microcracking is most evident in coarser regions of γ-phase while local finer regions do not experience the same level of cracking, as illustrated in Figure 6-14. Comparison of microstructure scale near to the fracture surface (100-200 μm) to the scale far from the failure site (1-2 mm) reveals a large difference in microstructure scale (Figure 6-15). This confirms that fracture occurred

near a prior β-phase grain boundary, since it has been demonstrated that coarser microstructure is present near these boundaries due to γ-phase nucleation upon quenching.

CHAPTER 7
SUMMARY AND CONCLUSIONS

Through thermal analysis, heat treatment, and microstructural evaluation was conducted on alloys in the Ti-Al-Nb-Cr-Mo system with high Nb concentration (15-25 at%). Alloys of composition Ti-45Al-xNb-5Cr-1Mo (where x = 15, 20, 25 at%) were prepared via arc melting, solution treated, water quenched, and aged to produce γ + σ microstructure. Alloys with 15, 20, and 25 at% Nb were solution treated at 1400, 1450, and 1500°C, and aged at 1000, 950, and 1125°C, respectively. This evaluation has found that increasing Nb content has several effects on phase transformation and microstructure development.

Primarily, increasing Nb increases phase transformation temperatures for equilibrium phase transformations, suppresses metastable ($\beta \rightarrow \gamma + \sigma$) transformation temperatures, increases amount of γ-TiAl formed upon quenching, as Nb stabilizes all phases to higher temperature, and increases phase fraction of Nb-rich σ-phase. Ultrafine, relatively equiaxed microstructure was successfully produced in 15 and 20 at.% Nb alloys, but it has been observed that with an increase to 25 at.%, aged microstructures transition to a coarser microstructure with more connected σ-phase. It has also been demonstrated that microstructural development in these alloys is very sensitive to composition and processing parameters, such as heating and cooling rates. Cooling rate after solution treatment, as well as transformation to γ-TiAl is vital to the modification of γ + σ microstructure in these alloys. Towards the goal of designing a high-Nb titanium aluminide with ultrafine, disconnected γ + σ morphology, it has been established that microstructural control can be accomplished in alloys containing 15 - 25 at.% Nb through targeted chemistry and processing controls.

Elevated temperature compression testing was conducted on alloys with 15, 20, and 25 at% Nb that were heat treated to form a γ + σ microstructure. Ti-45Al-15Nb-5Cr-1Mo at 700 and 800°C shows good high temperature strength and large compressive strain (40%) without sustaining macroscopic fracture. Strain rate sensitivity and analysis of the flow curves indicate that γ/γ interfacial sliding and dynamic recrystallization of the γ-phase are the predominant deformation mechanisms at 800°C, especially at slower strain rates. Microstructural analysis of deformed samples supports γ/γ interfacial sliding, with microcracks opening primarily at γ/γ grain boundaries and no cracking of the σ-phase. At 700°C, localization of strain within the γ phase is apparent and higher strength and work hardening rates may be attributed to the lack of recrystallization behavior in this temperature regime. The impact of dynamic recrystallization behavior at lower strain rates warrants further study in order to determine this material's potential for high temperature applications.

It was found that increased Nb content produces alloys with higher strength at high temperature, resulting from increased σ-phase present in the microstructure. Accompanying the increase in strength was a decrease in compressive strain to failure, especially at 700°C and highest strain rates. All samples strained significantly past yielding exhibited flow softening behavior, which can be attributed to dynamic recovery and recrystallization mechanisms. Deformation of the 25 at.% Nb alloy resulted in a decrease in strength between 800°C and 900°C that was much larger than the lower Nb alloys. This is due to the increased σ-phase content and connectivity, which undergoes a softening transition around 900°C, indicating that the high temperature deformation

behavior of this alloy is more dependent on σ-phase properties than that of alloys with a finer, more disconnected precipitate.

From the standpoint of microstructure development and mechanical behavior at elevated temperature, the 20 at% Nb alloy produces both optimal microstructure and properties for the goals of this work. A fine, disconnected σ-phase morphology was produced through heat treatment, and high temperature yield strengths of approximately 600-1000 MPa were achieved when tested at strain rates of 10^{-4} to 10^{-2} s^{-1}. This combination of strength with desired microstructure makes this alloy the best of the three studied in this work, though further characterization and alloy development is required in order to fully determine if this alloy is most suitable for mechanical applications.

One important finding from tensile testing is that cracking and failure is controlled by the γ-phase in this coarse alloy microstructure, rather than the more connected σ-phase as previously thought. Since σ-phase volume fraction is not high enough for it to form a fully contiguous matrix, the deformation is controlled by the γ-phase, which accommodates strain such that stresses are never high enough to fracture σ-phase precipitates before crack propagation occurs through γ-phase.

Tensile testing shows that while coarser γ-phase is potentially beneficial to high temperature deformation resistance, it is not sufficiently ductilized by σ-phase dispersion to redistribute stresses and prevent the formation of microcracks. In order to circumvent the negative effects of coarse γ-phase on fracture in these alloys, it is desirable to produce a single-crystal sample of β-phase before aging the alloy to produce the γ + σ microstructure. In this way, a uniformly fine microstructure can be

formed without coarse γ-phase local to the previous β-grains that would serve to initiate crack propagation through the alloy.

CHAPTER 8
FUTURE WORK

At this stage in the research into high-Nb containing Ti-Al-Nb based alloys, investigations have encompassed computational and experimental thermodynamic assessment, study of nucleation sequences, phase equilibria, and phase reactions, as well as room temperature compression, elevated temperature compression, and initial exploration into fracture toughness and tensile properties at room temperature [1, 10, 14-16, 23, 33, 38-40, 42, 65, 66, 69, 70, 82]. The present work explores the microstructure development and mechanical properties of alloys with varying Nb concentration as a first step towards a more full scientific understanding of alloys in this system, and there is ample opportunity for further study.

As a direct continuation of this work, there are several avenues that can be explored. The first of these is the improvement in room and high temperature mechanical behavior, namely in tension. This work showed that refinement of the microstructure is very important for improvement in mechanical properties and that prior β-grains are a weak point in tension due to localized strain and opening of cracks. Future work could be completed to overcome this challenge in a few ways.

Study of alloying additions for grain boundary engineering would offer the benefit of strengthened β-grain boundaries. If the chemistry of alloys in this system can be altered such that there is reduced strain between adjacent β-grains, this could improve tensile behavior. This could be accomplished by beginning with first principles calculations [91, 92], and can be experimentally verified by measuring the relative amounts of texturing in the β-grains after

solution treatment and quench via electron backscatter diffraction (EBSD) mapping. The texturing of each alloy can be related to the strength of the material in tension, but in order for this to be an appropriate measure, grain size must be controlled for (both of β-grains and the aged γ+σ microstructure), as well as σ-phase content and morphology. Alternatively if alloying additions can be found that completely inhibit the formation of γ-phase at the β-grain boundaries upon quenching, resulting in a uniformly ultrafine microstructure, this would serve to reduce the amount of strain localization and cracking in the γ-phase that ultimately led to failure in this study.

Another approach is the fabrication of single-crystal β-phase samples that can then be heat treated to produce the γ + σ microstructure. The presence of β-grain boundaries in these alloys provides a location for heterogeneous nucleation of γ + σ microstructure, especially γ-phase upon quenching. The driving force for nucleation of γ + σ microstructure from the β-phase calculated in Chapter 4 only reflects homogeneous nucleation, but in the experimental alloys it was seen that heterogeneous nucleation and growth of the γ-phase was comparatively easier, leading to a coarse γ-phase near the prior β-grain. Due to their lack of β-grain boundaries, and therefore lack of coarse γ-phase grains, single crystal samples did not experience strain localization. A uniformly fine microstructure would be able to accommodate more strain before failure through the distribution of strain and the presence of σ-phase to reduce crack length and alter the local stress state in the surrounding γ-phase.

Another option would be to explore chemistry, thermo-mechanical processing, or other routes to refine the β-grain size. If β-phase grains can be

refined to a significant extent there would be less strain incompatibility between them, and if they are sufficiently small could even limit the γ + σ microstructure scale. In the current alloys, the β-phase grain size is on the order of 1-3 mm, which is comparable to the tensile sample gage section size. If instead the β-phase grains could be refined to 10-100 μm, tensile testing of similar sample size would represent polycrystalline behavior rather than the bond strength of one to a few β-grain boundaries. Additionally, the refinement of the β-grain size may make the prevention of γ-phase nucleation upon quenching unnecessary if thermal processing can be determined to nucleate and grow the σ-phase homogenously from γ-phase, such as very long-term aging.

In addition to characterization and improvement of tensile properties, it would be of interest to investigate fatigue behavior in these alloys, as well as the relative fracture toughness of the various γ + σ microstructure scales and morphologies that can be produced. The investigation into fracture toughness and fatigue would allow for the determination of whether crack nucleation or propagation is most important in tensile failure of these alloys. In order for toughness to be appropriately tested, samples must be made according to ASTM standard E1820, and it should be noted that indentation methods are not suitable to calculate fracture toughness of these alloys due to the presence of the connected γ-phase matrix, which is too ductile to produce accurate readings by this method.

Finally, if these alloys are intended for use in high temperature applications, it would be relevant to investigate their creep behavior. Previous research has studied creep of γ + σ alloys with high σ-phase content [1, 12], so it

would be appropriate to characterize the creep behavior of low σ-content alloys to see if creep behavior is dependent on the σ-phase as previously established [1, 12] , or more directly related to the γ-phase content and contiguity, as is the compressive and tensile deformation.

In order to further explore deformation mechanisms in these alloys, transmission electron microscopy (TEM) could be conducted in order to gain insight into dislocation structures and interfaces. The first aspects of interest would be the character of the γ/σ interface. This could be done by using focused ion beam (FIB) milling in order to extract samples that contain this interface. TEM analysis of the interface could then be conducted to analyze for coherency, and would add to the understanding of how σ-phase precipitates behave with respect to dislocation mechanics in the γ-phase matrix, and if coherency changes through the course of long-term aging.

Also of great interest would be TEM analysis of interrupted high temperature testing. This would be done with the goal of determining if dislocation recovery mechanisms such as dynamic recrystallization are occurring. Evidence may include the presence of recrystallized, dislocation-free grains and the overall decrease in dislocation density of samples interrupted near the trough of recrystallization oscillations versus those interrupted near the peaks. In order to accomplish such characterization, a high temperature mechanical testing system must be set up which has capability for quenching directly from the hot test stage. Ideally, the testing would still be conducted under vacuum in order to minimize the effect of surface oxidation of alloy properties. Alternatively, in-situ TEM mechanical testing could be used to

determine the dislocation behavior in very small samples. However, this may not be representative of overall alloy characteristics since the scale of the microstructure is not nanoscale, the stress states of the TEM foil would necessarily be different than those of bulk alloy samples.

Another approach to studying dynamic recrystallization behavior in these alloys would be to conduct in-situ high temperature mechanical testing while performing neutron scattering. This could be accomplished using systems such as the VULCAN at Oak Ridge National Laboratory, in which the sample can be induction heated while loading and would also allow for in situ studies of texture changes, stress development, and damage [93].

APPENDIX A
CHEMICAL ANALYSIS OF ALLOYS

Table A-1: Summary of EMPA results of 15Nb alloy from Certificate of analysis; Sophisticated Alloys, Inc., nationally certified external laboratory.

Element	at%	at wt	wt/mol_{alloy}	wt%	ICP (wt%)	ICP (at%)
Ti	34	47.88	16.28	35.45	35.14	33.70
Al	45	26.98	12.14	26.44	26.67	45.39
Nb	15	92.90	13.93	30.35	30.13	14.89
Cr	5	51.99	2.59	5.66	5.87	5.18
Mo	1	95.94	0.96	2.09	2.19	1.05
Total	100	-	45.91	100	100	100.21

Table A-2: Summary of EMPA results of 20Nb alloy from Certificate of analysis; Sophisticated Alloys, Inc., nationally certified external laboratory.

Element	at%	at wt	wt/mol_{alloy}	wt%	ICP (wt%)	ICP (at%)
Ti	29	47.88	13.89	28.83	29.06	29.23
Al	45	26.98	12.14	25.21	25.38	45.31
Nb	20	92.90	18.58	38.58	37.88	19.64
Cr	5	51.99	2.59	5.40	5.50	5.10
Mo	1	95.94	0.96	1.99	2.18	1.09
Total	100	-	48.17	100	100	100.37

Table A-3: Summary of EMPA results of 25Nb alloy from Certificate of Analysis; Sophisticated Alloys, Inc., nationally certified external laboratory.

Element	at%	at wt	wt/mol_{alloy}	wt%	ICP (wt%)	ICP (at%)
Ti	24	47.88	11.49	22.79	22.70	23.90
Al	45	26.98	12.14	24.08	23.89	44.64
Nb	25	92.91	23.22	46.07	46.37	25.16
Cr	5	51.99	2.60	5.16	5.02	4.87
Mo	1	95.94	0.96	1.90	2.02	1.06
Total	100	-	50.41	100	100	99.64

APPENDIX B
THERMAL ANALYSIS (DSC)

Upon initial cycling of the as-cast or quenched alloys, there are some metastable phase transformations that occur. In the as-cast microstructure, there is some β-phase present in addition to the γ- and σ-phases that would be expected to form upon solidification. This results in non-equilibrium transformations that are seen in the first cycle, but disappear in subsequent thermal cycling. In the case of the 15 at% Nb alloy, this is manifested by a double endothermic peak in the dissolution of the γ- and σ-phase into the β-phase. Upon subsequent cycling, this peak turns into a single peak, indicating that the γ- and σ-phases that formed upon equilibrium cooling of the alloy begin to dissolve at the same temperature.

Similarly, there is a double peak upon heating of 25 at% Nb alloy near 800°C which corresponds to the nucleation of σ-phase, as seen in Figure 4-6. This double peak occurs only on the first cycle, indicating that it is the result of σ-phase nucleation from the non-equilibrium cast or quenched microstructure. As such, there is an extra dissolution peak corresponding to the dissolution of this non-equilibrium phase, seen a shoulder in the endothermic peak near 1350 °C. After cycling these alloys, the metastable phase transformations do not appear since the alloy has sufficient during cooling to transform to equilibrium γ- and σ-phases phases. Additionally, with thermal cycling of all of the alloys there is a suppression of any exothermic peaks occurring below about 1000°C. That is to say that the non-equilibrium nucleation of the γ- and σ-phases does not occur since the alloy is being heated from an equilibrium γ+σ microstructure in the second and third cycles, rather than one containing the metastable β-phase from with the two-phase microstructure can nucleate.

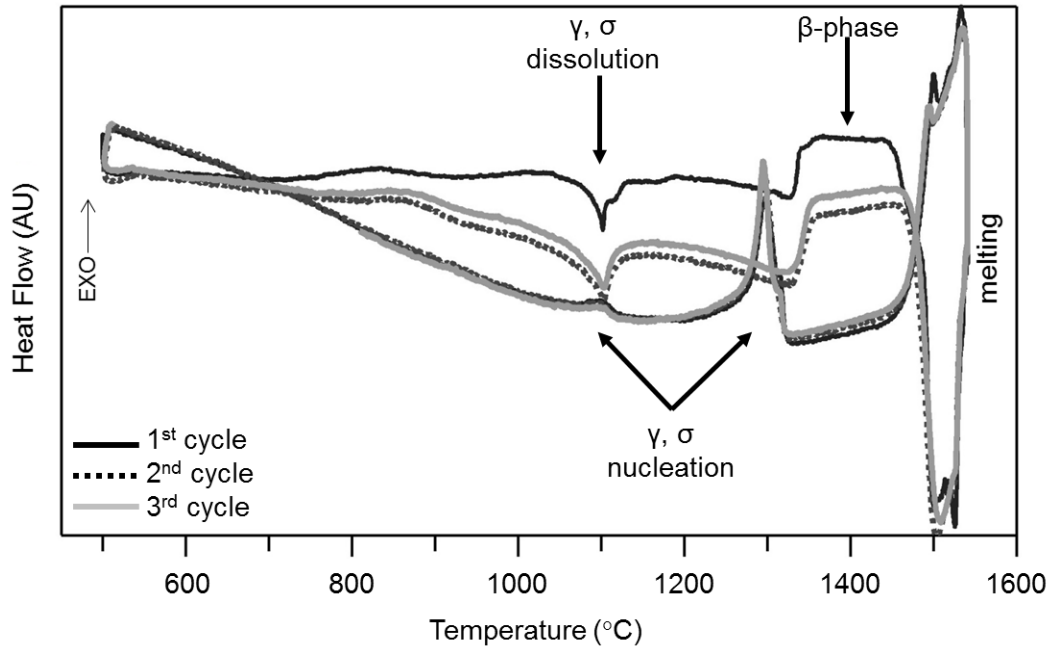

Figure B-1: DSC of as-cast 15Nb alloy, cycled three times. Note stability of transformation temperatures between cycles. Dark, solid curve indicates initial heating (top curve), melting and cooling, with subsequent cycles settling to similar heat flow levels after initial alloy melting and solidification

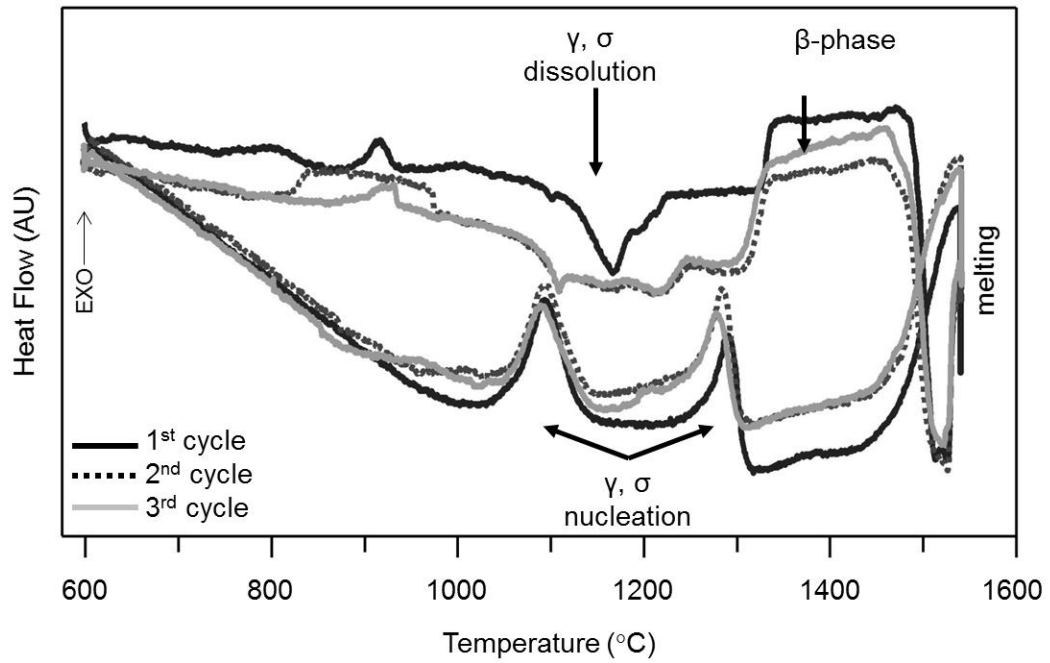

Figure B-2: DSC of as-cast 20Nb alloy, cycled three times. Note stability of transformation temperatures upon cooling, and change in nature of transformation upon heating with increasing cycles.

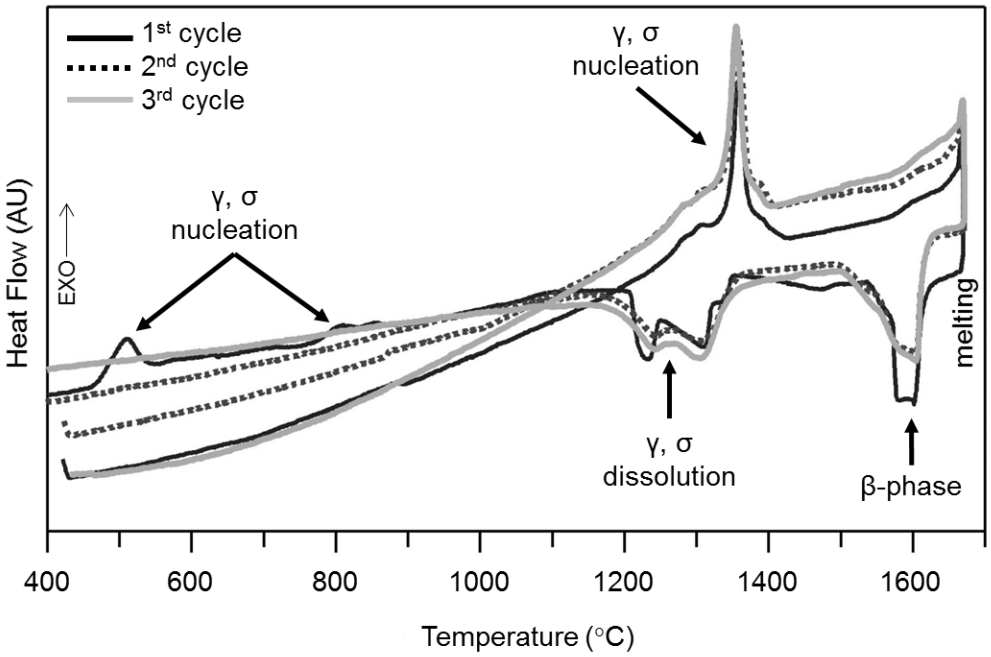

Figure B-3: DSC of as-cast 25Nb alloy, cycled three times. Note stability of transformation temperatures upon cooling and heating, with lack of low temperature peaks upon second and third heating.

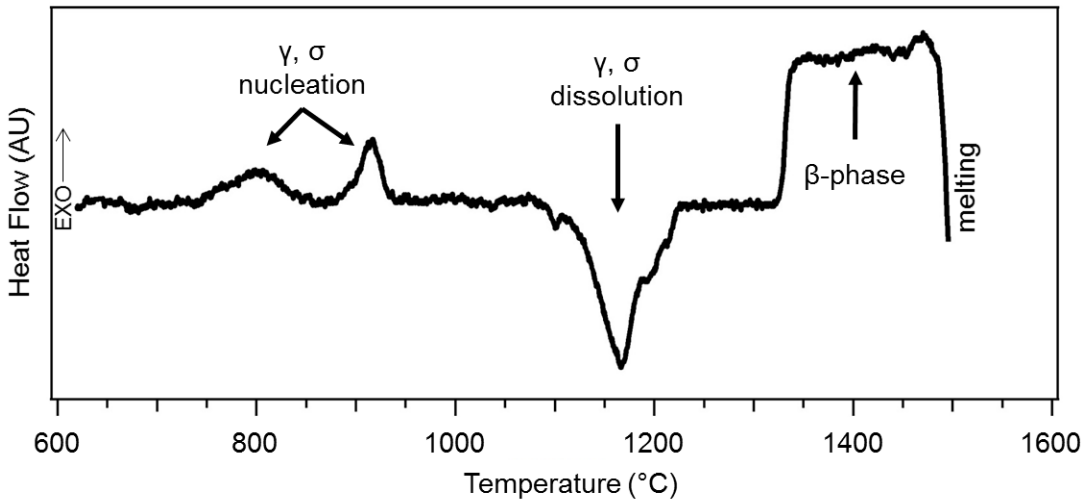

Figure B-4: DSC curve upon heating of solution treated and quenched 15Nb alloy

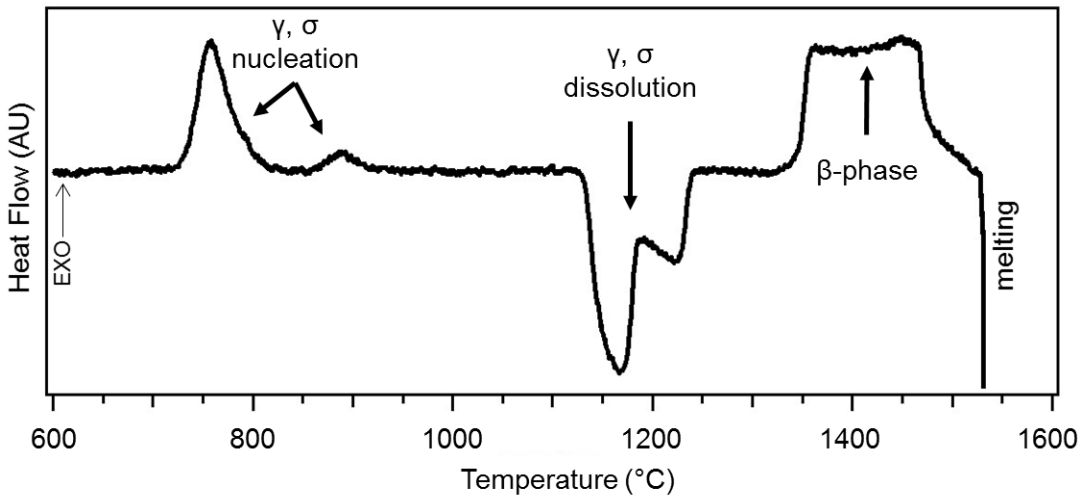

Figure B-5: DSC curve upon heating of solution treated and quenched 20Nb alloy

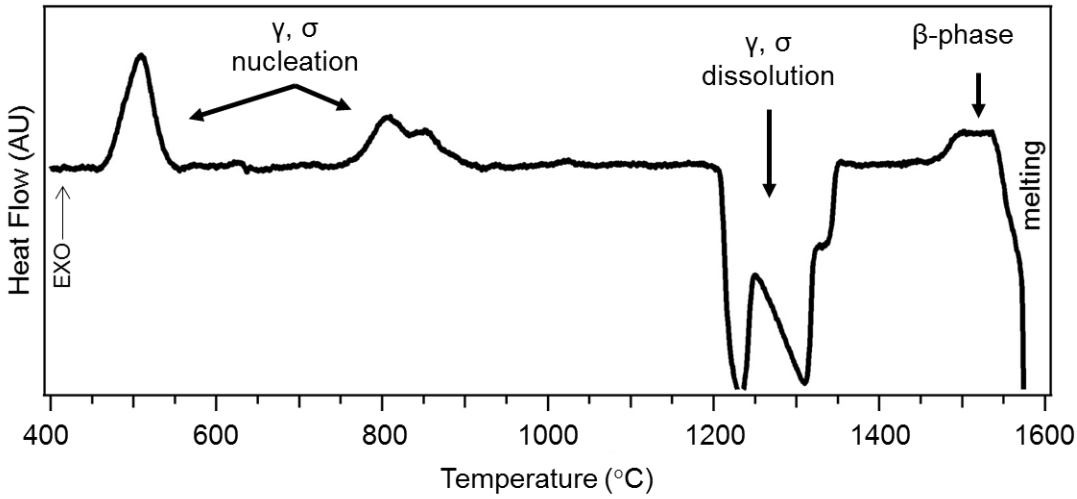

Figure B-6: DSC curve upon heating of solution treated and quenched 25Nb alloy

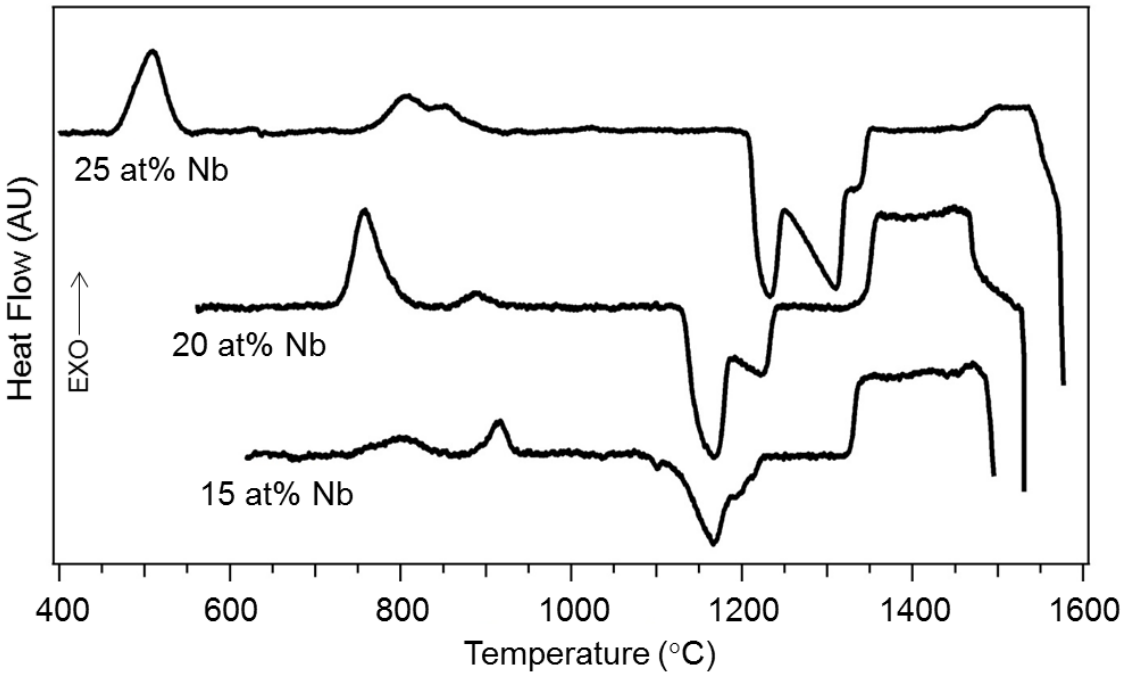

Figure B-7: Comparison of DSC curves produced upon initial heating of solution treated and quenched 15, 20, and 25 at% Nb alloys

APPENDIX C
MECHANICAL TESTING DATA

Ti – 45Al – 15Nb – 5Cr – 1Mo

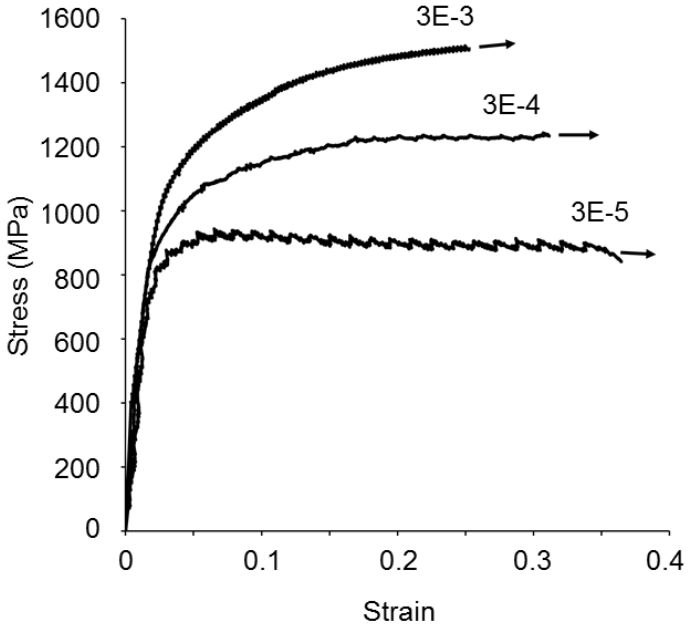

Figure C-1: Compression testing of Ti – 45Al – 15Nb – 5Cr – 1Mo alloy at 700°C

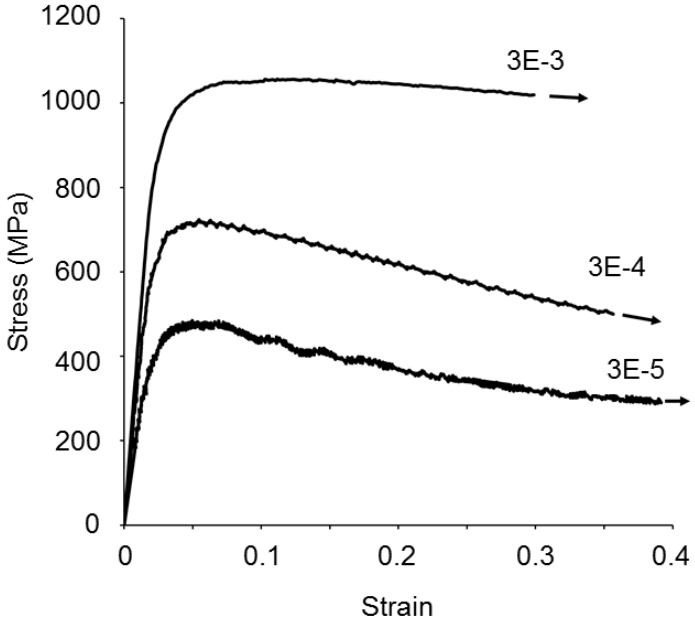

Figure C-2: Compression testing of Ti – 45Al – 15Nb – 5Cr – 1Mo alloy at 800°C

Ti – 45Al – 20Nb – 5Cr – 1Mo

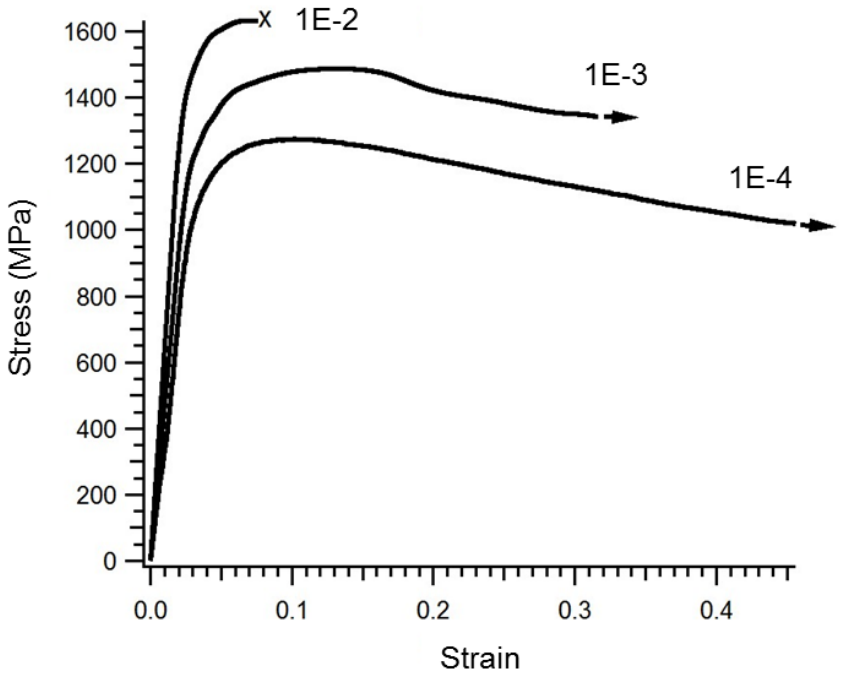

Figure C-3: Compression testing summary of Ti – 45Al – 20Nb – 5Cr – 1Mo alloy at 700°C at strain rates of 10^{-2}, 10^{-3}, and 10^{-4} s^{-1}

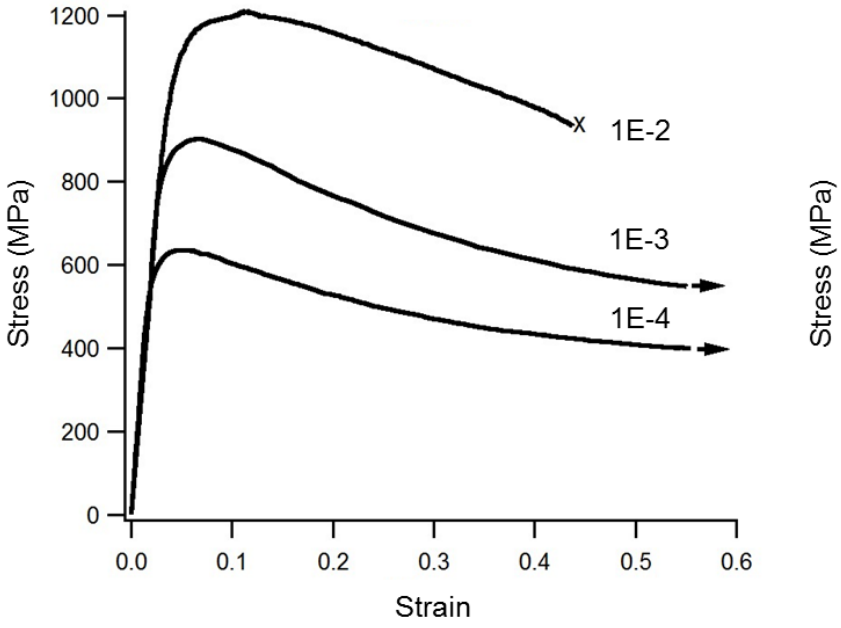

Figure C-4: Compression testing summary of Ti – 45Al – 20Nb – 5Cr – 1Mo alloy at 800°C at strain rates of 10^{-2}, 10^{-3}, and 10^{-4} s^{-1}

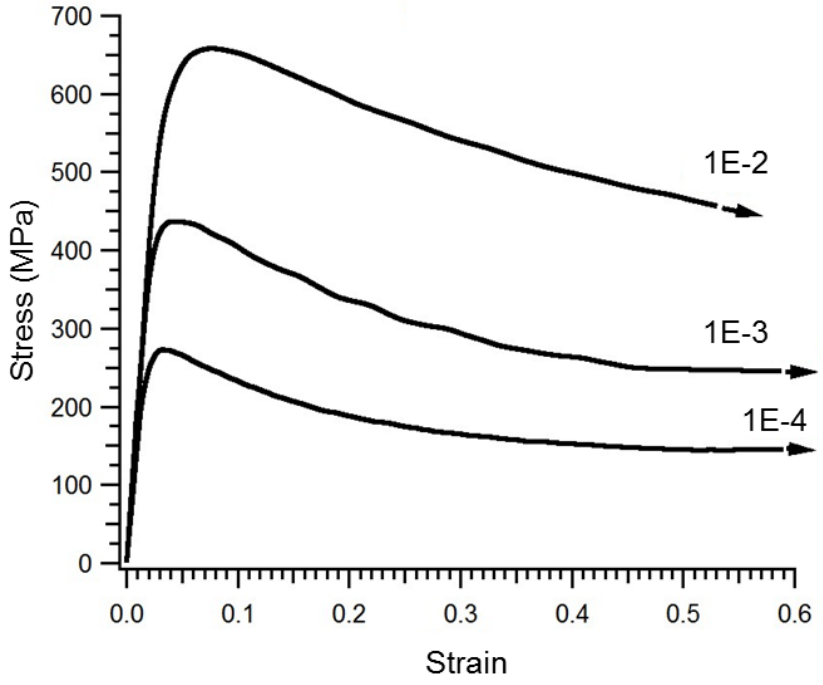

Figure C-5: Compression testing summary of Ti – 45Al – 20Nb – 5Cr – 1Mo alloy at 900°C at strain rates of 10^{-2}, 10^{-3}, and 10^{-4} s^{-1}

Ti – 45Al – 25Nb – 5Cr – 1Mo

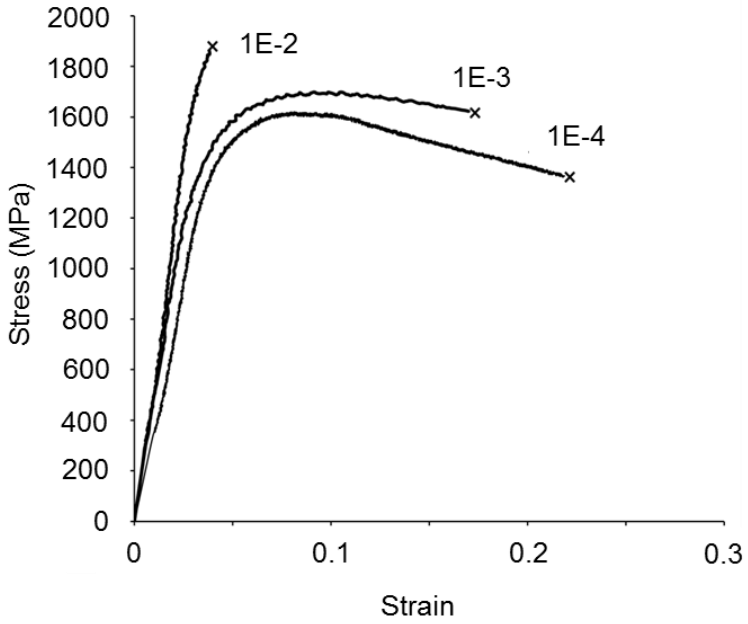

Figure C-6: Compression testing summary of Ti – 45Al – 25Nb – 5Cr – 1Mo alloy at 700°C at strain rates of 10^{-2}, 10^{-3}, and 10^{-4} s^{-1}

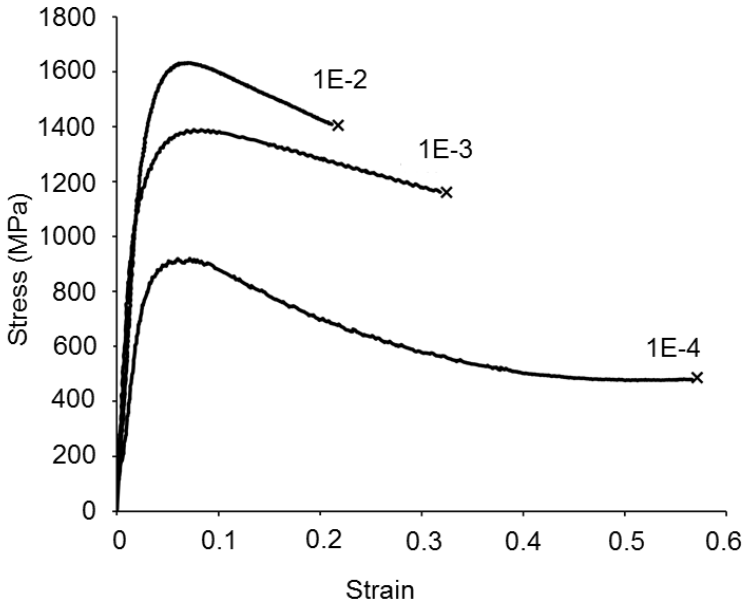

Figure C-7: Compression testing summary of Ti – 45Al – 25Nb – 5Cr – 1Mo alloy at 800°C at strain rates of 10^{-2}, 10^{-3}, and 10^{-4} s^{-1}

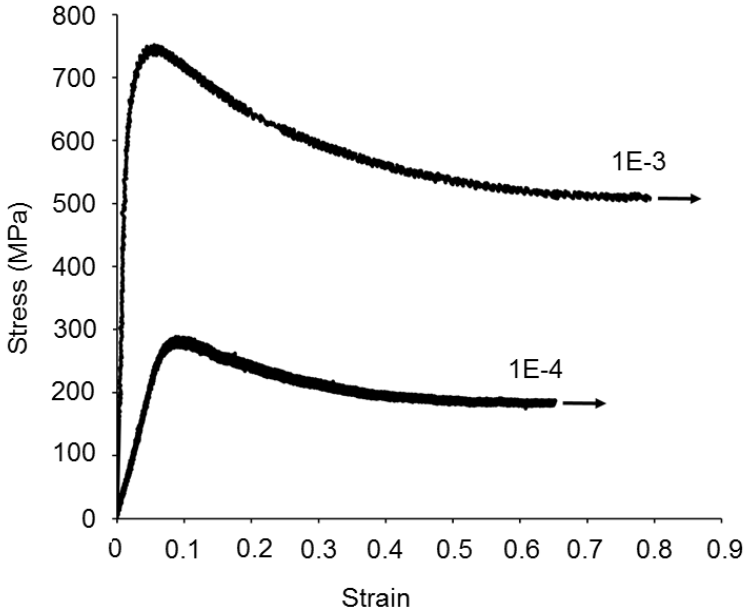

Figure C-8: Compression testing summary of Ti – 45Al – 25Nb – 5Cr – 1Mo alloy at 900°C at strain rates of 10^{-3}, and 10^{-4} s^{-1}

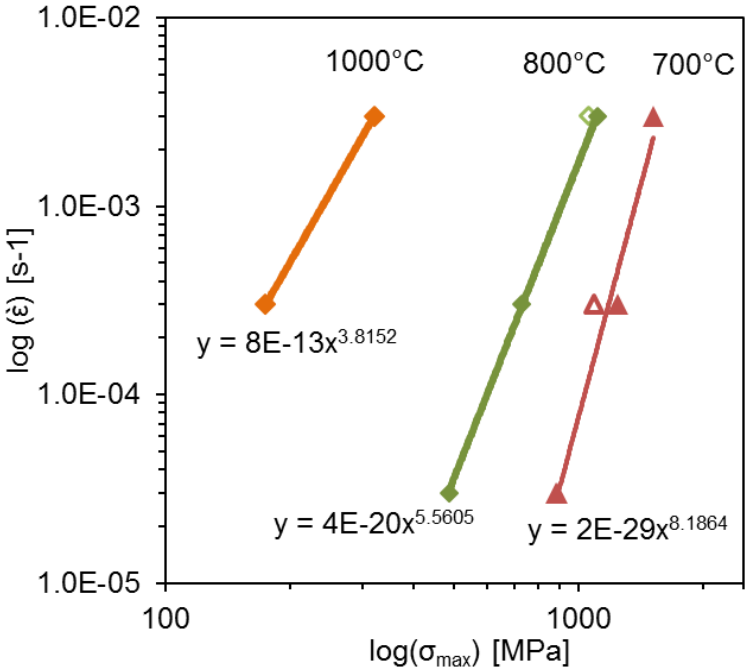

Figure C-9: Strain rate dependence of strength for 15Nb alloy, showing stress exponent determination

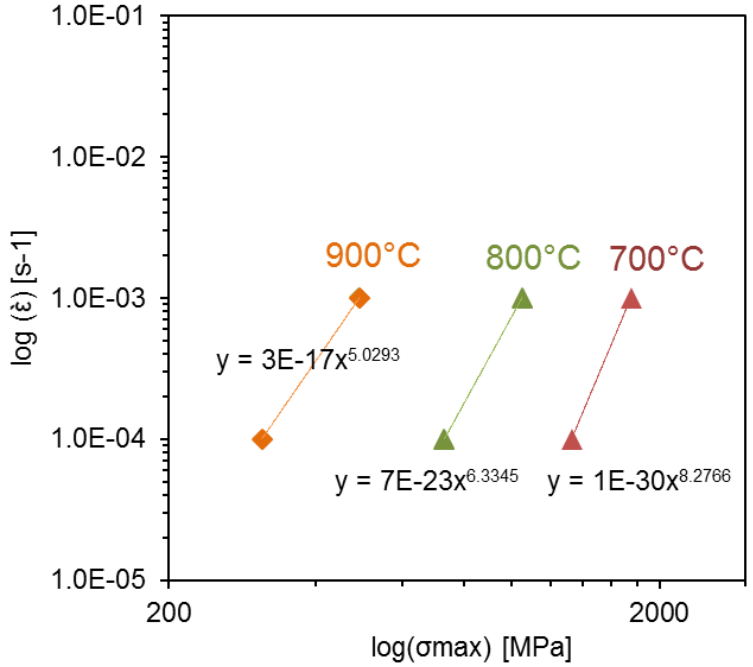

Figure C-10: Strain rate dependence of strength for 20Nb alloy, showing stress exponent determination

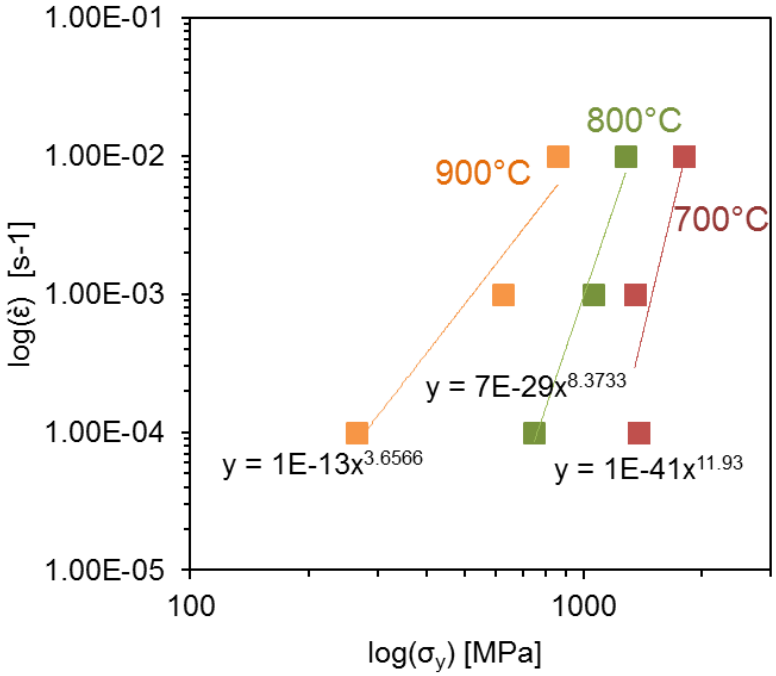

Figure C-11: Strain rate dependence of strength for 25Nb alloy, showing stress exponent determination. Note: for fitting at 900C, two lines of different slope were fitted to determine n-values for “high” and “low” strain rates, as listed in the following table.

Table C-1: Calculated values for n, Q for compression testing of alloys at high temperature. Note change in stress exponent for 25Nb alloy at 900C; apparent change in mechanism leads to differences in n, Q

Alloy	T (°C)	n	Q	T range (°C)
15 Nb	700	8.18		
	800	5.56	-36.9	(700-800)
	1000	3.82	-59.2	(800-1000)
20 Nb	700	8.28		
	800	6.33	-34.3	(700-800)
	900	5.03	-47.4	(800-900)
25 Nb	700	11.93		
	800	8.37	-23.9	(700-800)
	900	7.24 [high]	-31.7	(800-900 [high])
		2.68 [low]	-49.1	(800-900 [low])

LIST OF REFERENCES

[1] B.J.G. deAragao, F. Ebrahimi, High temperature deformation of Nb-Ti-Al alloys with sigma+gamma microstructure, Materials Science and Engineering a-Structural Materials Properties Microstructure and Processing, 208 (1996) 37-46.

[2] F. Appel, R. Wagner, Microstructure and deformation of two-phase gamma-titanium aluminides, Materials Science & Engineering R-Reports, 22 (1998) 187-268.

[3] D.M. Dimiduk, Gamma titanium aluminide alloys - an assessment within the competition of aerospace structural materials, Materials Science and Engineering a-Structural Materials Properties Microstructure and Processing, 263 (1999) 281-288.

[4] F. Appel, M. Oehring, R. Wagner, Novel design concepts for gamma-base titanium aluminide alloys, Intermetallics, 8 (2000) 1283-1312.

[5] G.E. Aviation, The GEnx Engine Family, in, General Electric Company, 2012.

[6] J.P. Lin, X.J. Xu, Y.L. Wang, S.F. He, Y. Zhang, X.P. Song, G.L. Chen, High temperature deformation behaviors of a high Nb containing TiAl alloy, Intermetallics, 15 (2007) 668-674.

[7] E. Hamzah, M. Kanniah, M. Harun, Effect of chromium addition on microstructure and creep strength of as-cast Ti-48Al alloy, Materials Science and Engineering a-Structural Materials Properties Microstructure and Processing, 483-84 (2008) 555-559.

[8] J.P. Quast, C.J. Boehlert, Comparison of the microstructure, tensile, and creep behavior for Ti-24Al-17Nb-0.66Mo (atomic percent) and Ti-24Al-17Nb-2.3Mo (atomic percent) alloys, Metall. Mater. Trans. A-Phys. Metall. Mater. Sci., 38A (2007) 529-536.

[9] Q. Liu, P. Nash, The effect of Ruthenium addition on the microstructure and mechanical properties of TiAl alloys, Intermetallics, 19 (2011) 1282-1290.

[10] M.S. Kesler, S. Goyel, O. Rios, D.M. Cupid, H.J. Seifert, F. Ebrahimi, A study of phase transformation in a TiAlNb alloy and the effect of Cr addition, Materials Science and Engineering a-Structural Materials Properties Microstructure and Processing, 527 (2010) 2857-2863.

[11] F. Appel, J.D.H. Paul, M. Oehring, U. Frobel, U. Lorenz, Creep behavior of TiAl alloys with enhanced high-temperature capability, Metall. Mater. Trans. A-Phys. Metall. Mater. Sci., 34A (2003) 2149-2164.

[12] B.J.G. DeAragao, F. Ebrahimi, High Temperature Deformation of a Nb-Ti-Al Alloy with sigma+gamma Microstructure, in, MRS Proceedings, 1995, pp. 1247-1252.

[13] F. Ebrahimi, B.J.G. Dearagao, J.R. Castillogomez, Evaluation of Fracture Toughness of Duplex microstructures by an Indentation Technique, Materials Science and Engineering a-Structural Materials Properties Microstructure and Processing, 177 (1994) L7-L10.

[14] F. Ebrahimi, D.T. Hoelzer, J.R. Castillogomez, Fracture toughness of sigma+X microstructures in the Nb-Ti-Al system, Materials Science and Engineering a-Structural Materials Properties Microstructure and Processing, 171 (1993) 35-45.

[15] O. Rios, S. Goyel, M.S. Kesler, D.M. Cupid, H.J. Seifert, F. Ebrahimi, An evaluation of high-temperature phase stability in the Ti-Al-Nb system, Scr. Mater., 60 (2009) 156-159.

[16] M.S. Kesler, Deformation and Fracture Behavior of Ti-Al-Nb-(Cr,Mo) Alloys with a Gamma + Sigma Microstructure at Ambient Temperature, in: Materials Science and Engineering Department, Universidy of Florida, Gainesville, FL, 2011, pp. 237.

[17] X.J. Wu, A.K. Koul, Grain Boundary Sliding in the Presence of Grain Boundary Precipitates during Transient Creep, Metall. Mater. Trans. A-Phys. Metall. Mater. Sci., 26 (1995) 905-914.

[18] H. Tanaka, M. Murata, F. Abe, K. Yagi, The effect of carbide distributions on long-term creep rupture strength of SUS321H and SUS347H stainless steels, Materials Science and Engineering a-Structural Materials Properties Microstructure and Processing, 234 (1997) 1049-1052.

[19] G.E. Deiter, Mechanical Metallurgy, McGraw-Hill, London, 1988.

[20] a.J.L. John Price Hirth, Theory of Dislocations, McGraw-Hill, Inc., 1968.

[21] R. Reed-Hill, R. Abbaschian, Physical Metallurgy Principles, 3rd Edition ed., PWS Publishing Company, Boston, 1994.

[22] G. Bean, F. Ebrahimi, H.J. Seifert, M. Manuel, High Temperature Deformation of Ti-Al-Nb-Cr-Mo Alloys, in, TMS 2012: Annual Meeting and Exhibition, Orlando, FL, 2012.

[23] S. Goyel, O. Rios, M.S. Kesler, F. Ebrahimi, Two-step nucleation of the gamma-phase in a Ti-45Al-18Nb alloy, Intermetallics, 18 (2010) 1491-1497.

[24] J.P. Lin, L.L. Zhao, G.Y. Li, L.Q. Zhang, X.P. Song, F. Ye, G.L. Chen, Effect of Nb on oxidation behavior of high Nb containing TiAl alloys, Intermetallics, 19 (2011) 131-136.

[25] E.L. Hall, S.-C. Huang, Microstructures of rapidly-solidified binary TiAl alloys, Acta Metall. Mater., 38 (1990) 539-549.

[26] Y.-W. Kim, Effects of microstructure on the deformation and fracture of γ-TiAl alloys, Materials Science and Engineering: A, 192–193, Part 2 (1995) 519-533.

[27] Y.-W. Kim, D.M. Dimiduk, Progress in the understanding of gamma titanium aluminides, JOM, 43 (1991) 40-47.

[28] S.-C. Huang, E.L. Hall, Characterization of the effect of vanadium additions to TiAl base alloys, Acta Metall. Mater., 39 (1991) 1053-1060.

[29] Y.-W. Kim, Ordered intermetallic alloys, part III: Gamma titanium aluminides, JOM, 46 (1994) 30-39.

[30] Y.W. Kim, A. Rosenberger, D.M. Dimiduk, Microstructural changes and estimated strengthening contributions in a gamma alloy Ti–45Al–5Nb pack-rolled sheet, Intermetallics, 17 (2009) 1017-1027.

[31] H. Lipsitt, D. Shechtman, R. Schafrik, The deformation and fracture of TiAl at elevated temperatures, Metallurgical Transactions A, 6 (1975) 1991-1996.

[32] M. Yamaguchi, Y. Umakoshi, The deformation behaviour of intermetallic superlattice compounds, Progress in Materials Science, 34 (1990) 1-148.

[33] J.R. Castillo-Gomez, Development of High Temperature Niobium Based Alloys, in: Materials Science and Engineering, Univerisity of Florida, 1990.

[34] D. Vojtech, T. Popela, J. Hamacek, J. Kutzendorfer, The influence of tantalum on the high temperature characteristics of lamellar gamma + alpha 2 titanium aluminide, Materials Science and Engineering a-Structural Materials Properties Microstructure and Processing, 528 (2011) 8557-8564.

[35] C.G. Wilson, F.J. Spooner, Order in NbAl and TaAl type Sigma Phases, Journal of Materials Science, 12 (1977) 1653-1658.

[36] B.T. Solomon, An investigation into the correlation of fracture toughness and microstructure for the sigma+beta structure in the Nb-Ti-Al ternary system, in, University of Florida, 1991.

[37] S. Das, J.M. Howe, J.H. Perepezko, A high-resolution transmission electron microscopy study of interfaces between the γ, B2, and α2 phases in a Ti-Al-Mo alloy, Metallurgical and Materials Transactions A, 27 (1996) 1623-1634.

[38] D.M. Cupid, O. Fabrichnaya, O. Rios, F. Ebrahimi, H.J. Seifert, Thermodynamic re-assessment of the Ti-Al-Nb system, Int. J. Mater. Res., 100 (2009) 218-233.

[39] S. Goyel, The Study of the Beta to Gamma Phase Transformation in High-Nb Ti-Al-Nb Alloys, in: Materials Science and Engineering, University of Florida, Gainesville, FL, 2011.

[40] F. Ebrahimi, Castillogomez, Jr., The Effect of Plastic Deformation on Fracture morphology of the Sigma Phase in the Nb-Ti-Al System, Acta Metall. Mater., 40 (1992) 1409-1416.

[41] V. Recina, D. Lundstron, B. Karlsson, Metallurgical and Materials Transactions A, 33A (2008) 2869-2881.

[42] D.T. Hoelzer, in: Materials Sciencenand Engineering, University of Florida, Gainesville, FL, 1996.

[43] J.B. Forsyth, J.P. Brown, Structure of Sigma Phase Nb2Al, Acta Crystallographica, 14 (1961) 362.

[44] G. Bergman, D. Shoemaker, The Determination of the Crystal Structure of the Sigma Phase in the Iron-Chromium and Iron-Molybdenum Systems, Acta Crystallographica, 7 (1954) 857.

[45] E.O. Hall, S.H. Algie, The Sigma Phase, Metallurgical Reviews, 11 (1966).

[46] T. Ishimasa, Y. Kitano, Y. Komura, Faulted Structure in the Fe-Cr sigma-Phase, Phys. Stat. Sol., 66 (1981) 703.

[47] M.J. Marcinkowski, D.S. Miller, A study of defect sub-structures in the Fe-Cr sigma phase by means of transmission electron microscopy, Phil. Mag., 7 (1962).

[48] D.S. Zhou, H.W. Ye, K.H. Kuo, An HREM study of the intergrowth structures of sigma-related phases and the mu-phase, Philosophical Magazine A, 57 (1988) 907-922.

[49] A. Ohta, A. Noya, M. Takeyama, M. Taguchi, T. Sase, K. Sasaki, Preparation of Ta2Al intermetallic compound films and their application as diffusion barriers to Cu penetration, Thin Solid Films, 278 (1996) 6-11.

[50] H. Zhu, e. al, Materials Science & Engineering A, 483-484 (2008) 533-536.

[51] E.A. Ott, T.M. Pollock, Metallurgical and Materials Transactions A, 29A (1998) 965-978.

[52] J.G.L. Ruizaparicio, F. Ebrahimi, Diffusivity in the Nb-Al Binary Solid Solution, J. Alloy. Compd., 202 (1993) 117-123.

[53] A.A. Bondar, V.T. Witusiewicz, U. Hecht, M.V. Remez, V.M. Voblikov, N.I. Tsyganenko, Y.I. Yevich, Y.M. Podrezov, T.Y. Velikanova, Structure and Properties of Ti-Al Alloys Doped with Nb and Ta, Powder Metallurgy and Metal Ceramics, 50 (2011) 397-415.

[54] S. Azad, R.K. Mandal, A.K. Singh, Materials Science & Engineering A, 429 (2006) 219-224.

[55] D. Banerjee, Progress in Materials Science, 42 (1997) 135-158.

[56] S. Jung, H.S. Jang, M.H. Oh, J.H. Lee, D.M. Wee, Materials Science & Engineering A, 329 (2002) 13-18.

[57] A.K. Singh, D. Banerjee, Metallurgical and Materials Transactions A, 28 (1997) 1735-1743.

[58] H.Z. Niu, Y.Y. Chen, S.L. Xiao, L.J. Xu, Microstructure evolution and mechanical properties of a novel beta γ-TiAl alloy, Intermetallics, 31 (2012) 225-231.

[59] M.L. Weaver, M.J. Kaufman, Phase Relationships and Transformations in the Ternary Al-Ti-Ta System, Acta Metall. Mater., 43 (1995) 2625-2640.

[60] Y.S. Kim, K.R. Javed, G.J. Abbaschain, Final report on contract No. N00014-86-K-0178, Defense Advanced Research Projects Agency and Office of Naval Research, (1989).

[61] W.J. Boettinger, A.J. Shapiro, J.P. Cline, F.W. Gayle, L.A. Bendersky, F.S. Biancaniello, Investigation of the phase constitution of Al2TiTa, Scr. Metall. Materialia, 25 (1991) 1993-1998.

[62] V.T. Witusiewicz, A.A. Bondar, U. Hecht, V.M. Voblikov, O.S. Fomichov, V.M. Petyukh, S. Rex, Experimental study and thermodynamic modelling of the ternary Al–Ta–Ti system, Intermetallics, 19 (2011) 234-259.

[63] C. McCullough, J.J. Valencia, C.G. Levi, R. Mehrabian, Peritectic Solidification of Ti-Al-Ta Alloys in the Region of Gamma TiAl, Materials Science and Engineering a-Structural Materials Properties Microstructure and Processing, 156 (1992) 153-166.

[64] T. Velikanova, M. Turchanin, S. Ilyenko, G. Effenberg, Critical evaluation of the Aluminium–Tantalum–Titanium system, Calphad, 33 (2009) 192-199.

[65] D.M. Cupid, O. Fabrichnaya, F. Ebrahimi, H.J. Seifert, Thermodynamic assessment of the Al-Mo system and of the Ti-Al-Mo System from 0 to 20 at.% Ti, Intermetallics, 18 (2010) 1185-1196.

[66] D.M. Cupid, M.J. Kriegel, O. Fabrichnaya, F. Ebrahimi, H.J. Seifert, Thermodynamic assessment of the Cr-Ti and first assessment of the Al-Cr-Ti systems, Intermetallics, 19 (2011) 1222-1235.

[67] M. Hatherly, F.J. Humphreys, Recrystallization and Related Annealing Phenomena, Elsevier Science, Ltd., Tarrytown, NY, 1996.

[68] C.M. Sellars, M.J. Lutton, Dynamic Recrystallization in Ni and Ni-Fe Alloys during High Temperature Deformation, Acta Metallurgica, 17 (1969) 1033.

[69] F. Ebrahimi, J.G.L. RuizAparicio, Diffusivity in the Nb-Ti-Al ternary solid solution, J. Alloy. Compd., 245 (1996) 1-9.

[70] O. Rios, F. Ebrahimi, Spinodal decomposition of the gamma-phase upon quenching in the Ti-Al-Nb ternary alloy system, Intermetallics, 19 (2011) 93-98.

[71] J. Lankford, Journal of Materials Science Letters, 1 (1982) 493-495.

[72] M.F. Ashby, Strengthening Methods in Crystals, Applied Science, (1971) 137-192.

[73] X.Z. Liao, S. Cheng, E. Ma, Y.T. Zhu, Y.H. Zhao, Simultaneously Increasing the Ductility and Strength of Nanostructured Alloys, Adv. Mater., 18 (2006) 2280-2283.

[74] M.H. F.J. Humphreys, Recrystallization and Related Annealing Phenomena, Elsevier Science Ltd., Tarrytown, NY, 1996.

[75] W.G. Johnston, D.F. Stein, Stress dependence of dislocation velocity inferred from strain rate sensitivity, Acta Metallurgica, 11 (1963) 317-318.

[76] F.J. Humphreys, M. Hatherly, Recrystallization and Related Annealing Phenomena, Elsevier Science Ltd, Tarrytown, NY, 1996.

[77] R.W. Hertzberg, Deformation and Fracture Mechanics of Engineering Materials, 3rd Edition ed., John Wiley & Sons, In., 1989.

[78] D. Hull, D.J. Bacon, Introduction to Dislocations, Robert Maxwell, M. C., 1984.

[79] A.H. Committee, Volume 3, Alloy Phase Diagrams, ASM International, ASM Handbook Online, 1992.

[80] A. International, Standard Test Methods for Tension Testing of Metallic Materials (E8/E8M), in, ASTM International, West Conshohocken, PA, 2009 (revised).

[81] J.-O. Anderson, T. Helander, L. Hoglund, P. Shi, B. Sundman, THERMO-CALC & DICTRA, Computational Tools for Materials Science, Calphad, 26 (2002) 273-312.

[82] G. Bean, F. Ebrahimi, M. Manuel, High temperature deformation of Ti-Al-Nb-Cr-Mo alloy with Ultrafine Microstructure, Intermetallics, 49 (2014) 132-137.

[83] S. Neve, P. Masset, M. Shutze, H. Boumann, K. Bethge, H.E. Zschau, Characterization of the long time oxidation protection of fluorine implanted technical Ti-Al alloys using ipn beam methods, Nuclear Instruments and methods in Physics Research B, 266 (2008) 2441-2445.

[84] *Y. Wu*, *G.M. Song*, The Isothermal Oxidation Behavior of a Ti_3Al-Nb-V-Mo Alloy, The Open Corrosion Journal, 3 (2010) 7-15.

[85] A.H. Committee, Volume 2, Properties and Selection: Nonferrous Alloys and Special-Purpose Materials, ASM International, ASM Handbook Online, 1992.

[86] M.H. Poech, H.F. Fischmeister, Deformation of Two-Phae Materials: A Model Based on Strain Compatibility, Acta Metallurgica Et Materialia, 40 (1992) 487 - 494.

[87] A.A. Griffith, Proc. First Int. Cong. App. Mech, 1 (1924) 55.

[88] C.G. Sammis, M.F. Ashby, Acta Metallurgica, 34 (1986) 511.

[89] M.F. Ashby, S.D. Hallam, Acta Metallurgica, 34 (1986) 498.

[90] A.W. Thompson, J.C. Chestnutt, Identification of a Fracture Mode: The Tearing Topography Surface, Metallurgical Transactions A, 10A (1979) 1193-1196.

[91] L.Q.C.e. al., MRS Bulletin, 26 (2001) 197.

[92] M. Asta, V. Ozolins, C. Woodward, A First-Principles Approach to Modeling Alloy Phase Equilibria, JOM, (2001) 16.

[93] VULCAN Beam Line 7: The Engineering Materials Diffractometer at SNS, O.R.N. Lab (Ed.), ORNL, http://neutrons.ornl.gov/vulcan/.

BIOGRAPHICAL SKETCH

Glenn obtained his BS in Mechanical Engineering from the University of Central Florida, while undertaking his research and Honors Undergraduate Thesis in Solid Oxide Fuel Cells under the direction of Dr. Nina Orlovskaya. During his undergraduate career, Glenn had the opportunity to work as an intern in the NASA Kennedy Space Center Materials Failure Analysis Laboratory, learning about practical application and analysis of materials. As a graduate student at the University of Florida, Glenn began work under the advisement of Dr. Fereshteh Ebrahimi, and has continued to the completion of his master's degree work with Dr. Michele Manuel, and is currently pursuing his Ph.D. conducting research on alloy design, microstructure development, and mechanical testing of high temperature alloys based on the Ti-Al-Nb system. Glenn has also recently begun work with aluminum alloys, acting as team leader and senior researcher on the design and development of Al-based self-healing metal-matrix composites with shape memory alloy reinforcement.